The Pennsylvania State University

The Graduate School

Department of Electrical Engineering

AN INTELLIGENT CONTROL SYSTEM FOR A HYBRID FUEL CELL WITH GAS TURBINE POWER PLANT

A Dissertation in

Electrical Engineering

by

Wenli Yang

Submitted in Partial Fulfillment
of the Requirements
for the Degree of

Doctor of Philosophy

December 2009

The dissertation of Wenli Yang was reviewed and approved* by the following:

Kwang Y. Lee
Professor Emeritus of Electrical Engineering
Dissertation Co-Advisor
Co-Chair of Committee

W. Kenneth Jenkins
Department Head of Electrical Engineering
Professor of Electrical Engineering
Dissertation Co-Advisor
Co-Chair of Committee

Jeffrey S. Mayer
Associate Professor of Electrical Engineering

Robert M. Edwards
Professor of Nuclear Engineering

*Signatures are on file in the Graduate School

ABSTRACT

Fuel cell power plant is a novel, clean and efficient energy source in distributed generation, and received extensive attentions from researchers, developers, and governments in recent decades. As one of the most advanced fuel cell technologies, hybrid fuel cell power plant has shown its potential for applications and is already under commercialization. A hybrid fuel cell with gas turbine power plant was envisioned as a base-load power source for distributed generation. As an emerging technique, the need of advanced control systems, which are essential components that guarantee reliable and efficient operations for the power plant, has motivated this investigation.

This dissertation seeks to develop an intelligent control system to improve the energy conversion efficiency and the reliability of the hybrid fuel cell power plant. Toward this goal, an intelligent overall control system is established in the dissertation by developing and integrating a hybrid plant model, an optimal reference governor, and a fault diagnosis and accommodation system in the comprehensive control system. The hybrid plant model provides a novel modeling method that combines a mathematical model and a neural network model, which can identify plant parameters and uncertainties from operational data and can considerably improve the model accuracy for the following and future analysis and research work. The optimal reference governor is achieved by particle swarm optimization algorithms and a neural network state estimator to generate optimal setpoints and feedforward controls to improve plant efficiency. A nonlinear multi-objective optimization framework is developed by integrating heuristic optimization and artificial neural network technologies. Meanwhile, a fault diagnosis and

accommodation system is implemented with fuzzy logic to detect and regulate system faults, preventing instabilities and damages to the power plant during system failures. The capability of the fuzzy theory in detecting and regulating system faults is demonstrated.

The individual control systems are finally integrated into a comprehensive system that provides overall management for the hybrid power plant. With the integrated control system, the power plant can have high energy conversion efficiency in normal operations and can be well regulated during system failures. As a result, an intelligent autonomous control system is achieved to perform high quality plant-wide control, by which both efficiency and reliability can be guaranteed. Moreover, the presented intelligent control system and its design approach are not only valid for the hybrid fuel cell power plant, but also capable of other types of power plants, where efficiency and reliability need to be improved and guaranteed.

TABLE OF CONTENTS

LIST OF FIGURES

LIST OF TABLES

ACKNOWLEDGEMENTS

I would like to express my sincere gratitude to my advisor Prof. Kwang Y. Lee for his guidance, support, motivation, and patience though my Ph.D. study and research. This work would not have been possible without his great help and advice.

Besides my advisor, I would like to thank the rest of my committee: Prof. W. Kenneth Jenkins, Prof. Jeffrey S. Mayer, and Prof. Robert M. Edwards, for their encouragement, insightful comments and questions.

My sincere thanks also goes to Dr. S. Tobias Junker and Dr. Hossein Ghezel-Ayaph with FuelCell Energy, Inc. for providing me the data and the model, and for their valuable discussion and comments on my work.

Last but not the least, I would like to thank my family: my parents Yuming Yang and Yulan Liu, for giving birth to me at the first place, and thank my wife, Yan Wang, for her support and encouragement throughout my life.

Chapter 1

Introduction

1.1 Background and Motivation

This dissertation continues the work of developing an overall control system for a hybrid fuel cell power plant through the use of intelligent control techniques. The work is motivated by three major aspects. First, as a clean and safe energy source, fuel cell power plant becomes one of the most competitive energy sources for distributed generation. However, it is still a relatively new technology and should continue to be analyzed and improved. Second, the hybrid structure of fuel cells combined with gas turbine is one of the most advanced technologies in alternative energy and power generation. This hybrid power plant is still under commercialization, where a reliable operating and control system is indispensable. Third, since the fuel cell power plant will serve as a base load in the power system, the energy efficiency and system reliability are two major issues must be solved by control systems. The intelligent control system proposed in this work performs both optimal control and fault detection to the power plant to guarantee its efficiency and reliability.

1.1.1 Energy sources for distributed generation

Distributed generation (DG), which refers to any modular generation located at or near the load center, has significant positive impacts to power systems, including

improved power quality, diversification of power sources, reduction in transmission/ distribution losses, and improved reliability. The small, decentralized power plants in DG are categorized as photovoltaic, biomass, wind and fuel-based systems [1]. However, wind and biomass are constrained by the availability of wind and land, and photovoltaics are limited by the high cost and weather conditions. Compared with these DG and traditional generation technologies, fuel cell power plants do not have limitations of weather and land, but have many advantages:

- High conversion efficiency
- Very low emissions
- Quiet operation
- Flexible siting and scalability
- Fuel flexibility

Fuel cells generate electricity through an electrochemical process, where the chemical energy stored in the fuels is converted into direct current (DC) electricity without combustion. Through this smooth and continuous process, the fuels can be utilized efficiently with the only by-productions of water and carbon dioxide. Thus, the fuel cell power plant can achieve extremely clean, quiet and efficient operations. Meanwhile, the fuel cell system can utilize a variety of fuels. It can produce electricity and heat from hydrogen, natural gas, petroleum fuels or gases derived from coal and biomass. Therefore, with the high operational performance and flexible application capabilities, fuel cell power plant becomes a major source of distributed generation and possesses the ability of wide commercial applications.

Because of these advantages, fuel cell received extensive attentions and become an important part of U.S. distributed generation program, US smart grid program, and American Recovery and Reinvestment Act [2-4]. The first-generation of fuel cells for stationary power applications entered the commercial market in 1995. This type of fuel cell was used to generate very high-quality electricity and heat with negligible emissions in commercial and industrial settings. The second generation of stationary fuel cells is currently in the demonstration and commercialization phase. This type of fuel cell is expected to achieve higher efficiency at lower cost when used in distributed generation systems [5]. To reach this goal, fuel cell and its supporting facilities, including the control system, need further analysis and improvement before widely applied in the commercial market.

1.1.2 Hybrid fuel cell power plant

The integration of a fuel cell with a gas turbine has become a convincing technology that can greatly enhance the overall efficiency of the power plant. Based on this hybrid structure, a fuel cell and gas turbine hybrid system has been developed as a base-load power source for DG by FuelCell Energy, Inc. and the overall efficiency is expected to approach 75%. The major feature of this structure is a high integration level of fuel cells and a turbine system, which is incorporated to the fuel cell system through the interactions in gas and heat flows [6]. The gas turbine-compressor-generator system will produce electric power simultaneously with fuel cells. The DC power and

asynchronous AC power will be converted into synchronized AC power by a power conditioning system (PCS) [7] before feeding into the grid.

The direct fuel-cell with gas turbine (DFC/T) power plant in Figure 1-1 is developed based on a 250kW Molten Carbonate Fuel Cell (MCFC), whose electrolyte is molten carbonate salt with the operating temperature of 600°C - 650°C, and a 60kW Capstone MicroTurbine®. MCFC is a kind of high-temperature fuel cell where the fuel can be internally reformed to hydrogen without any additional reforming devices, so that the MCFC system is named as Direct Fuel-Cell (DFC). Compared with other available fuel cell techniques [2], such as phosphoric acid fuel cell (PAFC), solid oxide fuel cell (SOFC) and proton exchange membrane fuel cell (PEMFC), MCFC has the best performance-cost ratio that high capability and efficiency can be achieved at a relatively low price.

Figure 1-1 The 300kW DFC/T® power plant during factory alpha test [6].

1.1.3 Recent research and achievements

Before the DFC/T hybrid power plant was first established, the individual Direct FuelCell®, which is the basis of DFC/T plant, was the primary technology of fuel cell power generations. Since dynamic modeling and simulation have been proved to be powerful tools for the study of transient and global behaviors of the power generation systems [8], extensive research work has been done for the DFC power plant. A nonlinear mathematical model of an internal reforming molten carbonate fuel cell stack was first developed by Lukas *et al.* based on the principles of components and energy balances and thermochemical properties [8]. By simplifying the original stack model, a reduced-order dynamic model was developed for the study of grid transient, where the slower dynamics can be neglected [9]. Then, the plant-wide model of the entire direct fuel cell power plant, including fuel cell stack, heat exchangers, and oxidation devices, was built and simulated [10]. Based on this model, a local operation and control scheme was presented in [11], including flow, temperature, and pressure control.

The mathematical model of the hybrid DFC/T plant [12, 13] was obtained by integrating a gas turbine into the Direct FuelCell model and modularizing the computer simulation. However, the mathematical model of DFC/T was built on several assumptions and approximations, such as constant gas pressure and uniform temperature distribution, which made the model simpler but introduced model errors. These errors become significant when the simulation results are compared with the operational data of experiments. Before applying advanced intelligent control algorithm, the model accuracy must be improved.

Meanwhile, the dynamic model provides a platform for investigating advanced control algorithms and dynamic optimization methods during the design phase. To increase the efficiency of the power plant, an optimal off-line trajectory planning algorithm was designed in [14]. The optimal trajectories generated by this algorithm are then learnt by a neural network supervisor (NNS) [15], which provides on-line optimal setpoints for plant operations. The off-line optimization method is computationally expensive and is precluded in generating optimal solutions in real-time. While, the neural network supervisor may provide inordinate results if the operational patterns are not learned in the training phase. Therefore, an on-line updatable optimization algorithm needs to be developed for real-time operations.

In addition, one important issue that has not been involved in the previous research is the reliability of the hybrid power plant, especially during system failures. If faults occur in the power plant, the system behaviors may become completely different from normal situations. Under the operations of the local controllers, which were designed only for normal conditions and have only limited information of the entire plant, the system may be degraded, enter critical operational regions, or even become unstable. To perform effective and reliable control to the power plant during system failures, a special control scheme must be designed aiming fault situations.

1.1.4 Efficiency and reliability

The DFC/T hybrid power plant was designed for the base-load generation, and will be kept running at full load all through the year, except in the cases of repairs or

scheduled maintenance. The power plant will be working at a steady or smooth power load for a considerably long period of time. Thus, even a small improvement in efficiency will produce significant economic and environmental benefits in the long run. Meanwhile, highly reliable operations can guarantee the power quality, system stability, and minimize the average off-line time for scheduled maintenance or unexpected plant faults. Therefore, the primary objectives of its control and operation system are efficiency and reliability, rather than the fast responses for peak-load demand or backup power generations.

Although the theoretical efficiency of the DFC/T system can reach 75%, it still needs to be operated practically at an optimal status to achieve high efficiency. Because of the integration of the gas turbine, the entire system becomes more complicated than the individual fuel cell or gas turbine power plants. For such a multi-inputs multi-outputs (MIMO) and highly coupled system, the optimization is extremely difficult, especially for real-time operations. Hence, an intelligent control system with advanced optimization algorithm needs to be developed for the DFC/T system.

As a modern autonomous system, less and less human efforts are required during plant operations. To improve the reliability of the power plant, it is a necessity for the control system to monitor any possible faults in the system and to regulate the system to avoid critical operational regions before the faults are fixed manually. The control system also needs to have the ability to identify the type and the approximate location of the fault, so that the service time could be greatly reduced. As a part of the intelligent control system, a fault diagnosis and accommodation system is developed in the dissertation.

1.2 Statement of Propose

This dissertation will focus on three major issues on the analysis and operation of the DFC/T power plant. The first issue is mathematical model enhancement, which will improve the accuracy of the dynamic model for the following analysis and research work. The second issue is the optimization of plant operations to increase fuel efficiency. The third issue is the plant reliability, including system fault detection and accommodation, which will identify possible internal faults and regulate the system during system failures. The major research items are listed as follows:

- Mathematical model enhancement
  - Supplementary analytical model of internal energy dynamics
  - Parameter identification based on experimental data
  - Development of neural network model augmenters
- Optimization of plant operations
  - Investigations on multi-objective optimization algorithms
  - Development of optimization framework based on Particle Swarm Optimization (PSO) and other heuristic optimization algorithms
  - Neural network combined model as a plant state estimator
- Fault detection and accommodation
  - Fuzzy fault diagnosis system for fault identification and localization
  - Fuzzy fault accommodation system for fault regulation

The work of this dissertation will involve three issues regarding the methodology of intelligent control systems. These issues include modeling, optimization and fault diagnosis methods:

- Provide novel modeling methods: hybrid mathematical and neural network model, and combined neural network model.
- Develop an optimization framework with an on-line state estimator.
- Provide a framework of using fuzzy logic for fault detection and regulation.

1.3 Organization of the Dissertation

The fuel cell technologies, including basic mechanisms and recent commercializing techniques, are introduced in Chapter 2. The system process flows, chemical reactions, and a mathematical dynamic model of the DFC/T power plant are also investigated.

In Chapter 3, the mathematical model of the DFC/T power plant is enhanced by two methods to improve the model accuracy. An analytical method with least-squares and gradient descent approaches and a numerical method with neural network approach are applied for model augmentations.

For the optimization of the power plant, heuristic multi-objective optimizations and their variations are surveyed in Chapter 4, and a PSO-based optimal reference governor is developed in Chapter 5 to provide optimal setpoints and feedforward controls for plant operations. A neural network combined model is established as an estimator for the optimization framework.

In Chapter 6, fuzzy fault diagnosis and accommodation system is developed to improve the reliability of the hybrid power plant. Fuzzy fault patterns are defined. Membership functions and fuzzy rules are designed for fault detections and regulations. Multiple control methods are investigated and compared.

Finally, the hybrid mathematical model, optimal reference governor, fault diagnosis and accommodation system are integrated as an overall intelligent control system in Chapter 7. Conclusions are drawn and future works are anticipated in Chapter 8.

Chapter 2

The Hybrid Fuel Cell/Gas Turbine Power Plant

2.1 The Fuel Cells

A fuel cell is similar to a battery that converts chemical potentials to electric power through electrochemical reactions. The main difference between fuel cells and batteries is that batteries carry a limited amount of fuel internally, as an electrolytic solution and solid materials, but fuel cells consume reactants from an external source, which can be constantly replenished. In a fuel cell, the fuel on the anode side and the oxidant on the cathode side react in the presence of an electrolyte. The reactants flow into the cell, and the products flow out of it, while the electrolyte remains within it. Hence, fuel cells can operate continuously without replacement as long as the necessary maintenance is performed.

A battery is an energy storage device, but a fuel cell is an energy conversion device. The maximum available energy in a battery is determined by the amount of chemical reactant stored in it. The battery will stop producing energy when the chemical reactants are consumed. In contrast, the reactants in a fuel cell are replenished from an external source. Thus, a fuel cell theoretically has the capability of producing electrical energy as long as fuel and oxidant are supplied to the electrodes. In reality, degradation, primarily corrosion, or malfunction of components limits the practical operating life of fuel cells.

Fuel cells generate electricity through an electrochemical reaction process, in which the energy stored in fuel is converted into direct current (DC) electricity. Because fuel cells generate electric energy without combustion, they have many advantages as an energy conversion device:

- High energy conversion efficiency
- Very low emissions
- Low noise
- Fuel flexibility
- Modular design

2.1.1 A typical fuel cell

In a typical fuel cell as shown in Figure 2-1, a gaseous fuel (*i.e.,* hydrogen) is fed continuously to the anode, an oxidant (*i.e.*, oxygen) is fed continuously to the cathode. The electrochemical reactions take place at the electrodes to produce electric currents. The overall chemical reaction can be described by the following equitation:

$$H_2 + \frac{1}{2}O_2 \xrightarrow[\text{reactions}]{\text{electrochemical}} H_2O + \text{Power} \tag{2.1}$$

Outside the fuel cell, electrons are released from the anode, and return to the cathode through a load, where the current turns into electric power. Inside the fuel cell, positive ions move from anode to cathode, or negative ions move from cathode to anode in the electrolyte to recruit the electrons at the electrodes. The type of the electrolyte and ion species can be various in different fuel cells. Meanwhile, the electrode material should be

catalytic as well as conductive, porous rather than solid. The catalytic function of electrodes is more important in lower temperature fuel cells and less so in high temperature fuel cells because ionization rates increase with temperature.

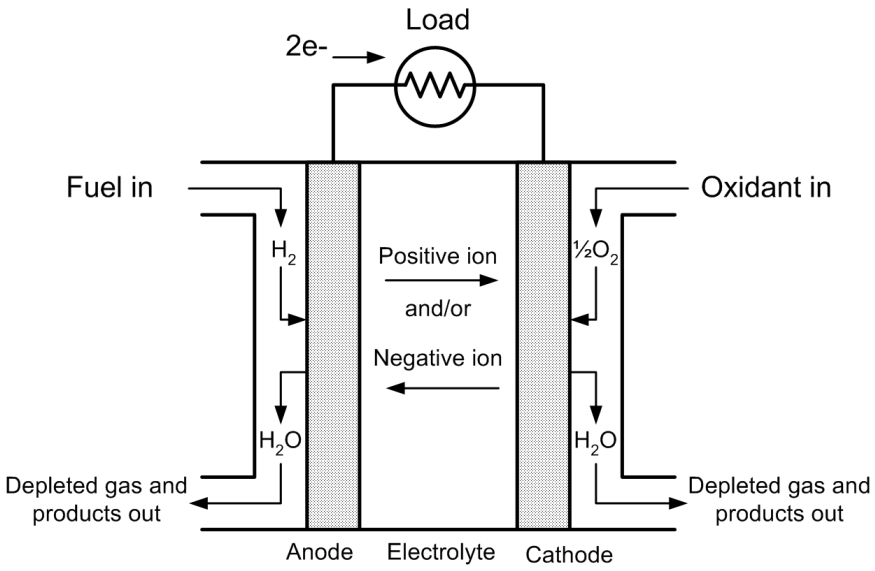

Figure 2-1 The concept and a prototype of a fuel cell.

2.1.2 Types of fuel cells

There are four main types of fuel cells currently being developed. They include Phosphoric Acid Fuel Cells (PAFC), Molten Carbonate Fuel Cells (MCFC), Solid Oxide Fuel Cells (SOFC), and Proton Exchange Membrane Fuel Cells (PEMFC).

Phosphoric Acid Fuel Cells (PAFC) are the most commercially developed type of fuel cell. They range in size from 50 kW to 500 kW, and both stationary and vehicle applications are possible. This type of fuel cell operates at 190˚C, and the peak current density ranges around 200mA/cm^2. It generates electric power at more than 40%

efficiency, and the startup time is 1 to 4 hours. The PAFCs are being widely used in commercial buildings, airports, and utility power plants [16].

Molten Carbonate Fuel Cells (MCFC) have promised high fuel-to-electricity efficiencies of 50-60%. They operate at 600˚C to 650˚C, so that the fuel can be reformed directly into hydrogen. The MCFCs range in size from 250 kW to 5 MW with peak current density about 160mA/cm^2, and need a startup time up to 10 hours. The high efficiency and high operating temperature of MCFC units makes them most attractive for base-load power generation, either in electric-only or cogeneration modes [16].

Solid Oxide Fuel Cells (SOFC) can be scaled from kW-size units to MW-size units for large high-power applications, including industrial and large-scale central electricity generating stations. The high operating temperature of 1000˚C makes it possible to reform fuels to hydrogen internally. Power generating efficiencies in SOFCs could reach 60%, and 80% in co-generation applications [16].

Proton Exchange Membrane Fuel Cells (PEMFC) operate at relatively low temperatures about 80˚C, having high power density up to 700mA/cm^2, and able to vary output power quickly. The PEMFCs range in size from sub-kW to 500 kW. Because of their high power density and fast response, the most attractive applications are in the automotive industry and portable devices. However, the costs for the proton exchange membranes are relatively high [16].

2.2 The Direct FuelCell Power Plant

Because of the promising fuel efficiency and the commercializing ability of MCFC, a direct reforming MCFC (under the trade name of Direct FuelCell® or DFC®) was developed by FuelCell Energy, Inc. Different form the conventional fuel conversion technologies, where fuel turns into a hydrogen-rich gas in an external fuel processor, the DFC reforms natural gas internally in the anode compartment with a reforming catalyst directly placed in the anode of the fuel cell [17]. The chemical reactions of fuel reforming and water-gas shift partially convert the methane and water into hydrogen, the effective reactant of the electrochemical reactions at the anode, and carbon dioxide as the following equations. The internal fuel reformation results in a simpler plant configuration and improved efficiency.

$$CH_4 + H_2O \xrightarrow{\text{reforming}} CO + 3H_2 \tag{2.2}$$

$$CO + H_2O \xrightarrow{\text{water-gass shift}} CO_2 + H_2 \tag{2.3}$$

Moreover, a single fuel cell can only produce a voltage less than one volt with a low current capability. Thus, to produce electric power in practicable voltage and current ranges, fuel cells are connected both in parallel and in series, composing a "fuel cell stack". Heat recuperators are placed prior to the fuel cell stack to prepare the fuel to an appropriate temperature with the recycled heat from the depleted gas.

A demonstration project of the DFC technology was established in Santa Clara, California, 1997. A 2 Mega-Watt DFC power plant was set up and connected to the

utility grid. The MCFC technology, plant reliability, performance, fuel efficiency, and its commercializing potential are verified in the project [18].

2.3 The Hybrid DFC/T Power Plant

The integration of fuel cells with a gas turbine has become a convincing technology that can greatly enhance the overall efficiency of the power plant. Based on this hybrid structure, the fuel cell and turbine system (under the trade names: Direct FuelCell/Turbine® and MicroTurbine™) has been developed by FuelCell Energy, Inc. and expected to be a base-load power source in distributed generation. The major feature of this structure is a high integration level of fuel cells, gas turbine, and heat recuperators [6]. Figure 2-2 shows the simplified system diagram of the hybrid power plant, where a gas turbine is integrated to the Direct FuelCell system both mechanically and thermo-dynamically. The fuel cell and the generator propelled by the gas turbine generate electric power simultaneously. The DC power from the fuel cell stack and the asynchronous AC power from the generator will be converted to synchronized AC power by a power conditioning system (PCS) [7] before connecting to the utility grid.

The significance of the integration of the gas turbine is the highly improved fuel efficiency. Because the gas turbine is deeply integrated to the fuel cell system, it can utilize the fuel energy (heat) more efficiently than simply using the exhaust heat for co-generation, so that the overall fuel utilization can be considerably improved [19]. In Figure 2-3, the efficiencies of different power generation techniques are plotted against their size ranges. An individual gas turbine can only reach the efficiency of 40%; while,

an individual DFC system has 50% to 55% efficiency. However, the hybrid DFC/T plant can achieve a much higher efficiency up to 75%. With most traditional technologies, economies of scale are critical to obtaining efficient power generation. However, the DFC/T is not dependent on economies of scale to achieve high efficiency.

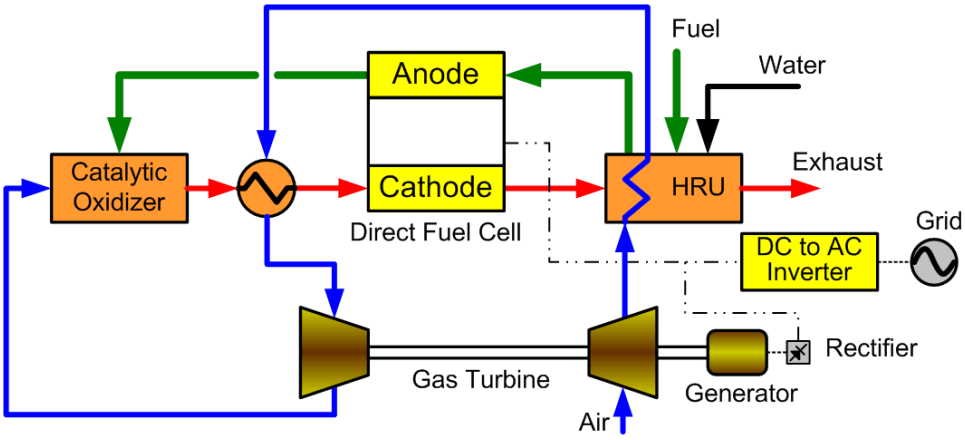

Figure 2-2 The integrated Direct FuelCell and gas turbine [6].

The combination of the MCFC and gas turbine improves the plant efficiency, but at the same time, it increases the system complexity. The gas turbine introduces air into the fuel cell and uses the excessive fuel and heat to generate extra power. The gas turbine and fuel cell are highly coupled both in gas flows and in heat flows, both mechanically and thermo-dynamically. Therefore, advanced operating and control systems need to be developed for this hybrid structure. Further analysis and improvement are necessary in the testing and the commercializing phase.

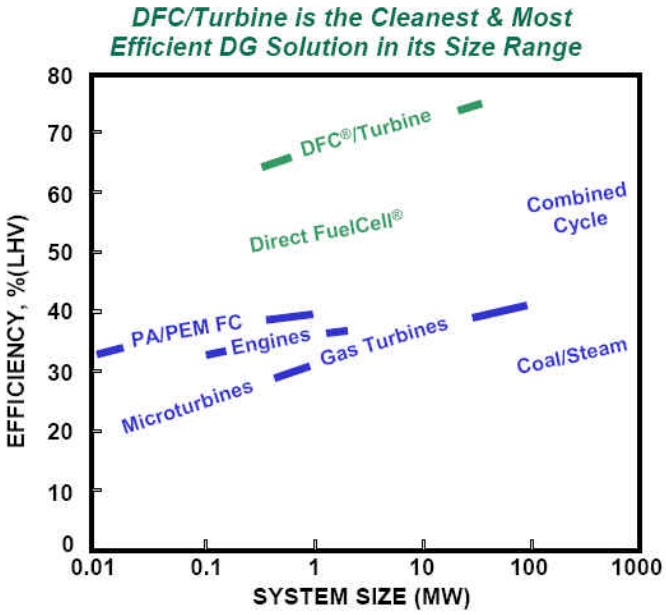

Figure 2-3 Fuel efficiency of power generation technologies [6].

2.4 Process Description

The detailed process flow diagram is shown in Figure 2-4. The fuel (*i.e.*, methane and water) is introduced to the plant through a Humidifying Heat Exchanger (HumiHex or HH), where the methane is humidified and heated. Then, a Fuel Pre-heater (FP) heats the fuel again to a constant temperature determined by the characteristic of the catalyzer in the Pre-fuel Converter (PC), in which the fuel is partially reformed to hydrogen. The fuel is finally heated in a Super Heater (SH) to an appropriate temperature prior to entering the fuel cell anode.

On the other side of the plant, cold air in ambient temperature is compressed and introduced to the system by an air compressor, which is driven by the gas turbine. The compressed air is heated by a Low Temperature Recuperator (LTR), a Second Start-up

Heater (SSH), and a High Temperature Recuperator (HTR), subsequently. The high pressure air with high temperature then expands in the gas turbine to drive the air compressor and a permanent magnet generator (PMG) to produce electric power. The exhausted air form the turbine and the depleted fuel from the anode are mixed and burnt in an Anode Gas Oxidizer (AGO), producing high temperature oxidative gas. The excessive heat from the AGO is transferred to the incoming air via HTR to impel the turbine. The cooled AGO off gas enters the cathode as the oxidizer for the fuel cells. Finally, the heat from the cathode off gas is recycled to heat the fresh fuel and air through SP, FP, LTR, and HH [12].

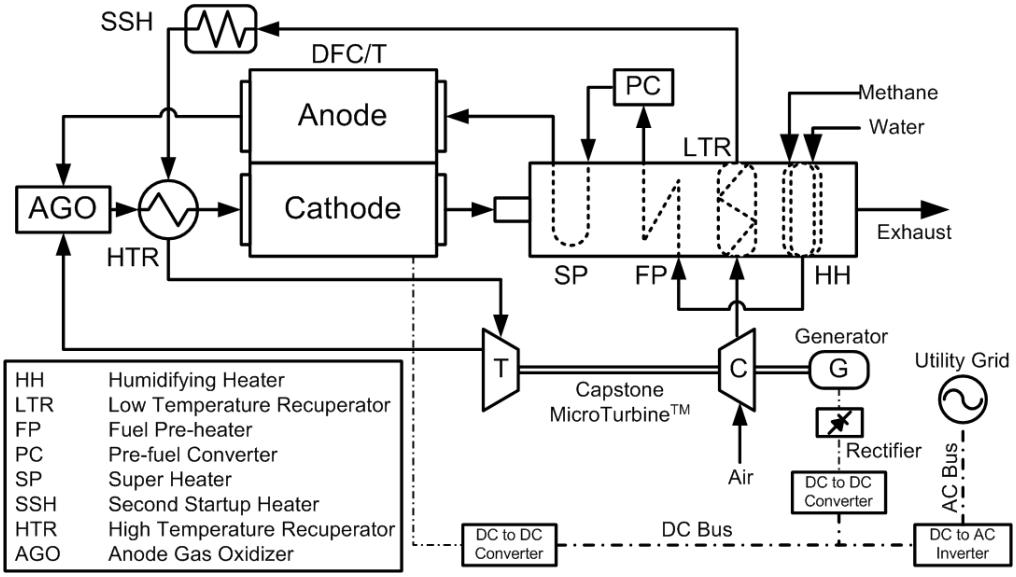

Figure 2-4 The process flow diagram of the DFC/T power plant.

In addition, when the DFC/T power plant is in the starting-up process, only a small amount of fuel is supplied, from which the plant cannot produce sufficient heat to warm up itself. Thus, the SSH, an electric heater, will provide extra heat to the system, and the PMG will work as an electric motor to drive the air compressor [6].

2.4.1 Chemical reactions

Although there are a number of subunits in the DFC/T power plant, chemical reactions take place only in three of them [12], *i.e.*, the PC, the fuel cell stack, and the AGO. Fuel reforming and water-gas shift reactions, as in (2.2) and (2.3), take place in both PC and the anode of the fuel cell stack. Electrochemical reactions take place in the anode and cathode of the fuel cell stack as follows:

Anode: $$H_2 + CO_3^{=} \rightarrow CO_2 + H_2O + 2e^- \tag{2.4}$$

Cathode: $$CO_2 + \frac{1}{2}O_2 + 2e^- \rightarrow CO_3^{=} \tag{2.5}$$

The overall chemical reactions can be concluded as:

$$H_2^{anode} + CO_2^{cathode} + \frac{1}{2}O_2^{cathode} \rightarrow CO_2^{anode} + H_2O^{anode} + \text{Heat} + \text{Power} \tag{2.6}$$

The excessive fuel from the anode is burnt and fully oxidized in the AGO. The chemical reactions include [10]:

$$CH_4 + 2O_2 \rightarrow CO_2 + 2H_2O + \text{Heat} \tag{2.7}$$

$$H_2 + \frac{1}{2}O_2 \rightarrow H_2O + \text{Heat} \tag{2.8}$$

$$CO + \frac{1}{2}O_2 \rightarrow CO_2 + \text{Heat} \tag{2.9}$$

Thus, the AGO prepares carbon dioxide for the cathode reactions, and heat for the turbine and generator.

2.4.2 Electrical power flows

To feed the electrical power to utility grid, the DC power from the fuel-cell stack and the asynchronous AC power from the permanent magnet generator (PMG) must be synchronized in frequency and phase angle by a power conditioning system (PCS) [7] as Figure 2-5. The fuel cells usually generate DC power in a low voltage range, which should be boosted to a higher voltage for DC bus by DC-DC converters before inverted to synchronized AC power. The AC power from the PMG is rectified into DC power and then boosted to the voltage of the DC bus. A DC-AC inverter is used to convert the DC power to synchronized AC power, which can be connected to utility grid. Super capacitors and power filters may be applied to eliminate or reduce the undesired harmonics introduced by the switching components of the inverter [7].

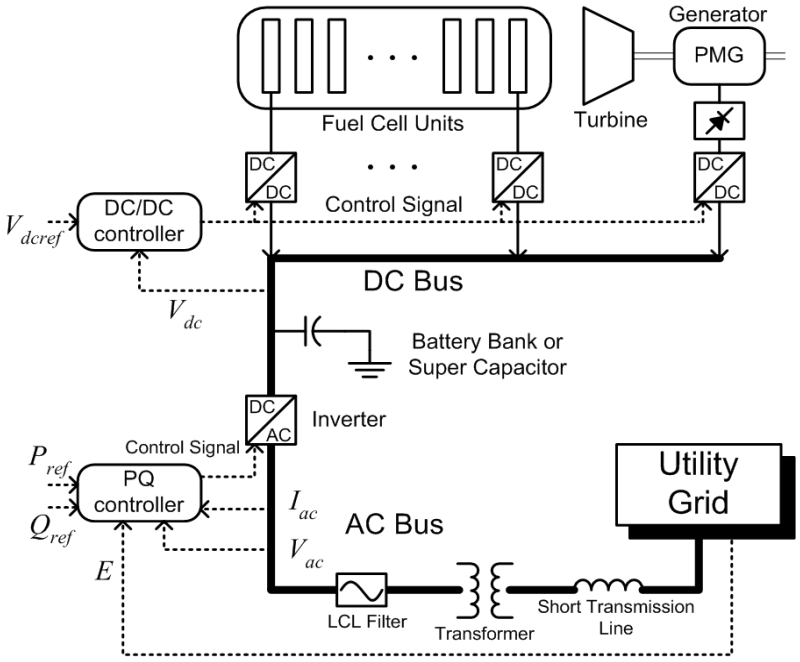

Figure 2-5 Power conditioning system based interface to utility grid.

2.4.3 Control schemes

The operational states of the plant, such as power, temperature, and rotational speed, must be controlled to generate desired power with smooth and reliable processes. For the DFC/T power plant, the output power is determined by the amount of the fuel fed into the system and the current drawn from the fuel-cell stack, and are regulated by feedforward controls. Since the temperature of the fuel cell stack is dominated by the cathode inlet gas and the output DC power, the stack temperature is maintained by the feedback controls of the SSH, LTR, and AGO through split valves according to the setpoint of cathode inlet temperature, which is a function of the stack power and is specified by the plant manufacturer. The turbine speed is controlled by the PMG, a speed controller, and a DC-DC converter according to the speed setpoint. By modifying the armature current of the equivalent DC generator [14], the torque can be regulated, and consequently, the shaft speed can be controlled. The detailed generator dynamics and control scheme can be found in Section 2.5.4 and Section 3.4.2. Moreover, the plant is operating at constant pressures regulated by two pressure controllers with constant setpoints [11]. Because of the complexity and importance in plant operations, the temperature controls are the primary control scheme to be investigated in this dissertation.

2.5 A Mathematical Model of Direct FuelCell and Gas Turbine

A plant wide dynamic simulation model was developed in [8, 10, 12] based on mass and energy conservation rules and the relationships of chemical reactions. A

nonlinear mathematical model of the internal reforming molten carbonate fuel cell stack was firstly developed in [8]. Based on the principles of energy and mass component balances and thermochemical properties, ordinary differential equations were built for cathode component balance, anode component balance, and stack energy balance, respectively. Based on this stack model, the plant-wide direct fuel cell simulation model and the DFC/T model were built in [10] and [12].

2.5.1 Cathode component balance

Since there are only seven chemical components in the whole system, for convenience, the set of all gas species is first identified as:

$$\mathbf{S} = \{H_2 \quad CH_4 \quad CO \quad CO_2 \quad H_2O \quad N_2 \quad O_2\} \tag{2.10}$$

where the ordering is used to refer to individual gas species (e.g., x_3 is the mole fraction of H_2O). Define the reaction rate of the electrochemical reaction as r_S in mole/s, and then the changing rates of each component due to the cathode reaction can be derived from to the coefficients of the reaction equation (2.5) as:

$$\mathbf{R}_C = [0 \quad 0 \quad 0 \quad -1 \quad -\frac{1}{2} \quad 0 \quad 0]' r_S \tag{2.11}$$

Dynamic equations can be built based on mole changing rates of cathode gas components:

$$\dot{\mathbf{n}}_C = \frac{d\left(N_C \mathbf{x}_C\right)}{dt} = \dot{N}_C \mathbf{x}_C + N_C \dot{\mathbf{x}}_C \tag{2.12}$$

$$\dot{N}_C = N_C^{in} - N_C^{out} + \sum_{i=1}^{7} R_C^{(i)} \tag{2.13}$$

$$N_C = \frac{P_C V_C}{R T_S} \tag{2.14}$$

where

$\mathbf{n}_C$ vector of mole amount of gas components stored in the cathode [mole];

N_C total mole number of the gas mixture stored in the cathode [mole];

$\mathbf{x}_C$ mole fractions of gas components in the cathode;

$\mathbf{x}_C^{in}$ mole fractions of the inlet stream of the cathode;

N_C^{in} / N_C^{out} gas inlet/outlet mole flow rate for the cathode [mole/s];

$R_C^{(i)}$ the *i*-th element of the vector $\mathbf{R}_C$ [mole/s];

P_C cathode gas pressure [kg/(m^2·s)];

V_C cathode compartment volume [m^3].

T_S fuel-cell stack temperature [K];

R universal gas constant [J/(mole·K)].

At the same time, $\dot{\mathbf{n}}_C$ can also be expressed by the inlet and outlet gas flow rates at the cathode side as:

$$\dot{\mathbf{n}}_C = N_C^{in}\mathbf{x}_C^{in} - N_C^{out}\mathbf{x}_C + \mathbf{R}_C \tag{2.15}$$

Combining (2.12)-(2.15), the following equation can be obtained and simplified [20]. This equation is used as the component balance equation for the cathode.

$$\dot{\mathbf{x}}_C = \frac{R T_S}{P_C V_C}\left[N_C^{in}\left(\mathbf{x}_C^{in} - \mathbf{x}_C\right) - \mathbf{x}_C \sum_{i=1}^{7} R_C^{(i)} + \mathbf{R}_C \right] \tag{2.16}$$

2.5.2 Anode component balance

Different from the cathode, where only one chemical reaction takes place, three reactions (*i.e.*, anode electrochemical reaction (2.4), reforming reaction (2.2), and water-gas shift (2.3)) present to the anode. The rate of the electrochemical reaction is r_S. Define the reaction rates of reforming and water-gas shift are r_{REF} and r_{WGS}, respectively. Then the changing rates of each component due to these reactions are:

$$\mathbf{R}_A = [-1 \quad 0 \quad 0 \quad 1 \quad 1 \quad 0 \quad 0]' r_S \tag{2.17}$$

$$\mathbf{R}_{REF} = [3 \quad -1 \quad 1 \quad 0 \quad -1 \quad 0 \quad 0]' r_{REF} \tag{2.18}$$

$$\mathbf{R}_{WGS} = [1 \quad 0 \quad -1 \quad 1 \quad -1 \quad 0 \quad 0]' r_{WGS} \tag{2.19}$$

Dynamic equations can be built based on mole changing rates of the gas components stored in the anode:

$$\dot{\mathbf{n}}_A = \frac{d\left(N_A \mathbf{x}_A\right)}{dt} = \dot{N}_A \mathbf{x}_A + N_A \dot{\mathbf{x}}_A \tag{2.20}$$

$$\begin{aligned} \dot{N}_A &= N_A^{in} - N_A^{out} + \sum_{i=1}^{7} R_A^{(i)} + \sum_{i=1}^{7} R_{REF}^{(i)} + \sum_{i=1}^{7} R_{WGS}^{(i)} \\ &= N_A^{in} - N_A^{out} + \sum_{i=1}^{7} R_A^{(i)} + 2r_{REF} \end{aligned} \tag{2.21}$$

$$N_A = \frac{P_A V_A}{R T_S} \tag{2.22}$$

where the symbols are defined coordinately to the cathode equations with a subscript of "*A*" denoting the variables are defined for the anode side.

At the same time, $\dot{\mathbf{n}}_A$ can also be expressed by the gas flow rates of the anode:

$$\dot{\mathbf{n}}_A = N_A^{in}\mathbf{x}_A^{in} - N_A^{out}\mathbf{x}_A + \mathbf{R}_A + \mathbf{R}_{REF} + \mathbf{R}_{WGS} \tag{2.23}$$

Combining (2.20)-(2.23), the following equation can be obtained and simplified. This equation is used as the component balance equation for the anode.

$$\dot{\mathbf{x}}_A = \frac{RT_S}{P_A V_A}\left[N_A^{in}\left(\mathbf{x}_A^{in} - \mathbf{x}_A\right) - (\sum_{i=1}^{7} R_A^{(i)} + 2r_{REF})\mathbf{x}_A + \mathbf{R}_A + \mathbf{R}_{REF} + \mathbf{R}_{WGS} \right] \tag{2.24}$$

Moreover, the reaction rate r_S is calculated according to a nonlinear relationship of electrochemical reactions. The reaction rates r_{REF} and r_{WGS} are determined based on the equilibrium point of reforming and water-gas shift reactions [20].

2.5.3 Stack energy balance

The energy balance equation was built for the entire stack. Let E denotes the total energy stored in the fuel cell stack. Then, $\dot{E}$ is the energy changing rate of the stack, which can be expressed either by the temperature changing rate, or by the inlet and outlet flows of the stack:

$$\dot{E} = C_S\dot{T}_S = N_C^{in}H_C^{in} - N_C^{out}H_C^{out} + N_A^{in}H_A^{in} - N_A^{out}H_A^{out} - P_S - Q_{loss} \tag{2.25}$$

where

C_S the specific heat capacity of the stack and stored gas [J/K];

$H_{C(A)}^{in}$ inflow mole enthalpy of the cathode (or anode) [J/mole];

$H_{C(A)}^{out}$ outflow mole enthalpy of the cathode (or anode) [J/mole];

P_S the electric power provided by the stack [J/s];

Q_{loss} power loss of the stack due to heat loss.

The mole enthalpy of any gas flow "X" can be calculated from a forth-order polynomial:

$$H_X = \sum_{k=1}^{7} x_X^{(k)} \left(A_k T_X + B_k T_X^2 + C_k T_X^3 + D_k T_X^4 \right) \tag{2.26}$$

where $x_X^{(k)}$ is the mole fraction of the k-th component, T_X is the temperature of the stream "X", and A_k, B_k, C_k, and D_k are the polynomial coefficients derived from the integration of the specific heat capacity of the k-th component in the mixture. Meanwhile, the outlet flow rates can be given as:

$$N_C^{out} = N_C^{in} + \sum_{i=1}^{7} R_C^{(i)} \tag{2.27}$$

$$\begin{aligned} N_A^{out} &= N_A^{in} + \sum_{i=1}^{7} R_A^{(i)} + \sum_{i=1}^{7} R_{REF}^{(i)} + \sum_{i=1}^{7} R_{WGS}^{(i)} \\ &= N_A^{in} + \sum_{i=1}^{7} R_A^{(i)} + 2r_{REF} \end{aligned} \tag{2.28}$$

By combining (2.25), (2.27), and (2.28), the following equation can be concluded. This equation is used as the energy balance equation for the fuel cell stack.

$$\dot{T}_S = \frac{1}{C_S} \begin{bmatrix} N_C^{in} \left(H_C^{in} - H_C^{out} \right) - H_C^{out} \sum_{i=1}^{7} R_C^{(i)} \\ + N_A^{in} \left(H_A^{in} - H_A^{out} \right) - H_A^{out} \left(\sum_{i=1}^{7} R_A^{(i)} + 2r_{REF} \right) \\ - P_S - Q_{loss} \end{bmatrix} \tag{2.29}$$

The first term in (2.29) gives the energy increasing rate at the anode side, and the second term represents the energy increasing rate at the cathode side. The third term is the energy decrement, including the electric power P_S, and the heat loss Q_{loss}.

2.5.4 Model of the gas turbine system

The gas turbine system is composed of a permanent magnet generator (PGM), a compressor, and a turbine linked mechanically to a common shaft and thermodynamically to the fuel cell process. The shaft is modeled by Newton's second law for rotation:

$$J\frac{d\omega}{dt} = \tau_T - \tau_C - \tau_G \tag{2.30}$$

where J is the moment of inertia of the linked mechanical system; ω is the angular speed of the rotation; and τ_T, τ_C, and τ_G are the torques of turbine, compressor, and generator, respectively. The torques of turbine and compressor are calculated from the energy balances:

$$\tau_{T,C} = \frac{\dot{n}_{T,C}\left[H_{T,C}^{out} - H_{T,C}^{in}\right]}{\omega} \tag{2.31}$$

where $\dot{n}_{T,C}$ is the mole air flow rate through the turbine and compressor, and is obtained from proprietary operating maps. Here, $H_{T,C}^{out}$ and $H_{T,C}^{in}$ are mole enthalpies of the outlet and inlet flows of the turbine and compressor, and are functions of temperature as (2.26). The outlet temperatures are obtained from the following equations with the definitions of the isentropic efficiencies η computed from the operating maps [14] for compression and expansion:

$$\eta_C = \frac{\left(T_{out}/T_{in}\right)-1}{\left(p_{out}/p_{in}\right)^{1-1/K}-1} \tag{2.32}$$

$$\eta_T = \frac{\left(p_{out}/p_{in}\right)^{1-1/K} - 1}{\left(T_{out}/T_{in}\right) - 1} \tag{2.33}$$

Since the PMG and rectifier can be approximated as a DC generator [14], the torque and the output voltage of the equivalent DC generator can be approximated as:

$$\tau_G = K_m I_G \tag{2.34}$$

$$v_G = K_e \omega \tag{2.35}$$

where K_m and K_e are the armature and motor constants; I_G and v_G are the DC current and voltage of the equivalent DC generator. I_G can be controlled by the DC-DC converter. Thus, the generator torque can be regulated according to (2.34), and consequently, the rotational speed ω can be controlled.

Chapter 3

Model Augmentation for the DFC/T Power Plant

A mathematical model provides a platform and a powerful tool for investigating advanced control theories and technologies to improve the reliability and efficiency of the hybrid DFC/T power plant. Thus, extensive studies have been invested into the dynamic mathematical model and autonomous control systems for DFC and DFC/T power plant. A nonlinear mathematical model of an internal reforming molten carbonate fuel cell stack was first developed by Lukas, *et al.* based on the principles of energy and mass components balances and thermochemical properties as described in Section 2.5 [8, 20]. Then, a plant-wide model of the overall direct fuel cell power plant was built and simulated [10]. On the basis of the DFC model, a local operation and control scheme was then presented in [11]. The theoretical model of the hybrid DFC/T plant is obtained with the integration of a gas turbine model and the plant-wide DFC model [12, 13].

However, due to the assumptions of the mathematical model and the uncertainties of the actual DFC/T plant, the errors between the simulation results and the experimental data are non-negligible. Thus, controllers or control algorithms designed based on this mathematical model may become degraded or invalid to the actual plant. Therefore, the accuracy of the mathematical model needs to be improved. In this chapter, a supplementary mathematical model is firstly introduced, and then an analytical method and a numerical method are proposed for model augmentation. Finally, pressure dynamic models are developed and results are demonstrated by simulations.

3.1 An Analytical Augmentation Approach

To verify the performance and accuracy of the original mathematical model in Section 2.5, a simulation was executed with the exactly same input conditions as in an experiment conducted for forty-two days from standby mode to a full power load. Taking the fuel-cell stack for example, in Figure 3-1, the simulation result is compared with the experimental data, where the actual temperatures of the anode and the cathode are not equal. However, because the energy model was built regarding the entire stack, identical temperatures are given for both electrodes. Thus, the original mathematical model cannot express the complete energy dynamics of the fuel-cell stack.

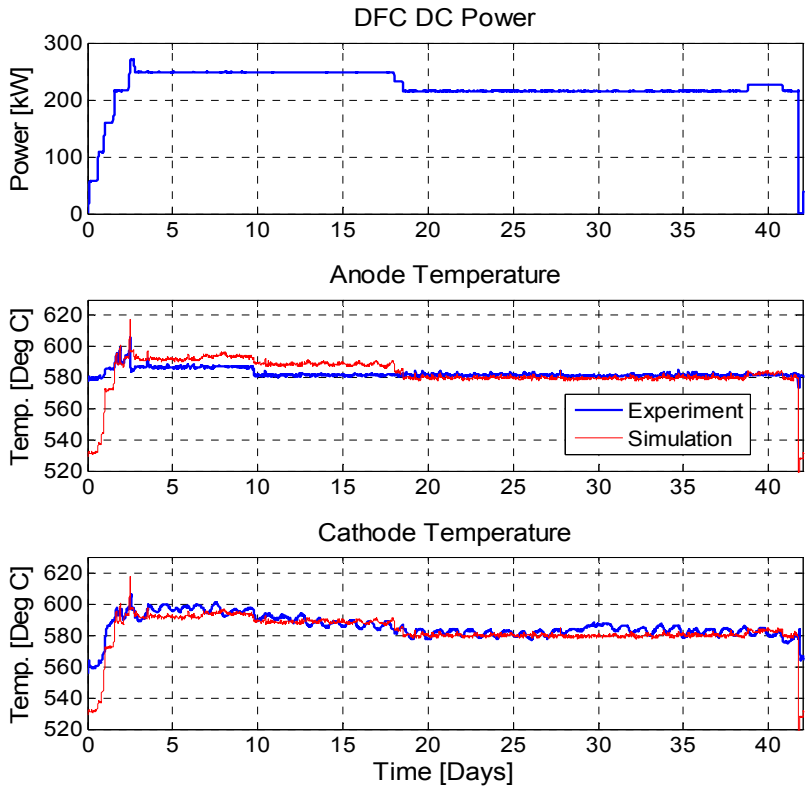

Figure 3-1 Fuel cell stack temperature of the original model and experiment.

Meanwhile, from Figure 3-1, the errors between the simulation result and the experimental data illustrate that the original stack model has significant errors at low power loads. In this case, advanced control algorithms developed on the plant model may become degraded or even unstable. Therefore, the energy model of the fuel-cell stack needs to be improved.

3.1.1 The internal dynamics of the stack

To model the energy dynamics more precisely, in this section, the stack temperature is split into the anode temperature and the cathode temperature. Energy balance equations are built for the chemical reactions on each side individually. Meanwhile, the mutual reactions between the anode and the cathode are also modeled, including mass transfer, heat transfer, and heat loss. The dynamic equations are presented as follows, where E_{aorg} and E_{corg} are the energy flow rate calculated by the original stack model without internal dynamics for anode and cathode, respectively, and E_{aaug} and E_{caug} represent the corresponding improved energy flow rates.

$$E_{aaug} = E_{aorg} + E_{mass} - E_{trans} - E_{loss}^{a} \tag{3.1}$$

$$E_{caug} = E_{corg} - E_{mass} + E_{trans} - E_{loss}^{c} \tag{3.2}$$

Here, E_{mass} is the energy transfer rate due to the mass transfer between the electrodes and is in proportion to the electrochemical reaction rate R, since the mass (*i.e.,* $CO_3^=$) transfer rate equals to the electrochemical reaction rate; E_{trans} is the energy transfer rate

due to the heat transfer and is in proportion to their temperature difference [21]; and E_{loss}^{a} and E_{loss}^{c} are the anode or cathode energy loss rates due to heat loss and in proportion to the temperature difference between anode or cathode temperature and the ambient temperature. These relationships are presented in (3.3) to (3.6), with the positive directions defined in Figure 3-2 by waved arrows:

$$E_{mass} = K_{mass} R \tag{3.3}$$

$$E_{trans} = K_{trans} \Delta T_{a2c}, \text{ where } \Delta T_{a2c} = T_{anode} - T_{cathode} \tag{3.4}$$

$$E_{loss}^{a} = K_{loss}^{a} \Delta T_{a2amb}, \text{ where } \Delta T_{a2amb} = T_{anode} - T_{ambient} \tag{3.5}$$

$$E_{loss}^{c} = K_{loss}^{c} \Delta T_{c2amb}, \text{ where } \Delta T_{c2amb} = T_{cathode} - T_{ambient} \tag{3.6}$$

Here, the coefficients K_{mass}, K_{trans}, K_{loss}^{a}, and K_{loss}^{c} are four constant parameters to be determined for the internal energy dynamics; K_{mass} is the energy contained in each mole of $CO_3^{=}$, which is always in a form of chemical compounds, and whose enthalpy cannot be directly measured; K_{trans} is determined by the heat conductance of the electrolyte located between the electrodes; and K_{loss}^{a} and K_{loss}^{c} are determined by heat characteristics of the fuel-cell stack shell. The last three parameters should be positive; otherwise positive feedback will be introduced to the model and will cause instabilities.

These parameters can be established by theoretical analysis or offline experiments. However, the analysis needs design details and is not accurate, while the offline experiments are not always applicable. Thus, in this dissertation, the parameters are

identified by two system identification methods based on online operating data, in case the design details are unavailable or offline experiments are not applicable.

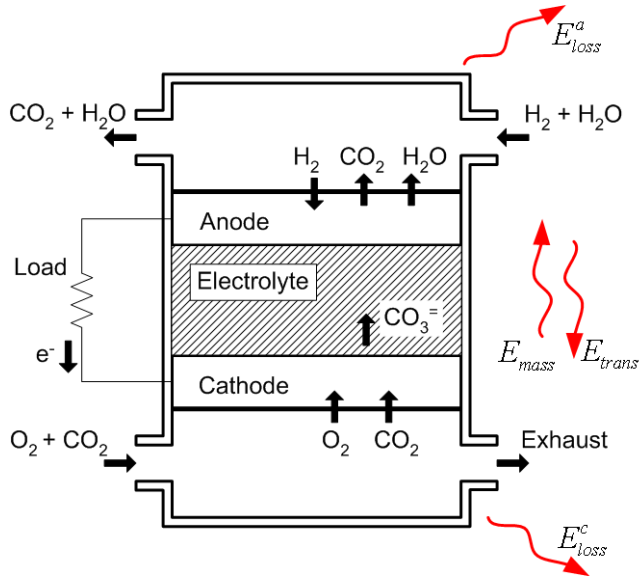

Figure 3-2 The simplified MCFC stack with internal energy dynamics.

3.1.2 A least-squares approach

The equations above suggest that the parameters to be determined are linear to the energy changing rates. Thus, these parameters can be estimated by a linear least squares approach [22].

The objective function

A objective function is defined below on energy errors, where E^a_{exp} and E^c_{exp} are the energy changing rates [8] calculated from experimental data by (3.8), and the superscript (i) indicates the i-th element in the sampled data set:

$$F_e = \sum_{i=1}^{N} \left[\left(E_{exp}^{a(i)} - E_{aug}^{a(i)} \right)^2 + \left(E_{exp}^{c(i)} - E_{aug}^{c(i)} \right)^2 \right] \tag{3.7}$$

$$E^{(i)} = N^{(i)} \sum_{k=1}^{7} x_k \left(A_k T^{(i)} + B_k T^{(i)2} + C_k T^{(i)3} + D_k T^{(i)4} \right) \tag{3.8}$$

In the energy calculation of a gas mixture, a fourth-order polynomial on temperature $T^{(i)}$ is used in (3.8), where x_k is the fraction of the *k*-th component in the gas mixture consisting of H_2, CH_4, CO, CO_2, H_2O, N_2, and O_2 in order; A_k, B_k, C_k, and D_k are the polynomial coefficients acquired by the integration of the specific heat capacity [8] of the *k*-th component in the mixture; and $N^{(i)}$ is the total mole flow rate of the gas mixture. Since the composition fractions can be obtained from simulation, the actual and simulated energy flow rates of the electrodes can be calculated from the experimental and simulation temperatures, respectively.

Solution of the least squares problem

According to the least squares approach, when the objective function is minimized, all partial derivatives of F_e to the parameters will be zeros, and the following conditions will be satisfied:

$$\frac{dF_e}{d\mathbf{K}} = \left[\frac{\partial F_e}{\partial K_{mass}} \quad \frac{\partial F_e}{\partial K_{trans}} \quad \frac{\partial F_e}{\partial K_{loss}^a} \quad \frac{\partial F_e}{\partial K_{loss}^c} \right]^T = \mathbf{0} \tag{3.9}$$

where

$$\mathbf{K} = \left[K_{mass} \quad K_{trans} \quad K_{loss}^a \quad K_{loss}^c \right]^T \tag{3.10}$$

By substituting F_e in (3.9) with (3.1) to (3.6), and simplifying the expressions into matrix form, the following equation can be concluded [22]:

$$\mathbf{F}^T\mathbf{F}\mathbf{K} = \mathbf{F}^T\mathbf{Y} \tag{3.11}$$

where

$$\mathbf{F} = \underset{2N\times 4}{\begin{bmatrix} \mathbf{R} & -\Delta\mathbf{T}_{a2c} & -\Delta\mathbf{T}_{a2amb} & \mathbf{0} \\ -\mathbf{R} & \Delta\mathbf{T}_{a2c} & \mathbf{0} & -\Delta\mathbf{T}_{c2amb} \end{bmatrix}} \tag{3.12}$$

$$\mathbf{Y} = \underset{2N\times 1}{\begin{bmatrix} \mathbf{E}^a_{exp} - \mathbf{E}^a_{org} \\ \mathbf{E}^c_{exp} - \mathbf{E}^c_{org} \end{bmatrix}} \tag{3.13}$$

Here, each element in $\mathbf{F}$ and $\mathbf{Y}$ is a $N\times 1$ vector containing N sample points of the corresponding experimental and/or simulation data, which are already known. The elements in the energy difference vector $\mathbf{Y}$ are calculated by [22]. Since the experiment and the simulation are conducted from the standby mode to full power mode, it can be guaranteed that $\mathbf{F}^T\mathbf{F}$ is a 4×4 nonsingular matrix. Therefore, the parameter vector $\mathbf{K}$ can be solved from (3.11).

Simulation and augmentation results

The supplementary internal dynamic model of the fuel-cell stack and the estimated parameter $\mathbf{K}$ are applied to the mathematical model. The simulation result on the augmented model with the least-squares approach is plotted and compared with the experimental data in Figure 3-3. It shows that the energy dynamics of the stack model has been augmented by calculating the anode and cathode energy separately. Contrasted with

Figure 3-1, the maximum anode temperature error is reduced from 50°C to 20°C; while the maximum cathode temperature error is reduced from 30°C to 10°C.

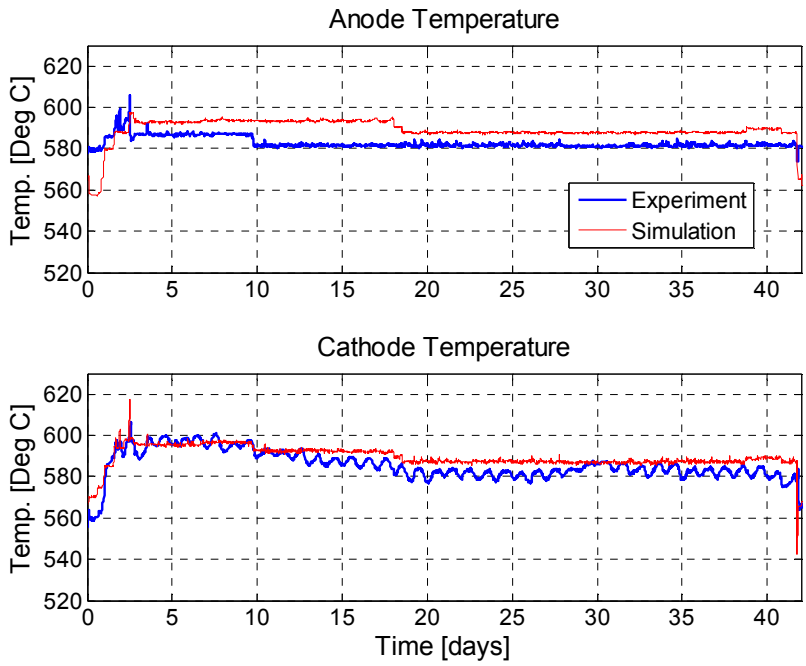

Figure 3-3 The augmentation result with a least-squares approach compared with the experimental result.

However, since the temperature is non-linear to energy or enthalpy, minimizing energy errors does not minimize temperature errors accordingly. Meanwhile, chemical balances of methane reforming and water/gas shifting [8] exist in the anode reactions, and are highly coupled with energy dynamics. The modifications to energy will affect the anode temperature, and consequently change the equilibrium point of the chemical reactions. Additional heat will be released or absorbed by these extra reactions, and finally fed back to the energy dynamic balances. As a result, the simulated temperature for the anode does not minimize, although reduces, the error as designed by using the least squares approach. Noticeable errors still exist between the simulation result and the

experimental data for the anode. Thus, the parameter vector $\mathbf{K}$ has to be further improved by minimizing the temperature errors directly.

3.1.3 A gradient descent approach

Although the parameter vector $\mathbf{K}$ is linear to energy flow rates, it is non-linear to the output temperatures, which are actually used to evaluate the accuracy of the mathematical model. To minimize the simulation errors on the output temperatures, a non-linear iterative optimization approach: the gradient descent method is applied.

The objective function

The objective function is defined below on temperature errors, where T_{exp}^{a}, T_{exp}^{c}, T_{sim}^{a}, and T_{sim}^{c} represent the electrode temperatures obtained by experiment and simulation, respectively, and the superscript (i) indicates the *i*-th data:

$$F_e\left(\mathbf{K}_k\right)=\sum_{i=1}^{N}\left[\left(T_{exp}^{a(i)}-T_{sim}^{a(i)}\left(\mathbf{K}_k\right)\right)^2+\left(T_{exp}^{c(i)}-T_{sim}^{c(i)}\left(\mathbf{K}_k\right)\right)^2\right] \tag{3.14}$$

where T_{sim}^{a} and T_{sim}^{c} are the temperature given by the mathematical model using the parameter vector $\mathbf{K}_k$ in simulation. Thus, the scalar F_e is a function of the variable vector $\mathbf{K}_k$. The subscript *k* indicates that the parameter vector is at the *k*-th iteration of the gradient descent algorithm, which is applied for searching the optimal $\mathbf{K}$ to minimize the objective function.

The gradient descent method

The gradient descent method is one of the most fundamental minimization methods for nonlinear optimization. It uses the negative gradient as its descent direction and finds the optimal step length to achieve the steepest descent. The algorithms are described as follows [23]:

Step 1: Set initial conditions for $\mathbf{K}_0$ and $k = 0$.

Step 2: Calculate the gradient of $F_e(\mathbf{K}_k)$,

$$\mathbf{g}_k = \nabla F_e(\mathbf{K}_k) = \frac{\partial F_e}{\partial \mathbf{K}}(\mathbf{K}_k) \tag{3.15}$$

Step 3: If $\|\mathbf{g}_k\| \le \varepsilon$, then stop, otherwise set $\mathbf{d}_k = -\mathbf{g}_k$.

Step 4: Find scalar α_k such that

$$F_e(\mathbf{K}_k + \alpha_k \mathbf{d}_k) = \min_{\alpha>0} F_e(\mathbf{K}_k + \alpha \mathbf{d}_k) \tag{3.16}$$

Step 5: Set $\mathbf{K}_{k+1} = \mathbf{K}_k + \alpha_i \mathbf{d}_k$, $k = k+1$, and go to *Step 2*.

In *Step 2*, the cost function F_e does not have an explicit expression on the parameter vector. Hence the gradient should be calculated by the following numerical differential method:

$$\frac{\partial F_e}{\partial K^{(i)}}(\mathbf{K}_k) = \frac{F_e(\mathbf{K}_k + \delta \mathbf{u}_i) - F_e(\mathbf{K}_k)}{\delta} \tag{3.17}$$

where $K^{(i)}$ is the *i*-th element of the parameter vector; $\mathbf{u}_i$ is the *i*-th unit vector; and δ is a small positive scalar. Thus, the partial differentials on each parameter will compose the gradient vector of the objective function F_e at the position $\mathbf{K}_k$.

In *Step 3*, ε is a positive scalar that defines the stop condition for the searching iterations. If the norm of the gradient vector is smaller than ε, it suggests that the surface of the objective function is flat at the point $\mathbf{K}_k$ and a minimum value has been reached. Otherwise, the negative gradient will be chosen as the descent direction $\mathbf{d}_k$.

The optimal step length

After the descent direction is determined, the minimum value of the objective function on this direction should be found. This task is accomplished in *Step 4* of the gradient descent algorithm, where $\mathbf{K}_k$ and $\mathbf{d}_k$ are fixed, and the cost F_e becomes a function of the scalar α, which is the descent step length. To find the optimal α_k to satisfy (3.16), the Golden Section Line Search Method [23] is used. The procedures are described below:

Step 1: Define a searching interval $[a_j, b_j]$ and set $j = 0$, $a_0 = 0$, $b_0 = \beta > 0$. Define a scalar function on α:

$$\phi(\alpha) = F_e\left(\mathbf{K}_k + \alpha \mathbf{d}_k\right) \tag{3.18}$$

Step 2: If the interval length $b_j - a_j < \varepsilon$, then stop, and take $\alpha_k = \left(a_j + b_j\right)/2$. Otherwise go to *Step 3*.

Step 3: At the iteration j, take two observations λ_j and μ_j in the searching interval $[a_j, b_j]$, such that

$$\lambda_j = a_j + 0.382(b_j - a_j) \tag{3.19}$$

$$\mu_j = a_j + 0.618(b_j - a_j) \tag{3.20}$$

Step 4: Evaluate $\phi(\lambda_j)$ and $\phi(\mu_j)$.

If $\phi(\lambda_j) \le \phi(\mu_j)$, set $a_{j+1} = a_j$, $b_{j+1} = \mu_j$, $\mu_{i+1} = \lambda_i$;

If $\phi(\lambda_j) > \phi(\mu_j)$, set $a_{j+1} = \lambda_j$, $b_{j+1} = b_j$, $\lambda_{i+1} = \mu_i$.

Set $j = j + 1$, and go to *Step 2*.

Since the parameter vector $\mathbf{K}_k$ and the descent direction $\mathbf{d}_k$ are both determined, for convenience in the expression, the objective function on the scalar α is represented as $\phi(\alpha)$ in (3.18). The parameters a_j and b_j, with the initial conditions 0 and a constant β, define the searching interval for α in the *j*-th iteration. In each iteration, two observations λ_j and μ_j will be taken at the golden section points of the interval $[a_j, b_j]$, and the interval will be shrunk by the ratio of 0.618 according to the conditions defined in *Step 4*. If the width of the interval is smaller than ε, then the optimal step length can be selected as the mean value of a_j and b_j, otherwise the iteration will continue.

Initial conditions and convergences

To guarantee the stability and convergence of the gradient descent iterations, the initial position of $\mathbf{K}_0$ should be selected close to the optimal solution $\hat{\mathbf{K}}$. Nevertheless, the parameter vector $\mathbf{K}$ obtained in Section 3.1.2 by the least squares approach is a quasi-optimal solution that can be applied as an ideal candidate for $\mathbf{K}_0$. Meanwhile, the algorithms require that the objective function $F_e(\mathbf{K}_k)$ has to be continuously

differentiable near $\mathbf{K}_k$, which is satisfied naturally since the dynamic equations are established based on a physical system.

There are no standard rules in choosing the initial value of β for the line search method. However, if β is too large, it will need more iterations in line search to find the optimal α_k; on the other hand, if β is too small, the optimal α_k may not be included in the searching interval, so that more iterations are required for the gradient descent method. Finally, the convergences of the gradient descent method and the golden section line search method have been proved in [23].

Simulation and augmentation results

By executing the algorithms presented above, the parameters are further improved. The objective function defined on temperature errors is minimized. The simulation result with the improved parameters in Figure 3-4 shows that the error of the anode temperature between the experimental data and simulation result is reduced considerably. In most of the simulation time, the errors are bounded in 5°C; while in the low power load, the errors are also limited under 15°C. Therefore, it can be concluded that the fuel-cell stack model has been augmented by developing an internal energy dynamic model and identifying model parameters with the lease squares approach and the gradient descent approach.

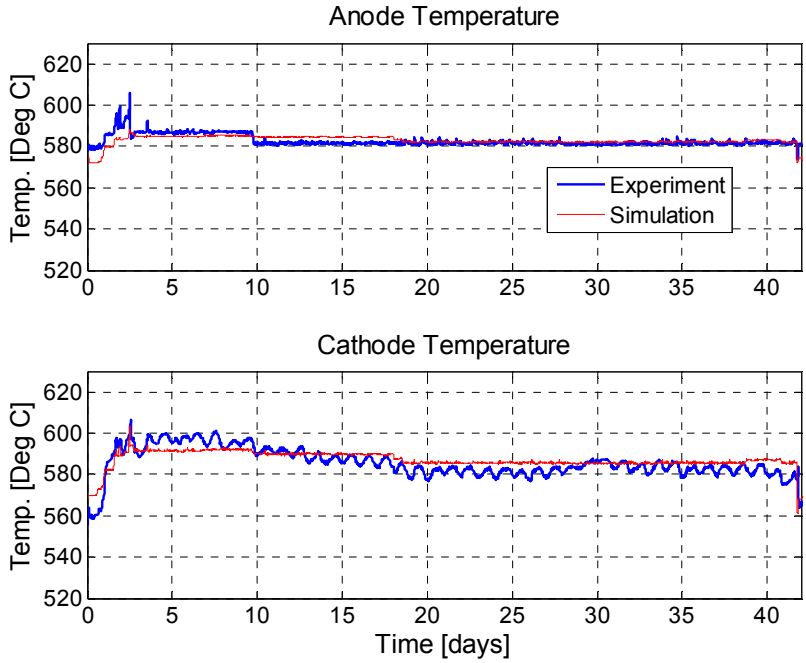

Figure 3-4 The augmentation result with a gradient descent approach compared with the experimental result.

3.2 A Numerical Augmentation Approach

Due to the assumptions of the mathematical model and the uncertainties of the DFC/T plant, the residuals still exist between the experimental data and the analytically augmented simulation result in Section 3.1. However, removing these assumptions may greatly increase the complexity of the fundamental model, and modeling uncertainties analytically is highly difficult. Thus, a numerical approach is applied to compensate these residuals and to further improve the dynamic model of the DFC/T plant.

As an advanced computational strategy, Artificial Neural Network (ANN) has shown its potential in nonlinear system modeling and controls [24]. With an ANN, a numerical model can be built based on only the input and output data of the actual system.

Because of these advantages, ANN is employed as an augmentation approach in this dissertation to enhance the accuracy of the plant model.

3.2.1 The augmentation algorithm

In the proposed model augmentation approach, ANN is used to estimate the residuals between the analytical model and the actual plant instead of modeling the entire dynamics of the power plant, which requires more complicated network structures and higher computational complexities. To minimize the size of the ANN, the whole plant is divided into 10 subunits, which is listed in Figure 2-4, besides the fuel-cell stack and the gas turbine. The augmentation algorithm with ANN in Figure 3-5 is implemented for each subunit, where y is the outputs of a particular subunit of the actual plant, and $\hat{y}$ is the corresponding outputs of the analytical model, which is simulated under the same inputs as the experiment.

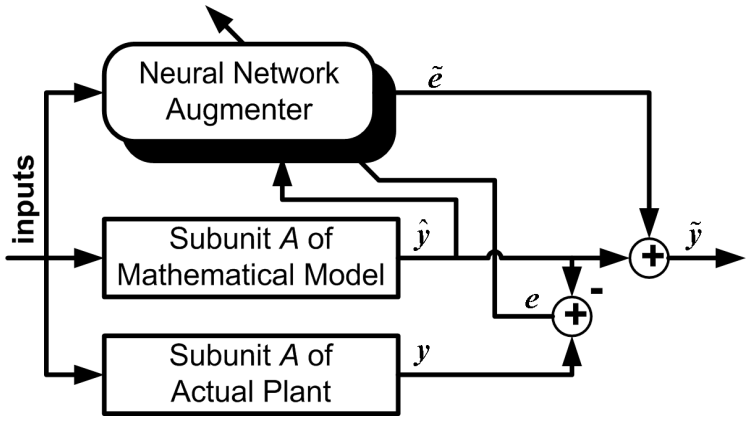

Figure 3-5 The structure of the neural network augmenter.

In the training mode, the residuals e between y and $\hat{y}$ are calculated and used to train the ANN. The neural network augmenter learns the error patterns regarding the

inputs of the subunit and the outputs of the mathematical model. In the running mode, the neural network augmenter will estimate the error $\tilde{e}$ based on the inputs and the simulation results, and compensates $\hat{y}$ to reduce the residuals.

The relationship presented in Figure 3-5 can be concluded by the equations below. During the training process, the output of the augmenter $\tilde{e}$ approaches to the simulation error *e*, as in (3.21). Meanwhile, in the running mode, the augmenter estimates the model error $\tilde{e}$ of the mathematical model and compensates the nominal output $\hat{y}$ to approximate the actual output y of the DFC/T plant.

$$\tilde{e} \xrightarrow{training} e = y - \hat{y} \tag{3.21}$$

$$\tilde{y} = \hat{y} + \tilde{e} \xrightarrow{estimating} \hat{y} + y - \hat{y} = y \tag{3.22}$$

3.2.2 Type of the ANN

The feedforward network with two layers (*i.e.,* one hidden layer and one output layer) is applied in the neural network augmenters. Tangent sigmoid functions are used for activation functions in the hidden layer, and linear activation functions are used for the output layer. The number of hidden neurons is selected slightly higher than twice of the number of inputs to keep complexity low and ensure accuracy.

Since most dynamics of the system have been modeled analytically by the mathematical model, this simple structure not only is adequate for the residual estimating, but also benefits the neural network augmenters. First, the feedforward structure with a reasonable size of hidden layers has a small number of parameters to be adjusted. Thus,

the training process can be kept in low computational complexity, and is applicable for online updating algorithms. Second, based on this simple neural network structure, the augmenters can only learn the major patterns of the model error and have low sensitivities to measurement noises. Therefore, the feedforward neural network is one of the best candidates for the model augmenters.

3.2.3 Training for neural networks

As described in Section 3.2.1, the neural networks are trained with the residuals between the experiment data and the simulation results. Thus, the capability of the training data set is limited by the availability of the experimental data. Forty-two days of the operational data on the DFC/T plant is provided, covering operational conditions from standby mode to full power mode. 70% of the data is used for training, while 30% is used to validate the performance of the ANNs.

The back-propagation method, which is highly efficient for feedforward networks and one of the most fundamental ANN training algorithms, is applied to the training process of the neural networks. Hence, the augmenter trained by this method can achieve high convergence rate with low computational complexity, and is capable for online updating, where high computational efficiency is required.

3.2.4 Simulation and augmentation results

To compare the performance of the numerical approach with the analytical approach and the original model, the simulation result is provided in Figure 3-6, where

the simulation data is too close to the experimental data to be clearly distinguished. Thus, the residuals between the simulation and the experiment are presented in Figure 3-7. It can be observed that the error of the augmented anode temperature is bounded in 1°C , while the error of the cathode temperature is reduced to 2°C with some brief instance of 3°C to 4°C.

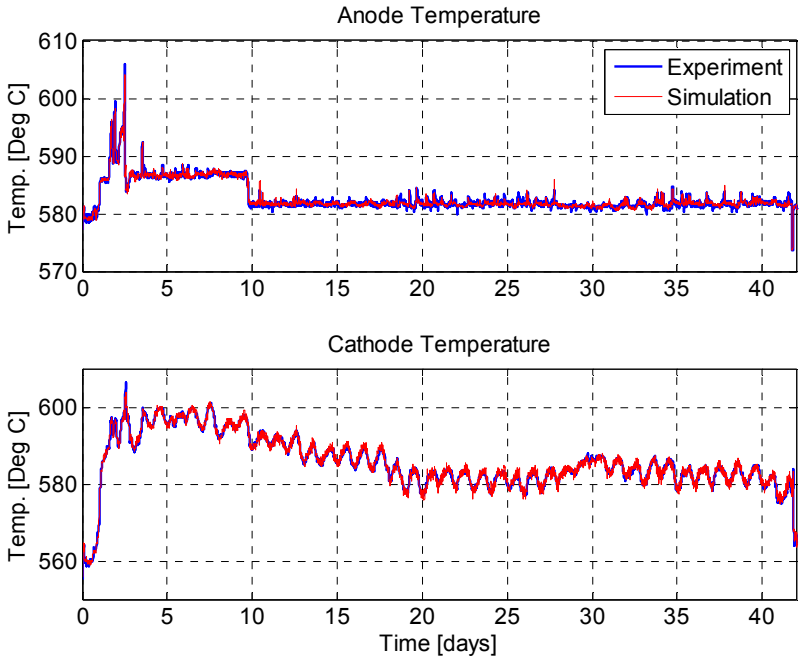

Figure 3-6 The augmentation result with a neural network approach compared with the experimental result.

Distinct from the previous figures of simulation errors, no evident patterns can be observed in Figure 3-7. The characteristic of the residuals is a zero-mean white noise, which implies that the error patterns of the mathematical model have been learned and compensated by the neural network augmenters. As a result, the accuracy of the DFC/T stack model is considerably improved by the numerical augmentation approach.

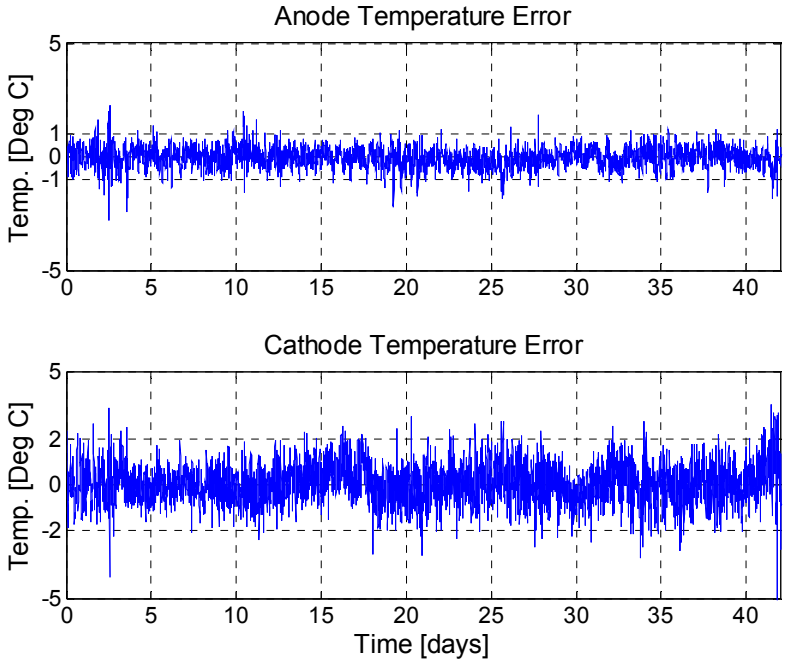

Figure 3-7 Stack temperature errors between the experimental data and augmentation result with artificial neural networks.

3.3 Augmentation Results on Other Subunits

To demonstrate the performance of the models enhanced by the various approaches introduced in Sections 3.1 and 3.2, the residuals of the augmented results for each subunit are calculated by

$$res_i^{(k)} = \frac{y_{sim\,i}^{(k)} - y_{exp\,i}^{(k)}}{y_{exp\,i}^{(k)}} \tag{3.23}$$

$$E = \left\| \left[\underset{1\times N}{\mathbf{res}^{(1)}} \quad \underset{1\times N}{\mathbf{res}^{(2)}} \quad \cdots \quad \underset{1\times N}{\mathbf{res}^{(M)}} \right] \right\|_2 \Big/ \sqrt{MN} \times 100\% \tag{3.24}$$

and compared with the original model in Table 3-1.

Equation (3.23) shows the *i*-th sampled relative error of the *k*-th output for a specific subunit, and $y_{sim\,i}^{(k)}$ and $y_{exp\,i}^{(k)}$ are the corresponding sample values of the simulation and experimental outputs. Kilo-Watt [kW] is used for the output power, and Kelvin [K] is used as the unit for the output temperatures, as the absolute temperature are actually used in the model simulations. A 2-norm is applied in (3.24) to evaluate the overall accuracy of the output vectors, where *M* residual vectors $\mathbf{res}^{(k)}$ with *N* elements each are combined to a long vector, *M* is the number of the outputs of a specific subunit, and *N* is the length of the sample data. The 2-norm is finally unified by the square root of *M* times *N*, which is the total number of the sample points. Thus, the relative errors listed in Table 3-1 are comparable to each other since they are in the same unified unit.

Table 3-1 Relative errors of the original and augmented model.

Subunits	Original Model [%]	Analytical Approach [%]	ANN Approach [%]
Stack	3.683	0.633	0.176
Turbine	12.929	4.809	0.891
HH	1.767	0.648	0.240
LTR	4.331	2.061	0.310
FP	1.318	0.906	0.078
PC	1.808	0.598	0.352
SP	1.280	0.302	0.064
SSH	8.371	3.995	0.676
HTR	2.956	0.461	0.111
AGO	2.728	1.603	0.707

Both the analytical augmentation approach and the numerical approach are applied to the 10 subunits of the DFC/T model. The unified residuals for the original fundamental model, the analytical augmentation approach, and the ANN augmentation approach are computed by (3.24) and listed in Table 3-1 in percentage. From comparison,

it can be observed that the errors of all subunits are decreased to less than 5% by the analytical approach, and further reduced to less than 1% by the ANN approach. Therefore, both the analytical approach and the numerical approach can effectively improve the accuracy of the mathematical model and are valid for all subunits.

3.4 The Model of Pressure Dynamics

The mathematical model of the DFC/T power plant was built with an assumption that the plant is operating with static pressures. The inlet and outlet pressures of all subunits are set to be constant to reduce the complexity of the model. However, gas pressure is one essential operational state of the dynamic system, and needs to be investigated with a mathematical model. In this section, a pressure model of the power plant is developed as a complement for the original mathematical plant model.

3.4.1 Pressure loss in pipelines

Due to the frictions and vortexes, the gas loses energy while traveling through a pipe. The energy loss is represented as pressure loss, which can be derived from fluid dynamic equations [25]:

$$P_{loss} = \xi \frac{R}{2A^2} \frac{M\dot{n}^2 T}{\overline{p}} \tag{3.25}$$

where

ξ pressure loss coefficient;

R universal gas constant;

A cross section of the pipeline;

M mole weight of the mixed gas;

$\dot{n}$ mole flow rate of the gas;

T gas temperature;

$\overline{p}$ average pressure of the gas through the pipe.

The coefficient ξ depends on the viscosity of the fluid, the length and roughness of the pipeline. For most instance, A, M, T, and $\overline{p}$ are nearly constant, and the pressure loss is mainly determined by the square of the mole flow rate $\dot{n}$.

Furthermore, for a certain pipeline or subunit, the pressure is calculated backward: the inlet pressure is determined by the outlet pressure and the pressure loss, which is opposite to the calculations for temperatures and component flow rates:

$$P_{in} = P_{out} + P_{loss} \tag{3.26}$$

3.4.2 Pressure control scheme

The DFC/T power plant has two major pressure controllers: anode back pressure controller and stack differential pressure controller [11], as shown in Figure 3-8. The first controller (PC1) regulates the anode pressure according to a constant setpoint of 1.1 bar (16 PSI) through a controllable valve. The second controller (PC2) maintains the differential pressure between the electrodes to 8×10^{-4} bar (0.012 PSI) with an electric blower, which boosts the cathode pressure to enhance mass transfer in the electrolyte. These two controllers compose the pressure control scheme of the direct fuel cell.

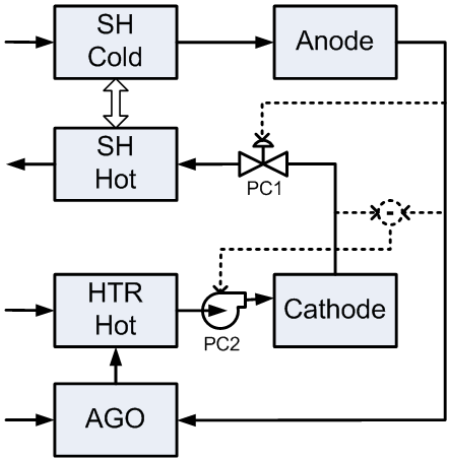

Figure 3-8 Pressure control scheme of the DFC/T power plant.

Anode back pressure control

The model of the anode back pressure control valve is shown in Figure 3-9, and represented by the following differential equations:

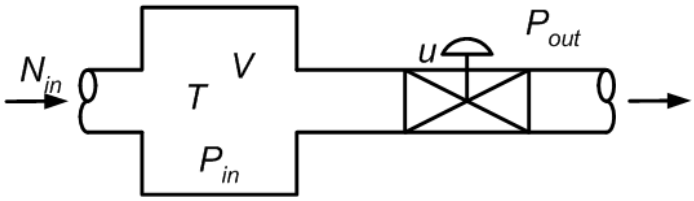

Figure 3-9 Simplified model of anode back pressure control valve.

$$N_{out} = \sqrt{\frac{P_{out} - P_{in}}{\Omega}} \times u \tag{3.27}$$

$$\dot{n} = N_{in} - N_{out} \tag{3.28}$$

$$P_{in} = \frac{nRT}{V} \tag{3.29}$$

where N_{in} and N_{out} are inlet and outlet flow rates; u is the control input limited from 0 to 1; V is the equivalent volume of the subunits prior to the pressure control valve; n is the mole number of the gas stored in the equivalent volume. Ω is the gas flow resistance:

$$\Omega = \xi \frac{R}{2A^2} \frac{MT}{\bar{p}} \tag{3.30}$$

Moreover, by combining (3.25)-(3.27) and (3.30), it can be concluded that:

$$N_{out} = N_0 \times u \tag{3.31}$$

where N_0 is the gas flow rate without any control constrains (*i.e.*, u=1). Actually, the input u controls the opening ratio of the valve, modifying the equivalent gas flow resistance of the valve, changing the gas flow rate, and consequently controls the anode back pressure.

Stack differential pressure control

The stack differential pressure control is realized by an electric blower driven by a variable frequency drive (VFD). The simplified model is shown in Figure 3-10. The only difference between the blower and the pressure control valve is that the gas outlet flow rate is directly determined by the control input u. The pressure model can be obtained by replacing (3.27) with:

$$N_{out} = u \tag{3.32}$$

It should be noticed that the actual model of an electric blower is an air compressor driven by an induction motor and a VFD, of which the gas flow rate is determined by the

rotational speed of the shaft. However, to reduce the complexity of the pressure model, the gas flow rate is assumed to be directly controlled. The compressor speed can be obtained from an nonlinear map of the gas flow rate and I/O pressures.

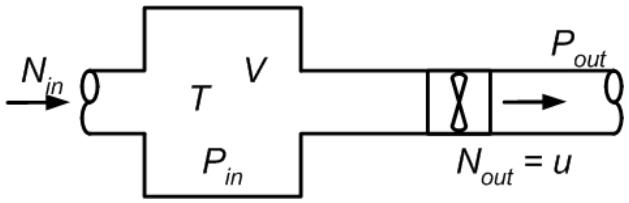

Figure 3-10 Simplified model of the blower for stack differential pressure control.

3.4.3 Pressure dynamics of the compressor-turbine system

In the original mathematical model of the hybrid power plant, the operating pressure of the air compressor and turbine are given by constants. However, pressure interactions and dynamics exist between the compressor and turbine. A simplified pressure model is shown in Figure 3-11, where $P_{C\_in(T\_out)}$ is the compressor inlet (turbine outlet) pressure; $N_{C\_in(T\_out)}$ is the compressor inlet (turbine outlet) air flow rate. P_{op} is the pressure of the air stored in the equivalent volume V and is called the operating pressure, which is both the compressor outlet pressure and the turbine inlet pressure. Here, P_{C_in} equals the ambient air pressure, which can be considered as a constant, and P_{T_out} is determined by the DFC pressure control scheme, which can be also assumed as a constant. Thus, P_{op} is the only pressure need to be investigated.

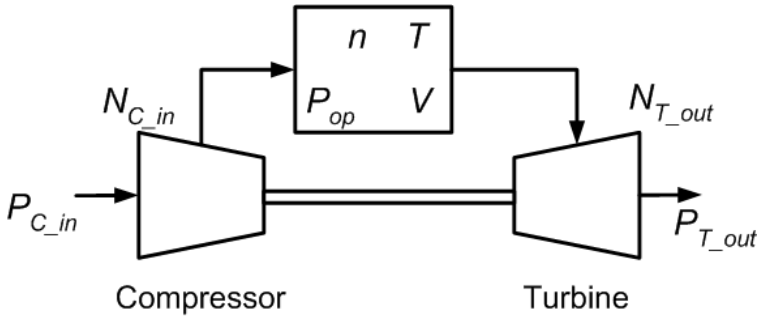

Figure 3-11 Simplified pressure model of the air compressor and air turbine.

The pressure dynamics of the stored air in the equivalent volume can be model as:

$$\dot{n} = N_{C\_in} - N_{T\_out} \tag{3.33}$$

$$P_{op} = \frac{nRT}{V} \tag{3.34}$$

The mole changing rate of the stored air is determined by the difference between the inlet and outlet air flow rates, and the operating pressure is in proportion to the mole number of the stored air when the temperature is constant or changing slowly.

Meanwhile, based on the compressor and turbine model in Section 2.5.4, the air flow rates of the compressor and turbine can be obtained from their inlet and outlet pressures, temperatures, and the rotational speed. Hence, by changing the operating pressure and the rotational speed under a constant temperature, two series of operating curves are obtained in Figure 3-12. The intersections of the compressor curves and the turbine curves are all located at the pressure of 3.7 bar, indicating that the compressor-turbine system will be operating at a constant pressure under the ideal conditions. With a low pressure, the inlet flow rate will be higher than the outlet flow rate, and the pressure will be built up according to (3.33) and (3.34). On the other hand, if the operating

pressure is higher than the steady pressure, the inlet flow rate will be lower than the outlet flow rate, and then the excessive air will be released to relief the operating pressure.

Furthermore, under a constant operating temperature, changing the rotational speed can only modify the air flow rate and will not affect the operating pressure. But actually, changing the speed will affect the operating temperature, and subsequently modifies the operating pressure in a certain range.

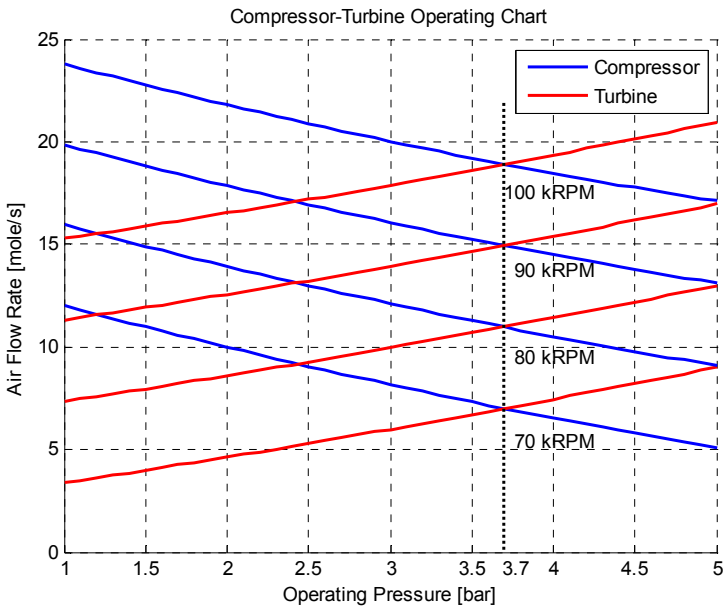

Figure 3-12 The operating curves of the compressor-turbine system.

The simulation results of the pressure control scheme and the pressure dynamics of the compressor-turbine system is shown in Figure 3-13. The plant operating status covers from the standby mode to the full power load, and the turbine rotational speed varies from 82 kRPM to 94 kRPM. The anode back pressure and the stack differential pressure are regulated according to constant setpoints with minor disturbances. The compressor inlet flow rate changes in proportion to the turbine rotational speed, and the

turbine operating pressure varies slightly around 3.7 bar. Hence, the pressure dynamic models are validated by the simulation results.

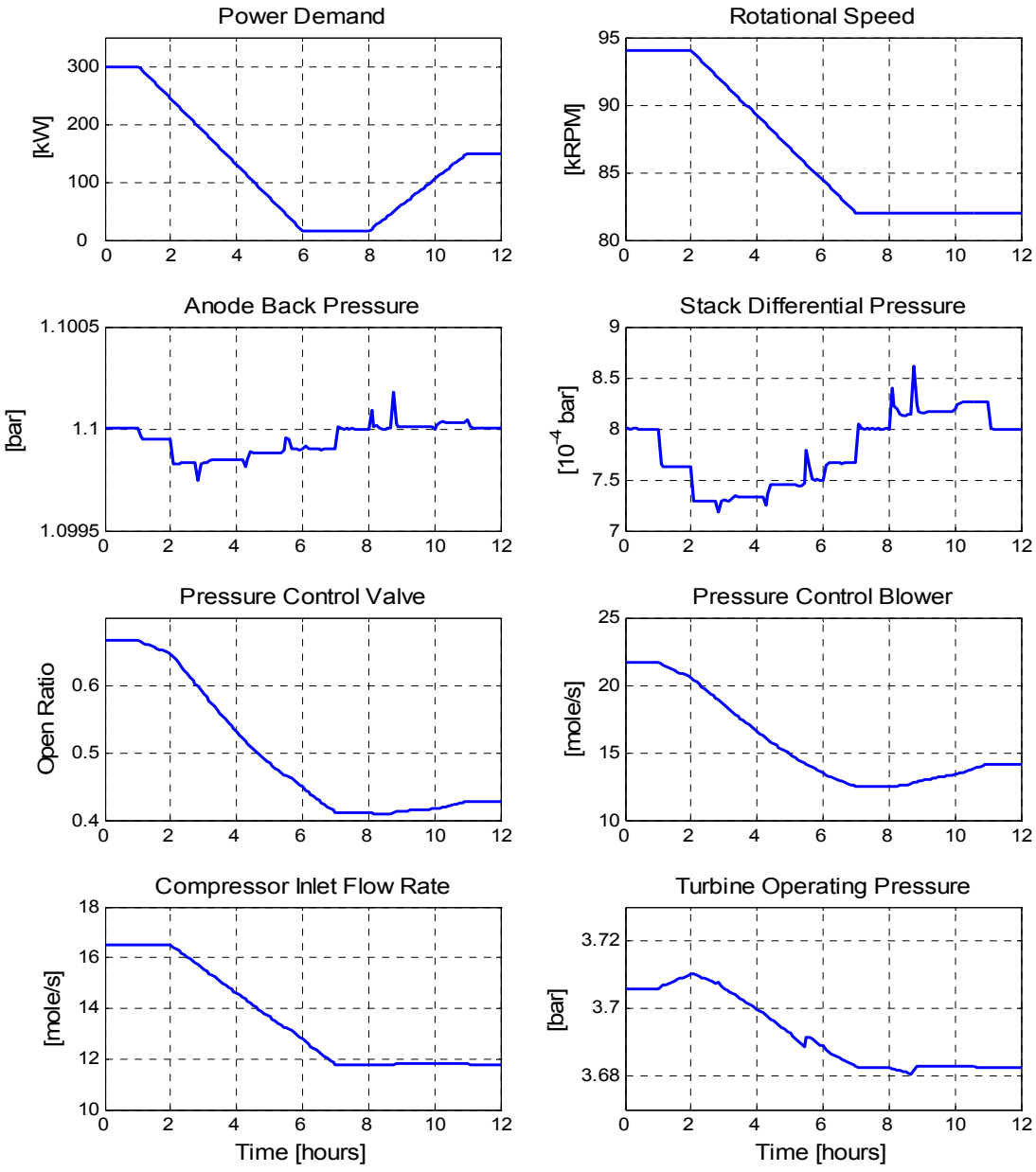

Figure 3-13 Simulation results of the pressure dynamic model.

Chapter 4

Modern Heuristic Optimization Techniques

Before developing the optimization framework for the DFC/T power plant, the optimization techniques should be firstly investigated. Because of the complexity of the hybrid power plant, the two classical optimization methods, *i.e.*, the least square approach and the gradient descent approach, used in Section 3.1 are no longer capable for the plant wide optimization problem. Thus, the modern heuristic optimizations, which are efficient for large scale nonlinear optimization problems, have to be studied.

Among a variety of heuristic optimization methods, Genetic Algorithm (GA) and Particle Swarm Optimization (PSO) are two fundamental algorithms that have been proven to be effective and are widely applied in the area of power and control systems[26]. GA and PSO, as well as multiple-objective optimization and other techniques will be reviewed in this chapter.

4.1 Genetic Algorithms

Genetic algorithm is a search algorithm based on the conjecture of natural selection and genetics. It operates on a population of individuals. Each individual is a potential solution to the given problem and is typically encoded a s a fixed-length binary string, which is an analogy with an actual chromosome. After an initial population is randomly or heuristically generated, the algorithm evolves the population through

sequential and iterative application of three operators: selection, crossover, and mutation. The execution of a GA iteration is basically a two-stage process. It starts with the current population. Selection is applied to create an intermediate population. Then, crossover and mutation are applied to the intermediate population to create the next generation of potential solutions [26]. The basic GA algorithm can be concluded as follows:

Step 1 - Initialization: Randomly generate an initial population of N chromosomes as $x_i \in \mathbb{S}$, i=1,2,...N, and $\mathbb{S}$ is the solution space of the optimization problem.

Step 2 - Fitness: Evaluate the fitness $f(x_i)$ of each chromosome x_i in the population.

Step 3 - New population: Create a new population by repeating following steps until the new population is complete:

- Selection: Select two parent chromosomes from a population according to their fitness. Usually, the better fitness, the bigger chance to be selected.
- Crossover: With a crossover probability cross over the parents to form a new offspring (children). If no crossover was performed, offspring is an exact copy of parents.
- Mutation: With a mutation probability mutate new offspring at each position in chromosome.
- Accepting: Place new offspring in a new population.

Step 4 - Replace: Use new generated population as the current population.

Step 5 - Stop: If the stop condition is satisfied, then stop and return the best solution in the population as the optimal solution for the problem.

Step 6 - Loop: Go to *Step 2*.

4.1.1 Encoding

In order to apply a GA to a given problem, the fist decision is the kind of genotype that the problem needs. That means how the parameters of the problem will be mapped into a finite string of symbols, known as genes, which encode a possible solution in the solution space. The issue of selecting an appropriate representation is crucial for the search. A binary alphabet, whose length is constant during the evolutionary process, is commonly used. In binary encoding, every chromosome is a string of bits, 0 or 1. All the parameters decode to the same range of values and are allocated the same number of bits for the genes in the string. [26]

4.1.2 Fitness function

Each string will be evaluated and assigned a fitness value after the creation of an initial population. The fitness function used by GA is distinct from the objective function. The objective function provides a measure of performance with respect to a particular set of gene values, independently of any other string. The fitness function transforms that measure of performance into an allocation of reproductive opportunities. The fitness of a string is defined with respect to other members of the current population. After decoding the chromosomes, each string is assigned a fitness value.

The fitness function is a black box for the GA. Internally, this may be achieved by a mathematical function, a simulator program, or a human expert that decides the quality of a string. At the beginning of the iterative search, the fitness function values for the population members are usually randomly distributed and widespread over the problem

domain. As the chromosome evolves, particular values for each gene begin to dominate, and the search will gradually converge to particular chromosomes. [26]

4.1.3 Basic operators

Selection

After a population is created and the fitness functions are evaluated, chromosomes should be selected from the current population as parents to generate new offspring for the next population. According to Darwin's evolution theory, high-fitness individuals have a better chance of reproducing, whereas low-fitness ones are more likely to disappear. The convergence rate of a GA is determined primarily by the magnitude of the selection pressure, which is the degree that the best individuals are favored [27]. Higher selection pressures imply higher convergence rates. If the selection pressure is too low, the convergence rate will be slow, and the GA will unnecessarily take longer to find a high-quality solution. If the selection pressure is too high, it is very probable that the GA will converge prematurely to a bad solution. A number of selection methods are concluded and investigated in [26, 28, 29], and will not be recited here.

Crossover

Crossover is a basic genetic operator that used to create new chromosomes from one generation to the next. It is analogous to reproduction and biological crossover. The type and implementation of crossover depends on the encoding method and the nature of the problem. For binary encoding, three crossover methods, *i.e.*, single point crossover,

two-point crossover, and uniform crossover, are commonly applied. In single point crossover, only one crossover point is selected. The binary string from the beginning of the chromosome to the crossover point is copied from one parent, and the rest is copied from the second parent. In two-point crossover, two crossover point are selected on both parents. The binary string from the beginning of the chromosome to the first crossover point is copied from one parent; the part between the two crossover points are copied from the second parent, and the rest is copied from the first parent. Uniform crossover is another recombination mechanism. Offspring is created by randomly picking each bit from either of the two parent strings. This means that each bit is inherited independently from any other bit [26, 30].

Mutation

Mutation is another basic genetic operator used to maintain genetic diversity from one generation to the next. It is analogous to biological mutation. In the case of binary encoding, mutation is carried out by flipping bits at random, with some small probability. For real-valued encoding, the mutation operator can be implemented by random replacement. Another possibility is to add/subtract a random amount [26]. The purpose of mutation is to allow the algorithm to avoid local minimum by preventing the population of chromosomes from becoming too similar to each other, thus slowing or even stopping evolution. This reasoning also explains the fact that most GAs usually take a random selection with a weighting.

4.2 Particle Swarm Optimization

PSO is another fundamental heuristic optimization technique firstly introduced by Kennedy and Eberhart in 1995 [31]. During recent decades, extensive investigations has been done to improve the performance of the PSO algorithm [32-34], and to expend it to solve multi-objective problems [35, 36]. The PSO-based algorithms were applied in many areas that need evolutionary computations, and are proven to be effective tools in solving large-scale nonlinear optimization problems in power systems engineering [37-39]. In this section, the formulation of the optimization problem is presented, and several PSO-based optimization algorithms are discussed.

4.2.1 The basic PSO algorithm

The PSO was originally developed through the simulation of bird flocks in a two-dimensional space, and then extended to a hyperspace. Each bird (called particle) is trying to find the best position that minimize a certain scalar objective function. The position of a particle is represented by a point in the hyperspace, and the velocity of the particle is similarly defined. These particles fly through hyperspace and have two essential reasoning capabilities: their memory of their own best position and knowledge of the global best. In a minimization problem, "best" simply means the position with the smallest objective value. The particles adjust their own positions and velocities based on these memories to find the best position. This is an analogy of the personal experience of a particle. A particle knows the situation and history of itself and how other particles have

performed. Each particle tries to modify its position using the concept of velocity to minimize the objective function and find the best position.

Assume there are N particles in an m-dimensional hyperspace, and an objective function defined on the space as $f:\mathbb{R}^m \to \mathbb{R}$. Each of the particles is associated with a position $\mathbf{x}_i^k$ and a velocity $\mathbf{v}_i^k$:

$$\mathbf{x}_i^k = \left(x_{i,1}^k, x_{i,2}^k, \cdots x_{i,m}^k\right) \in \mathbb{R}^m \tag{4.1}$$

$$\mathbf{v}_i^k = \left(v_{i,1}^k, v_{i,2}^k, \cdots v_{i,m}^k\right) \in \mathbb{R}^m \tag{4.2}$$

where i=1,…,N, k is the iteration number.

The new position of each particle for the next iteration is calculated according to the concept of velocity, where the new position is obtained by adding the current velocity to the current position.

$$\mathbf{x}_i^{k+1} = \mathbf{x}_i^k + \mathbf{v}_i^k \tag{4.3}$$

The velocities for the next iteration can be updated as:

$$\mathbf{v}_i^{k+1} = w\mathbf{v}_i^k + c_1\mathbf{r}_1^k \circ \left(\mathbf{x}^{*k} - \mathbf{x}_i^k\right) + c_2\mathbf{r}_2^k \circ \left(\mathbf{x}_i^{*k} - \mathbf{x}_i^k\right) \tag{4.4}$$

where w is a weighting factor, an analogy of the inertia of a particle, keeping the particle flying at its original velocity; c_1 and c_2 are two weighting factors that determine the updating speed for velocities; and $\mathbf{r}_1^k$ and $\mathbf{r}_2^k$ are two m-dimensional random vectors following uniform distribution, and introduce random factors to the search algorithm. The operator "$\circ$" indicates element-by-element product, and $\mathbf{x}^{*k}$ and $\mathbf{x}_i^{*k}$ are the global best

and the local best, respectively. The global best is the best position achieved by any particles so far at the *k*-th iteration. The local best is the best position achieved only by the *i*-th particle so far at the *k*-th iteration. They are defined as:

$$\mathbf{x}_i^{*k} : f\left(\mathbf{x}_i^{*k}\right) = \min_{j=1,2,\cdots k} f\left(\mathbf{x}_i^{j}\right) \tag{4.5}$$

$$\mathbf{x}^{*k} : f\left(\mathbf{x}^{*k}\right) = \min_{i=1,\cdots,N} f\left(\mathbf{x}_i^{*k}\right) \tag{4.6}$$

The basic AGO algorithm can be summarized in the following steps:

Step 1: Initialize $\mathbf{x}_i^1$ and $\mathbf{v}_i^1$ for all *i*. Usually take $x_{i,j}^1 \in U\left[a_j,\ b_j\right]$, where a_j and b_j are the lower and upper limits of the search space/operating window of each dimension.

Step 2: Let the local best $\mathbf{x}_i^{*k} = \mathbf{x}_i^1$, and the global best $\mathbf{x}^{*k} = \text{aug}\min_{i=1,\cdots,N} f(\mathbf{x}_i^1)$.

Step 3: For each particle, do

- Create random vectors $\mathbf{r}_1^k$ and $\mathbf{r}_2^k$, by taking $r_{1,j}, r_{2,j} \in U[0,1]$.
- Update the particle velocities according to (4.4).
- Update the particle positions according to (4.3).
- Update the local best: If $f(\mathbf{x}_i^{k+1}) < f(\mathbf{x}_i^{*k})$, $\mathbf{x}_i^{*k+1} = \mathbf{x}_i^{k+1}$; otherwise $\mathbf{x}_i^{*k+1} = \mathbf{x}_i^{*k}$.
- Update the global best: If $f(\mathbf{x}_i^{k+1}) < f(\mathbf{x}^{*k})$, $\mathbf{x}^{*k+1} = \mathbf{x}_i^{k+1}$.

Step 4: If converged, stop iteration, and $\mathbf{x}^{*k}$ is the optimal solution of the problem. Otherwise, *k*=*k*+1, go to *step 3*.

4.2.2 The modified PSO algorithm

Hybrid PSO (HPSO)

The HPSO [32] utilizes the basic mechanism of the PSO and the natural selection mechanism. Since the search procedure by the PSO depends strongly on the global best and the local best, the search area would be limited by them. On the other hand, by introducing a natural selection mechanism, the effects of the global best and local best are weakened and the search area will be broader. Particle positions with poor performance are replaced by those with better performance in the selected particles. The information of local best of each particle is still maintained. Therefore, both intensive searches in an effective area and the dependence on the past high performance positions are realized at the same time.

Evolutionary self-adapting PSO (EPSO)

The major differences between EPSO [33] and the basic PSO are a selection procedure and self-adapting properties for its parameters. Instead of moving the particles to find an optimal solution in the solution space, EPSO reproduces the particles with the movement rule and the mutation rule of Evolutionary Strategy (ES). Then, the best particles are selected stochastically through the evaluation. The general scheme of EPSO is replication, mutation, and reproduction with movement rule, evaluation, and selection. Furthermore, EPSO can also be classified as a self-adaptive algorithm, because it relies on the mutation and selection of strategic parameters. However, EPSO has a drawback of requiring 2 evaluations per particle per iteration.

Constriction factor approach (CFA)

The CFA [34] applies the velocity of the constriction factor approach in the basic PSO as follows:

$$\mathbf{v}_i^{k+1} = K\left[w\mathbf{v}_i^k + c_1\mathbf{r}_1^k \circ \left(\mathbf{x}^{*k} - \mathbf{x}_i^k\right) + c_2\mathbf{r}_2^k \circ \left(\mathbf{x}_i^{*k} - \mathbf{x}_i^k\right)\right] \tag{4.7}$$

$$K = \frac{2}{\left|2 - \varphi - \sqrt{\varphi^2 - 4\varphi}\right|}, \text{ where } \varphi = c_1 + c_2,\ \varphi > 4 \tag{4.8}$$

The factor K is smaller than 1, and constrict the velocities of particles. The constriction factor considers the dynamic behavior of each particle and the effect of the interaction among particles. The CFA ensures the convergence of the search procedure. Thus, it can generate higher quality solutions than the conventional PSO approach.

4.3 Multiple-Objective Optimization Algorithms

The previous algorithms all focus on the single-objective optimization problem, in which the objective function is a scalar $f : \mathbb{R}^m \to \mathbb{R}$. However, most engineering problems have more than one criteria need to be optimized and considered coordinatively. The multiple-objective functions can be represented as a vector function $f : \mathbb{R}^m \to \mathbb{R}^n$, where n is the number of criteria/objective functions. To conduct the these problems, different multiple-objective (MO) optimization algorithms were developed [35, 36, 40-46]. Compared with single-objective (SO) problems, which have a unique solution, the solution to MO problems consists of sets of trade-offs between objectives.

4.3.1 The weighted aggregation approach

The weighted aggregation is the most common approach, where all objectives are converted into a SO function. The objectives are summed to a weighted combination:

$$F = \sum_{i=1}^{n} w_i F_i(\mathbf{X}) \tag{4.9}$$

where w_i, i=1,2,…,n, are non-negative weights. Usually, the sum of the weights equals 1. These weights can be either fixed or dynamically adapted during the optimization.

If the weights are fixed, then it is called Conventional Weighted Aggregation (CWA). Using this approach, all optimization algorithms for SO problems can be used, and only one optimal solution will be obtained each time. Extra knowledge is required to choose the appropriate weights. If a number of candidate solutions are desired, the search has to be repeated several times, which is time consuming and computationally expensive.

If the weights are changing continuously during the optimization, it is called Dynamic Weighted Aggregation (DWA). The slow change of the weights forces the optimizer to keep looking for new optimal candidates. The collection of the global bests during the optimization process provides a set of optimal candidates for the MO problem. The performance of DWA for 2-dimensional cases was verified in [36, 42], but the weight functions are hard to design for the problems with higher dimensions.

4.3.2 The Pareto dominance approach

An alternative to the weighted aggregation approach is a MO algorithm using the concept of Pareto dominance, by which the term "better" is redefined. With a scalar

objective $f:\mathbb{R}^m \to \mathbb{R}$, A is better than B simply means $f(A) < f(B)$. In contrast, under a MO function $f:\mathbb{R}^m \to \mathbb{R}^n$, A is better than B, or A dominates B, if each element of $f(A)$ is no greater than the corresponding element of $f(B)$, and at least one element of $f(A)$ is strictly smaller than the element of $f(B)$. This relationship can be formulated as:

$$\begin{aligned} &\forall i = 1, \cdots n, \text{ that } f_i(A) \le f_i(B), \text{ and} \\ &\exists j = 1, \cdots n, \text{ that } f_j(A) < f_j(B) \end{aligned} \tag{4.10}$$

As a two-dimensional example in Figure 4-1, A is better than B, because $f_1(A)<f_1(B)$ and $f_2(A)<f_2(B)$, and B is called "dominated by A." However, C is nondominated by A, since $f_1(C)<f_1(A)$. Meanwhile, A is nondominated by C, since $f_2(A)<f_2(C)$. Furthermore, there exists a set of particles that are nondominated by any presenting particles in the plane. This set of particles is named Pareto Frontier. The goal of the MO algorithm is to find a Pareto Frontier for the optimization problem.

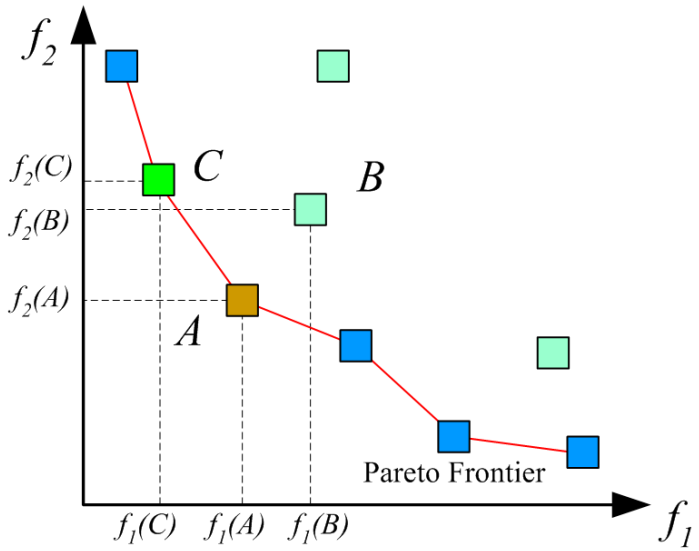

Figure 4-1 A two-dimensional example of Pareto frontier.

Taking MOPSO as an example [35], the global best is replaced by a global repository containing the Pareto Frontier, a set of nondominated particles, obtained so far. After each flying cycle, the particles neither dominated by the peer particles, nor dominated by any particles in the repository will be added to the repository. Any stored particles that are dominated by the newly entered particles will be removed from the repository. The global repository is used as a guide of the PSO search process [35].

The Pareto dominance approach can be summarized as the following steps:

Step 1: Initialize $\mathbf{x}_i^1$ and $\mathbf{v}_i^1$ for all i=1,…,N.

Step 2: Evaluate each of the particles, store the positions of all nondominated particles in the repository *REP*.

Step 3: Initialize the local best: $\mathbf{x}_i^{*k} = \mathbf{x}_i^1$

Step 4: For each particle, do

- Create random vectors $\mathbf{r}_1^k$ and $\mathbf{r}_2^k$, by taking $r_{1,j}, r_{2,j} \in U[0,1]$.
- Update the particle velocities according to (4.4). The global best $\mathbf{x}^{*k}$ is randomly selected from *REP*.
- Update the particle positions according to (4.3).
- Evaluate each of the particles.
- Update the local best: If $\mathbf{x}_i^{*k}$ is dominated by $\mathbf{x}_i^{k+1}$, $\mathbf{x}_i^{*k+1} = \mathbf{x}_i^{k+1}$; if $\mathbf{x}_i^{k+1}$ is dominated by $\mathbf{x}_i^{*k}$, $\mathbf{x}_i^{*k+1} = \mathbf{x}_i^{*k}$. If $\mathbf{x}_i^{k+1}$ and $\mathbf{x}_i^{*k}$ are nondominated by each other, choose one of them randomly as the local best.

- Update the repository: If $\mathbf{x}_i^{k+1}$ is nondominated by any $\mathbf{x}_j^k, j=1,\ldots,N,\ j \neq i$, and any $\mathbf{x} \in REP$, add $\mathbf{x}_i^{k+1}$ to *REP*. Then, if any $\mathbf{x} \in REP$ is dominated by $\mathbf{x}_i^{k+1}$, remove $\mathbf{x}$ from *REP*.

Step 5: If maximum iteration number reached, stop algorithm, the particles in *REP* are the candidate solutions for the problem. Otherwise, set $k=k+1$, go to *step 4*.

4.4 Other Heuristic Optimization Techniques

4.4.1 Evolution strategies and evolutionary programming

Evolution strategies (ES) employ real-coded variables and originally relied on mutation as the search operator with a population size of one. Then, it has evolved to share many features with the GA. Both of they maintain populations of potential solutions and use a selection mechanism for choosing the best individuals from the population. The main differences are ES operates directly on floating-point vectors, whereas classic GAs operate on binary strings. GAs rely mainly on recombination to explore the search space, whereas ES uses mutation as the dominant operator.

Evolutionary programming (EP) is a stochastic optimization strategy similar to a GA that places emphasis on the behavioral linkage between parents and their offspring. EP is similar to ES, although the two approaches developed independently. EP is a useful method of optimization when other techniques such as gradient descent or direct analytical discovery are not possible [26].

4.4.2 Simulated annealing

The name simulated annealing (SA) originates from the analogy with the physical process of solids. The analogy between physical system and simulated annealing is that the cost function and the solution in the optimization process correspond with the energy function and the state of statistical physics, respectively. In a large combinatorial optimization problem, an appropriate perturbation mechanism, cost function, solution space, and cooling schedule are required in order to find an optimal solution.

In the simulated annealing method, each point in the search space is analogous to a state of some physical system, and the objective function to be minimized is analogous to the internal energy of the system in that state. The goal is to bring the system, from an arbitrary initial state, to a state with the minimum possible energy. At each step, the SA heuristically considers some neighbors of the current state, and probabilistically decides between moving the system to the new state or staying in the current state. The probabilities are chosen so that the system ultimately tends to move to states with lower energy. Typically this step is repeated until the stop conditions are satisfied.

Because of the implementation simplicity, high performance, and low computational complexity, PSO algorithms, including both SOPSO and MOPSO methods, are finally selected as the core algorithms for the optimization framework for the DFC/T power plant. These PSO algorithms will be implemented and investigated in the next chapter.

Chapter 5

Online Optimal Reference Governor

Because of high energy conversion efficiency and long startup time [16], the DFC/T power plant is more suitable for a base-load power source, which keeps running at full load throughout the year, than for a peak-load source that requires fast responses. Thus, even a small improvement in fuel efficiency will provide significant economic benefits in the long run. However, the power plant cannot reach high efficiency without a proper control system. For example, excessive fuel in the system will generate heat instead of electric power, and will consequently decrease the plant efficiency. Therefore, optimal control is an essential issue for the proposed intelligent control system. In this chapter, an Optimal Reference Governor (ORG) is developed for the DFC/T power plant to improve the energy conversion efficiency from the perspective of control systems.

Extensive optimization research has been conducted for the hybrid power plant by researchers and investigators. The optimal off-line trajectory planning algorithm was introduced in [14], where Radau collection and large scale nonlinear programming solvers were used to solve the optimal control solutions. Since the nonlinear programming algorithm is computationally expensive, a Neural Network Supervisor (NNS) [15] was developed to estimate the optimal trajectories based on given load profiles. Diagonal recurrent neural networks (DRNN) [47] were trained by the dynamic back-propagation method and the data obtained from the off-line optimization results in [14]. The NNS provides optimal setpoints and feedforward controls with less

computational complexity. However, the computational time needed by the nonlinear programming algorithm makes it incapable of real-time applications. The neural network supervisor may give invalid results if the operational patterns were not learned during the training phase. Thus, a fast approach for online optimization is necessary for the intelligent control system of the hybrid power plant.

5.1 The Structure of the Optimal Reference Governor (ORG)

The objective of the optimal reference governor (ORG) is to find appropriate feedforward controls and setpoints that guarantee the efficient and reliable operations of the power plant. Toward this goal, an ORG is developed as in Figure 5-1, where the optimized setpoints and feedforward controls, including current density (I^2), methane flow rate (n_CH_4), turbine speed (RPM), power of the second-startup heater (q_SSH), LTR control move (u_LTR), and AGO control move (u_AGO), are generated based on a given load demand.

The core of the ORG is a Multi-objective Optimization Module (MOM) that generates the optimal setpoints and feedforward controls. The particle swarm optimization (PSO) [31, 48], which is a stochastic, population-based heuristic optimization algorithm, has been proven to be a powerful tool for solving large scale optimization problems in power systems [37-39]. Thus, PSO is utilized as the main algorithm for the ORG. The objective functions for the optimization problem include fuel efficiency and tracking errors representing how the output power or temperature follows the power demand or setpoints. The operating window provides possible operational

ranges for the load-dependent setpoints, serving as the solution space or search space for the multi-objective optimization algorithm.

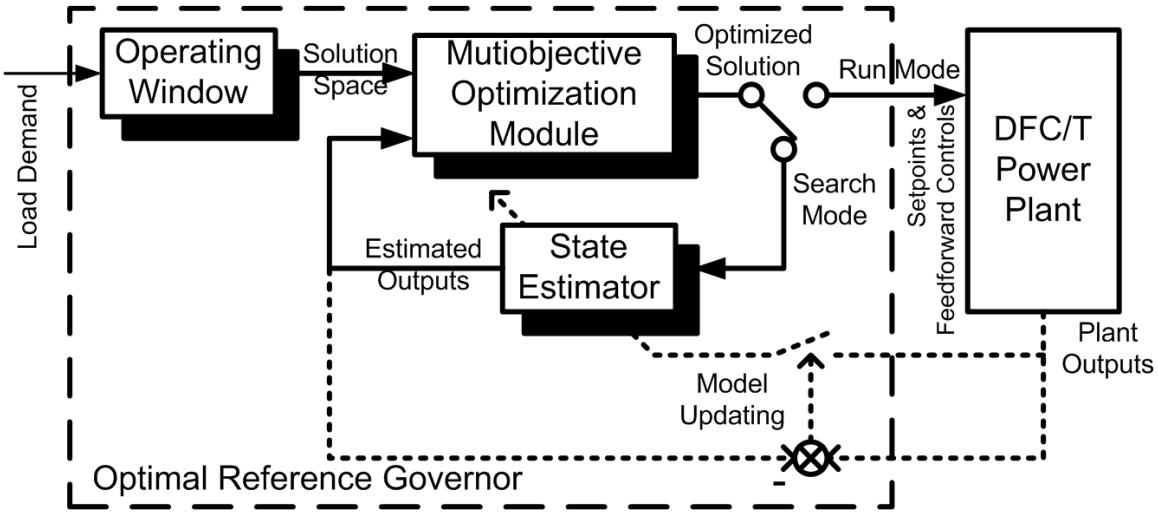

Figure 5-1 Block diagram of the optimal reference governor.

There are three possible phases, *i.e.,* search mode, run mode, and model updating mode, during the operations of the ORG. In the search mode, the candidate setpoints provided by the MOM will be tested by the online state estimator, which is realized by neural networks and estimates the outputs of the power plant under the given setpoints. Then, the objective functions will be evaluated based on these estimated outputs, and used by the MOM to refine the setpoints. After several search iterations, the ORG will switch to the run mode, where the optimized setpoints will be given to the local controllers as the references for plant operations. Then, the outputs of the actual plant are compared with the estimated outputs of the online state estimator. If significant errors are detected in the estimated outputs, the ORG will enter the model updating mode, where the online state estimator will be retrained with the newly obtained operating data. After the estimator is updated, the searching process will be executed again to ensure the

validity of the optimization results. With this structure, the optimal setpoints and feedforward controls can be determined for the optimal control of the power plant, and the plant estimator can be updated as required.

5.2 The Online State Estimator

The MOM needs to work with a plant model that estimates the steady-state outputs of the system under given setpoints. The original mathematical model is a "series" model, where the system states must change continuously, and only one set of setpoints can be tested at a single time. Thus, the mathematical model is not suitable for the heuristic population based algorithms, such as particle swarm optimization, which requires that the model can process multiple sets of setpoints in "parallel". Therefore, a special "parallel" model has to be developed to cooperate with the MOM.

The online state estimator is realized by artificial neural networks (ANN) as a simplified plant model that fulfills the requirements of the MOM and the ORG framework. The ANNs are non-linear statistical modeling tools, and have become an important role for system modeling and control system design in the area of power systems [49, 50]. Because the neural network model depends only on the input and output data, not the structure of the system, it is flexible and can easily be adapted to different types of power plants and control systems. In this section, neural network models are developed and trained for each subsystem of the power plant, and then a neural network combined model (NNCM) [49] is obtained as the online state estimator by integrating the models of the subsystems.

5.2.1 Definition of subsystems and streams

The DFC/T power plant is a nonlinear multi-input multi-output (MIMO) system, which is highly complicated that can hardly be modeled with a single neural network. The system inputs consist of 6 series of setpoints and feedforward controls, and the outputs include gas components, temperatures, and power of each subunit. To reduce the complexity of the state estimator, the whole system is divided into 7 subsystems, for each of whom, a neural network model will be built. As marked by the shadowed blocks in Figure 5-2, these 7 subsystems are:

- Humidifying Heat Exchanger (HH)
- Low Temperature Recuperator (LTR) + Second Startup Heater (SSH)
- Fuel PreHeater (FP) + Pre-Converter + Super Heater (SP)
- Fuel Cell Stack (Anode + Cathode)
- Gas Turbine (Compressor + Turbine)
- High Temperature Recuperator (HTR)
- Anode Gas Oxidizer (AGO)

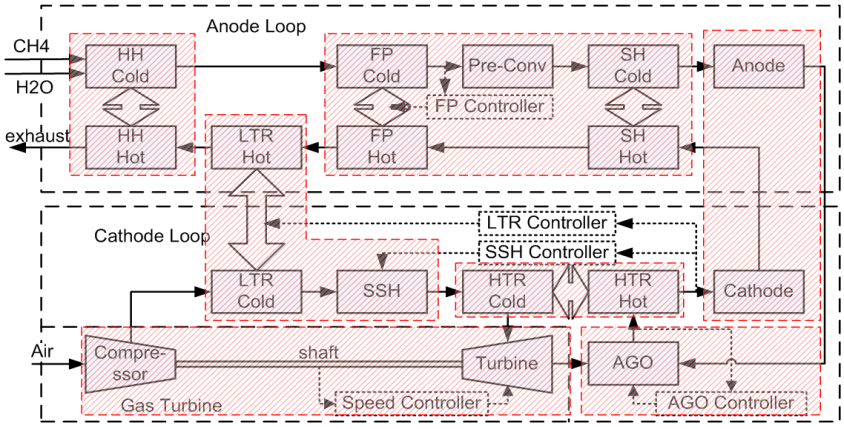

Figure 5-2 Definition of subsystems for the DFC/T power plant.

According to the definitions above, each subsystem has a common input/output representation described in Figure 5-3, where the inputs include two inlet streams and one control input (optional), and the outputs include two outlet streams and the generated or consumed power (optional). The characteristics of the inlet/outlet streams are described by the mole flow rates (*xN*) of each stream component , the stream temperature (*T*), and the stream pressure (*P*). With this common structure, one NN framework will be applicable to all the 7 subsystems, so that the complexity of the state estimator can be reduced. Meanwhile, the subunits connected in a row (*e.g.*, FP, Pre-Conv, and SH), are combined into one subsystem to reduce the number of the neural networks.

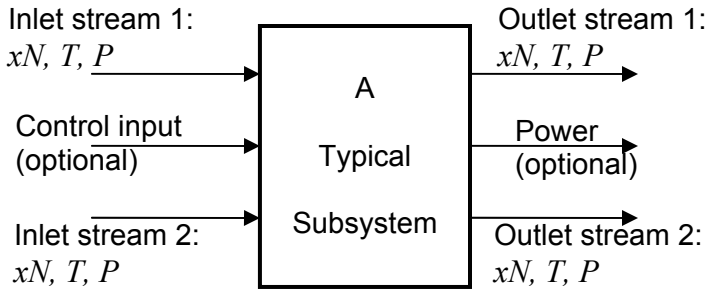

Figure 5-3 Common input/output representation of each subsystem.

To clarify the input/output relationships between the subsystems, the system streams are identified by the numbers in brackets in Figure 5-4. The dotted arrows without numbers indicate internal streams that are modeled within specific subsystems and are not considered as independent system streams. These assigned numbers are used to recall the system streams in the neural network models and the state estimator. The output of the state estimator can be arbitrarily selected from these streams. These 16 system streams are:

Stream #1: HH fuel inlet – raw fuel (methane and water)

Stream #2: HH cold outlet, FP cold inlet – pre-heated fuel

Stream #3: SP cold outlet, Anode inlet – prepared fuel

Stream #4: Cathode outlet, SP hot inlet – cathode off gas

Stream #5: FP hot outlet, LTR hot inlet – reused cathode off gas

Stream #6: LTR hot outlet, HH hot inlet – reused cathode off gas

Stream #7: HH hot outlet – exhaust gas to the environment

Stream #8: Compressor inlet air – fresh air

Stream #9: Compressor outlet air, LTR cold inlet air – compressed cool air

Stream #10: SSH outlet air, HTR cold inlet air – pre-heated compressed air

Stream #11: HTR cold outlet air, turbine inlet air – hot compressed air

Stream #12: turbine outlet air, AGO air inlet – turbine exhaust air

Stream #13: Anode outlet gas, AGO fuel inlet – anode off gas

Stream #14: AGO outlet gas, HTR hot inlet – oxidized hot gas

Stream #15: HTR hot outlet, AGO mixer inlet – reused hot gas

Stream #16: AGO mixer outlet, Cathode inlet – oxidizer for fuel cells

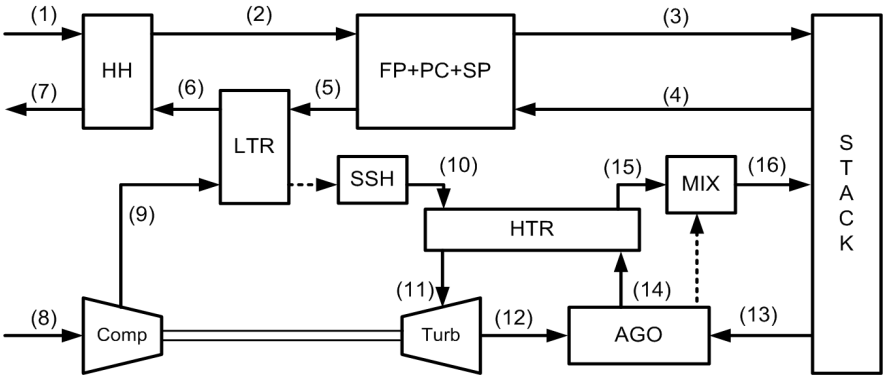

Figure 5-4 Definition of system streams of the state estimator.

5.2.2 Preparation of training data

The neural network model for each subsystem needs to be trained with either operational data or simulation data containing the dynamic behaviors of the power plant. In this study, due to the limitation of the operational data, the neural network models are trained with the data generated by the mathematical model. The data used for NN training should possess as much system characteristics as possible, so that the NN model would learn more information and operational patterns to achieve better performance. Hence, the inputs of the simulation should be carefully designed for NN training.

The designed inputs for simulation are shown in Figure 5-5, which covers the operational status from full load to half load. The current density setpoint *I2* steps from 140 down to 60 mA/cm^2 with 10 mA/cm^2 decrements. The CH_4 setpoint and the turbine speed setpoint vibrate repeatedly according to different current density levels, and try to cover most operational regions. The AGO temperature setpoint keeps constant, in which case the AGO control move will have a broad operational range because of the closed-loop PI controller and the variations of other setpoints. Meanwhile, the setpoint changing rates are limited to avoid operational or computational difficulties.

Moreover, a set of testing data for verification purpose is generated with the inputs shown in Figure 5-6. The testing data also covers the status from full load to half load, but the patterns are different from the training data. Both the training data and the testing data are generated in Simulink 6.5 with the proposed mathematical model.

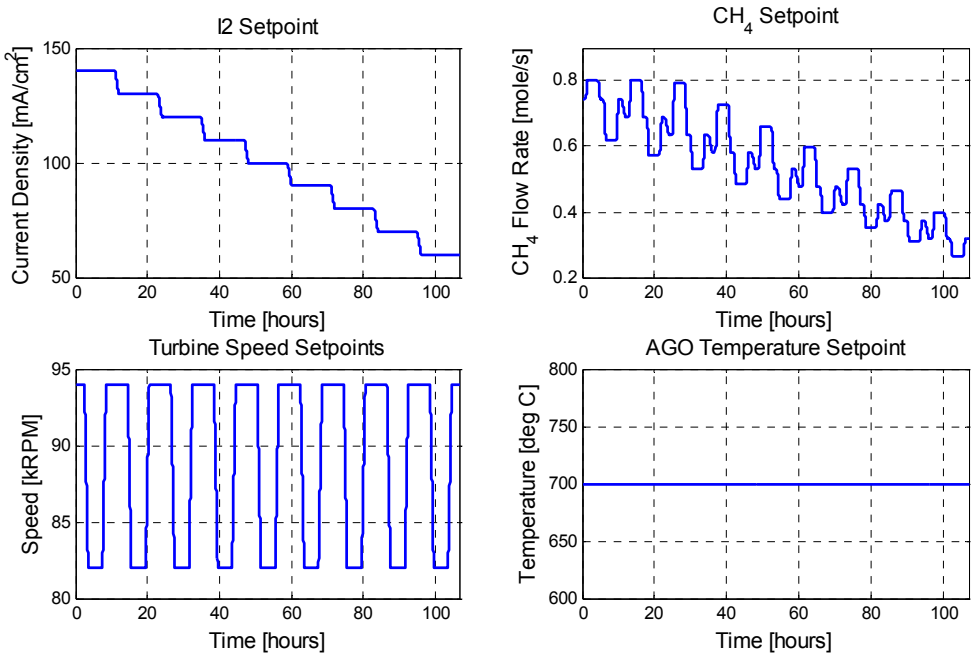

Figure 5-5 Setpoints in the simulation to generate the NN training data.

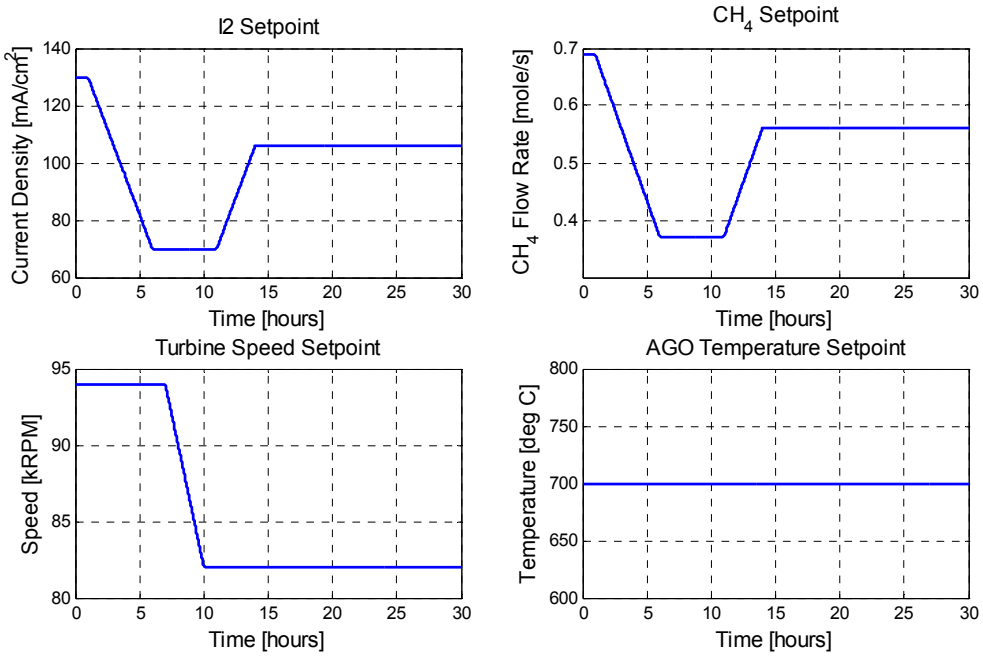

Figure 5-6 Setpoints in the simulation to generate the NN testing data.

5.2.3 Neural networks design and training

Neural network models are built for the 7 subsystems defined in Section 5.2.1. Since most subsystems are static heat exchangers, the feedforward neural networks (FNN) are used for these subsystems, except for the fuel-cell stack, AGO, and gas turbine, which contain dynamic behaviors and need diagonal recurrent neural networks (DRNN) [47, 49]. The FNN realizes a static mapping with a simple structure, which is capable of modeling static systems, but it cannot represent a dynamic response in the time domain. Nevertheless, the DRNN can naturally represent dynamic systems and needs fewer weights and neurons than the fully-connected recurrent neural network (FRNN). Hence, the static subsystems are modeled with FNN, while the dynamic subsystems are modeled with DRNN. With this assignment, the state estimator can both preserve the dynamic characteristics of the system, and can keep a low complexity.

The neural network applied here has a simple structure of two layers: a hidden layer and an output layer. The input/output specifications of a neural network are the same as the corresponding subsystem. The numbers of hidden neurons are assigned to twice of the number of inputs plus one. In order to guarantee the modeling accuracy, some subsystems have slightly higher numbers of hidden neurons. The neural networks are trained by the backpropagation method with the Levenberg-Marquardt algorithm [51, 52], which needs fewer training iterations and less time of convergence. The parameters of the neural networks and the training/testing results are listed in Table 5-1, where it can be seen that the neural networks models can estimates the outputs of the power plant accurately with the designed structure, training data, and training algorithm.

Table 5-1 Parameters and performance of the neural network models.

Subsystem	# of inputs	# of outputs	# of hidden neurons	Training Epochs	MSE training	MSE Testing
HH	7	2	15	55	1.1×10^{-4}	1.6×10^{-4}
LTR+SSH	9	2	24	60	4.6×10^{-3}	2.0×10^{-3}
FP+PC+SP	8	6	17	11	8.7×10^{-3}	4.5×10^{-3}
Stack	11	12	25	30	5.8×10^{-4}	1.6×10^{-3}
Turbine	7	6	18	45	7.8×10^{-3}	1.4×10^{-3}
HTR	7	2	15	35	8.9×10^{-4}	7.5×10^{-4}
AGO	7	5	15	28	2.4×10^{-4}	1.6×10^{-4}

5.2.4 The neural network combined model (NNCM)

Once the NN models for each subsystem are successfully trained, they will be combined to compose a NN-based combined model (NNCM) [49]. In the NNCM, the individual NN models are connected in series, in parallel, or in loops. The outputs of a specific NN model may be the inputs of other NN models, or be part of the outputs of the combined model. The 7 neural network models trained in the previous section are connected according to the input/output relationships in Figure 5-4, and then an overall plant model can be achieved. Because of the structure of the power plant, several subsystems are connected in loops, which will cause computational difficulties due to the algebraic loops formed by interconnecting the subsystems.

The algebraic loops

After the separate neural networks are joined into a combined model, six basic algebraic loops are developed as in Figure 5-7. An algebraic loop is a computational problem in simulation that the input of a system is determined by the output of itself. For instance, in the LOOP 2 of Figure 5-7, stream #3 and stream #4 are the input and output

of the "stack", respectively. Stream #3 is required to calculate the values of stream #4. On the other side of the loop, stream #3 and stream #4 are the output and input of the subsystem of "FP+PC+SP", respectively. Thus, to calculate stream #3, stream #4 is required. As a result, stream #4 is needed to calculate the values of itself. Thus, an algebraic loop is formed between the "stack" and the subsystem of "FP+PC+SP". Same logic exists in the other 5 algebraic loops.

These algebraic loops will create computational difficulties in simulation. First, the stream values are hard to determine because they are self-dependent. Second, the simulation errors will propagate and accumulate through the loops during simulation.

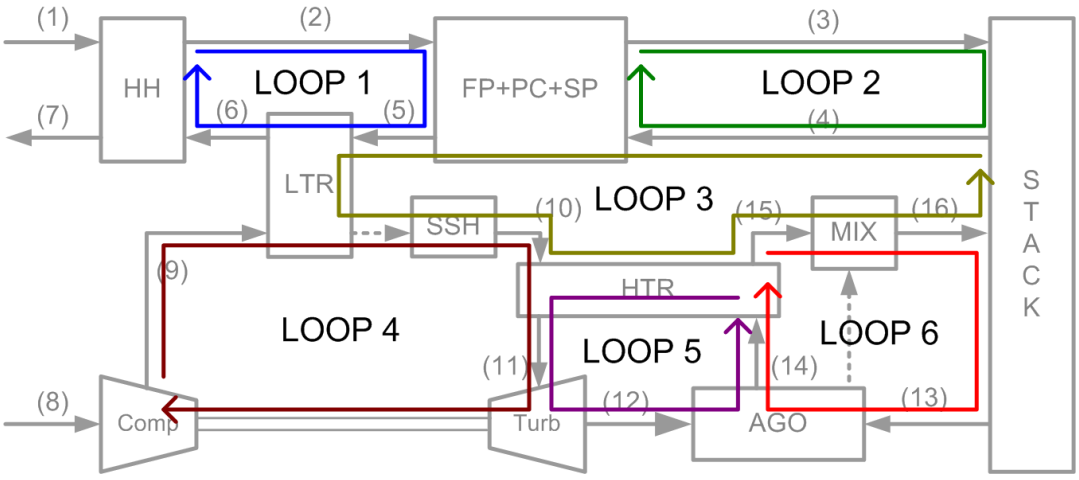

Figure 5-7 The algebraic loops of the neural network combined model.

The unit delays and NN starters

These algebraic loops must be eliminated to start the simulation. The normal technique is adding a small delay as a memory in the loop. Since the neural network models are discrete, unit delays (*i.e.*, Z^{1}) are added. These unit delays should remove all the loops from the system, and should be as few as possible to minimize the complexity

of the combined model. In addition, one algebraic loop should only contain one unit delay, otherwise convergence would be slow. One possible solution is shown in Figure 5-8, where 4 unit delays are applied to the combined model.

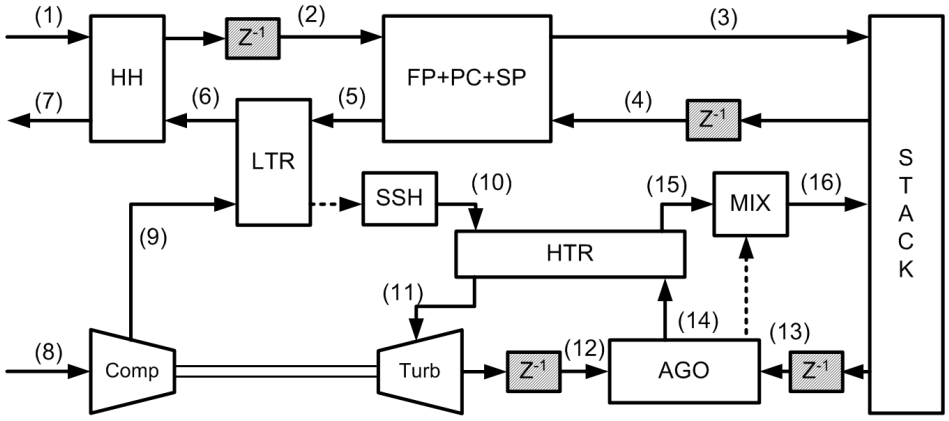

Figure 5-8 The block diagram of the NN combined model with unit delays.

The unit delay at stream #2 breaks LOOP 1; the unit delay at stream #4 breaks LOOP 2 and LOOP 3; the unit delay at stream #12 breaks LOOP 4 and LOOP 5; the unit delay at stream #13 breaks LOOP 6. With these 4 unit delays, the 6 algebraic loops can be eliminated, and the simulation can be started.

Moreover, the initial values for these delay units are also required to start the simulation. At the step of k=1, the outputs of the unit delays are needed, but are unknown in the combined model. To determine the initial values, two neural network starters are developed to estimate the initial conditions based on the given setpoints. One NN starter estimates the initial values of stream #4 and #13, which are the outputs of the fuel cell stack. The other NN starter initializes stream #2 and #12. With these unit delays and neural network starters, the simulation of the combined model can be started and processed successfully.

Error propagation

Although the NN combined model with unit delays and NN starters can be simulated smoothly, the simulation result may be invalid due to the algebraic loops, where the small errors of the single neural networks may propagate and accumulate to a significant error. To overcome this problem, all the sources of error need to be identified. Then, for each error source, the neural network needs to be re-constructed and retrained, until the closed-loop error reaches an acceptable level.

Simulation results

With the properly trained neural networks, the unit delays, and the neural network starters, the NNCM can estimate the outputs of the DFC/T power plant successfully and accurately. The simulation results of the NNCM with the training data and the testing data are shown in Figure 5-9 and Figure 5-10, respectively. For the training data, the simulation results of the NNCM are very close to the results of the original mathematical model. Based on the testing results, the NNCM can also approximate the outputs of the original model with acceptable errors.

Moreover, the inlet/outlet temperature of the electrodes, fuel cell DC power, and turbine AC power are selected and plotted in the figures, because these variables are important system states that can reflect the operating status of the whole power plant.

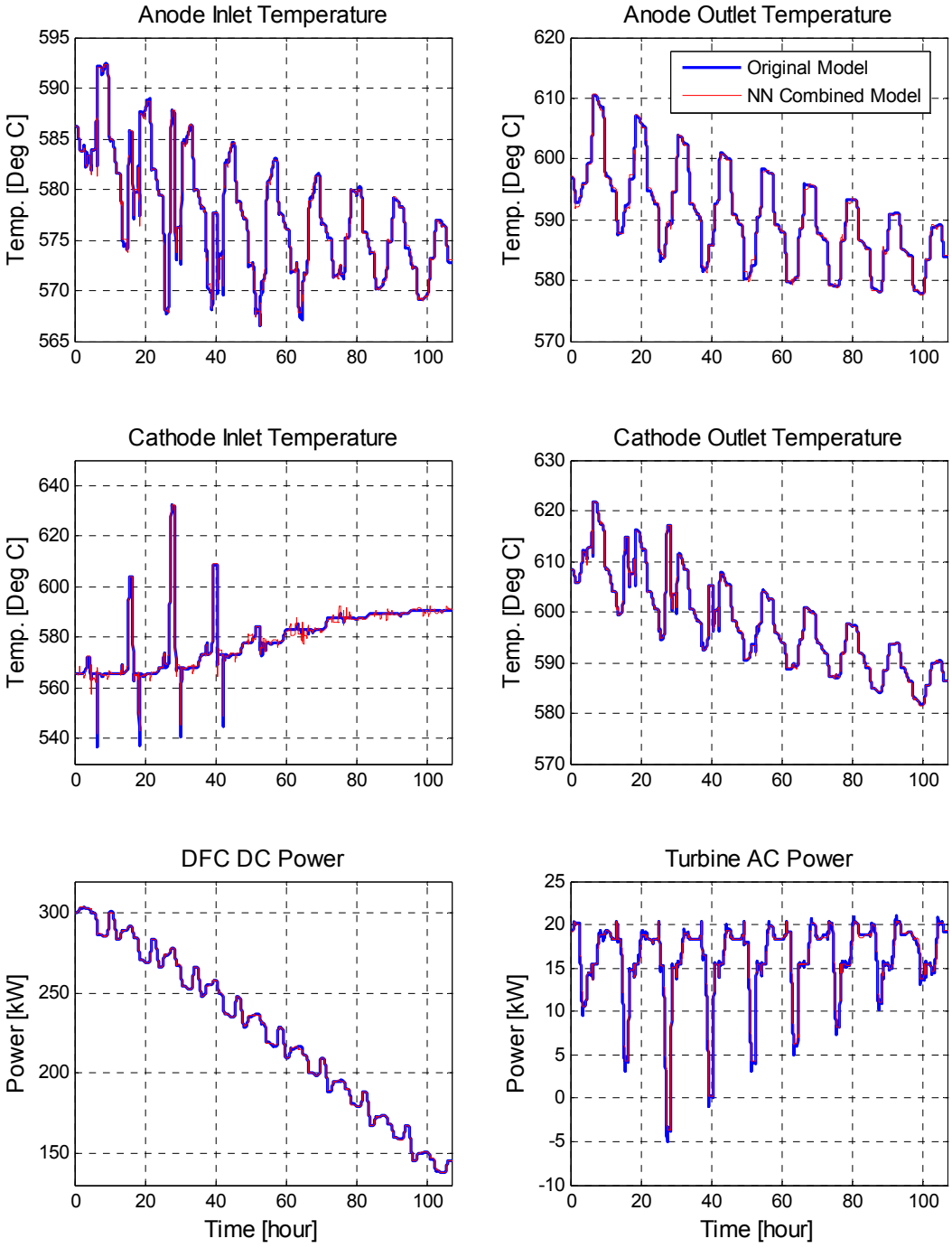

Figure 5-9 Simulation results of the NNCM on the training data set.

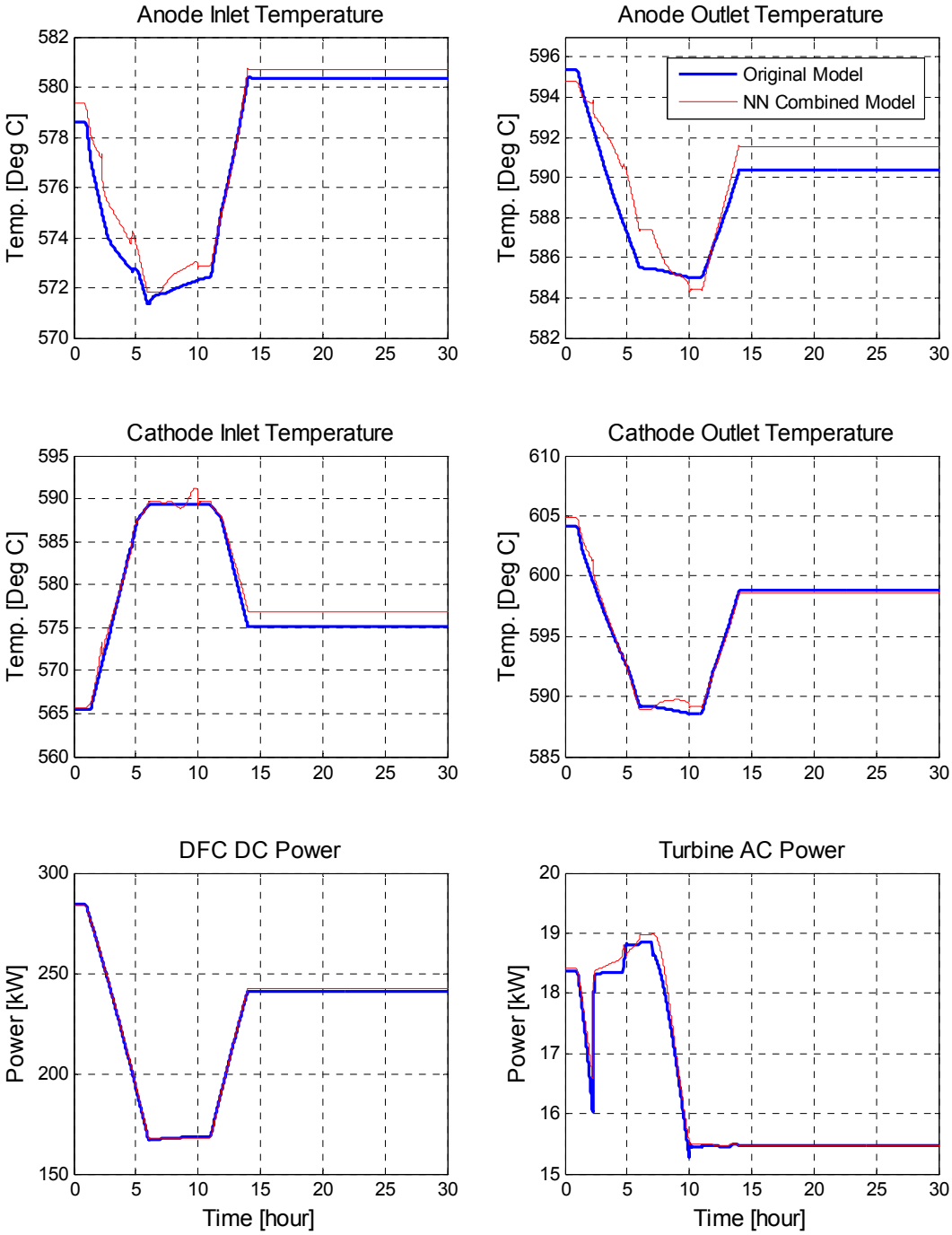

Figure 5-10 Simulation results of the NNCM on the testing data set.

Because the system modeling capability of a single neural network is limited, a combined neural network model is developed in this section to expand the capacities of single neural networks. Algebraic loops are formed in the combined model and are solved by the unit delays and neural network starters. The NNCM can estimate the outputs of the DCF/T power plant with low complexity and high accuracy. The validity of the NNCM is verified by comparing the NNCM simulation with the result of the original model.

5.3 The Operating Windows

Given a certain power load demand, there are many combinations of setpoints that can satisfy the power demand, but each setpoint should be bounded in a particular range, which is called an operating window. The operating windows for these setpoints need to be determined as the solution space for the MOM. Operating windows are physically realizable operating ranges, constrained by physical limitations such as actuator limits, power limits, temperature limits, etc. Some limitations are easy to determine, such as the split ratios of control valves and the maximum power of electric heaters, but others need to be found from the plant operational data.

The training data generated in Section 5.2.2 is used to find the appropriate operating windows. In Figure 5-11, the simulation data is sorted and plotted in grey against the net output power. The special patterns in the simulation data are caused by the pre-defined input for the simulation. It can be seen that, for a particular output power, all setpoints are bounded in certain ranges and the envelops of the operational data are selected as the operating windows, which define the search space for the MOM.

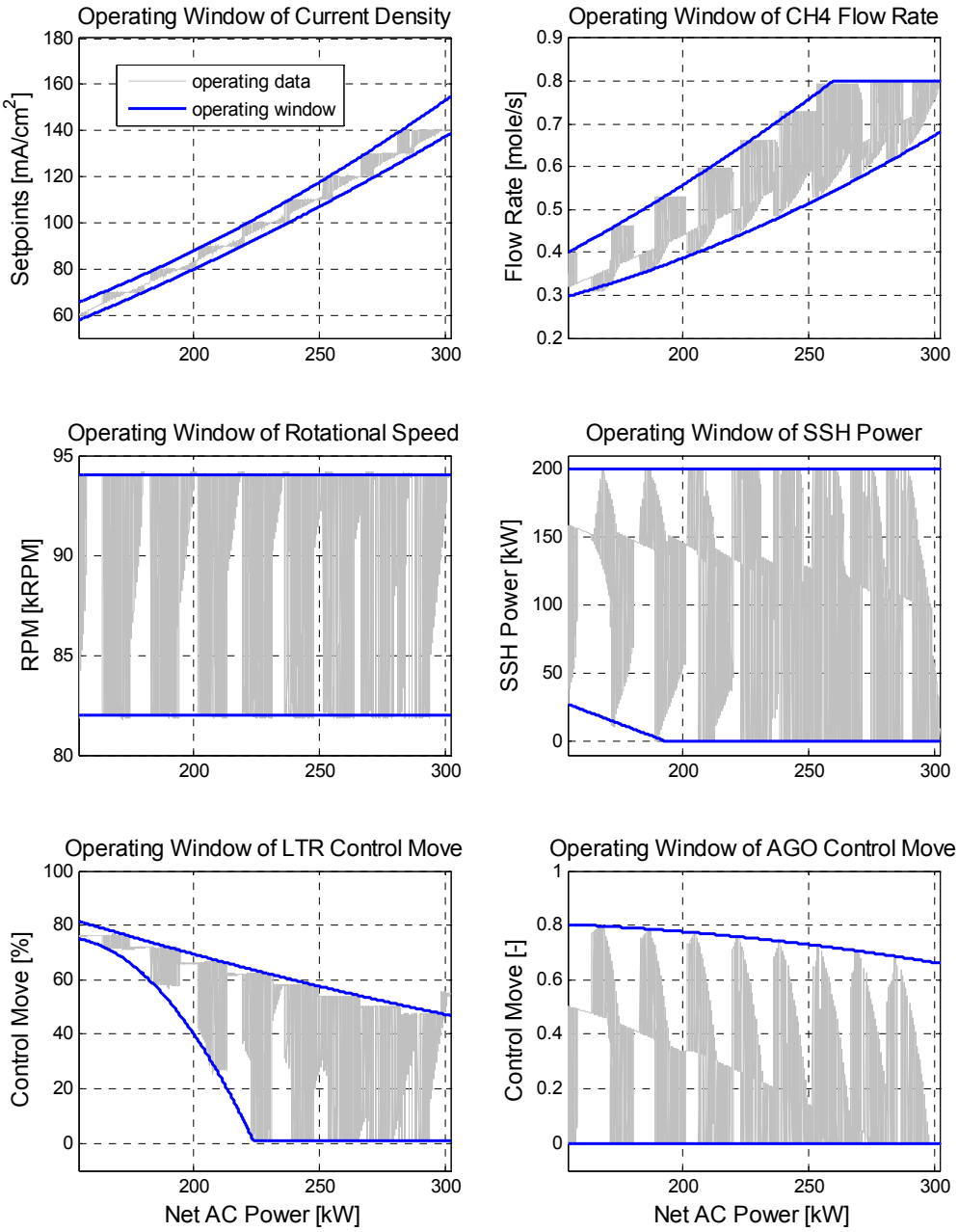

Figure 5-11 The operating windows of the Optimal Reference Governor.

5.4 Problem Formulation

The problem of the optimal control for the DFC/T power plant can be formulated with a multi-objective nonlinear optimization problem, which can be solved by the optimization algorithms discussed in Chapter 4. The problem is described as:

Find the 6 setpoints: the stack current density (I^2), methane flow rate (n_CH_4), turbine speed (RPM), power of the second-startup heater (q_SSH), LTR control move (u_LTR), and AGO control move (u_AGO), that minimize the 3 objective functions:

$$\min\{F_1,\ F_2,\ F_3\} \tag{5.1}$$

where

$$F_1 = \sum_{i=1}^{N}\left(P_{load} - P_{net}\right)^2 \tag{5.2}$$

$$F_2 = \sum_{i=1}^{N}\left(TCI_{set} - TCI_{act}\right)^2 \tag{5.3}$$

$$F_3 = \sum_{i=1}^{N}\frac{P_{csm}}{P_{net}} \tag{5.4}$$

The first objective function is defined on the power load, where P_{load} is the power load demand, and P_{net} is the net out power of the power plant. This objective function forces the generated power to follow the demanded power. The second objective function is defined on the cathode inlet temperature, an important control variable for plant operation to maintain the temperature of the fuel-cell stack. The cathode inlet temperature setpoint, TCI_{set}, is determined by the current density according to the manufacturer's requirement, while TCI_{act} is the actual cathode inlet temperature. The third objective

function is defined on efficiency, where P_{csm} is the total consumed power by the power plant, including the chemical potential contained in the fuels and the power used by the electrical heater. Minimizing this objective function will maximize the plant efficiency.

The constrains of the optimization problem is described in (5.5), where X can be any one of the 6 setpoints. Each setpoint searched by the MOM must belong to its operating window given in Figure 5-11.

$$\text{Setpoint}(X) \in \text{Operating Window}(X) \tag{5.5}$$

Moreover, the variables used in the objective functions are estimated by the NN combined model in Section 5.2.4. The NNCM can be represented as a nonlinear function (5.6) that maps the 6 setpoints to the plant outputs or states of interest. In the optimization problem, the stack DC power (P_{DFC}), turbine AC power (P_{Turb}), and cathode inlet temperature (TCI_{act}) are selected as the outputs of the NNCM. The objective functions will be calculated from the 3 system outputs and the 6 given setpoints.

$$[P_{DFC} \quad P_{Turb} \quad TCI_{act}] = f_{NNCM}\left(I^2,\ n\_CH_4,\ RPM,\ q\_SSH,\ u\_LTR,\ u\_AGO\right) \tag{5.6}$$

5.5 Optimization Results

A variety of advanced heuristic optimization algorithms introduced in Chapter 4 are implemented in the MOM for the ORG. The MOPSO algorithm with the Pareto dominance approach is firstly investigated with the NNCM and the operating windows to perform the tasks of the ORG. For a given power load demand, a set of optimal candidates will be provided.

Figure 5-12 is an example of the Pareto frontier obtained by the ORG under the power load of 250kW. Twelve candidate particles were collected during the MOPSO search process. Since each particle has three criteria, the candidates can be plotted in a 3-D space as the lower right chart in Figure 5-12. The projections of these particles on 2-D planes (*i.e.*, F_1 - F_2 plane, $F_1 - F_3$ plane, and $F_2 - F_3$ plane), are plotted in the upper left, upper right, and lower left quarters, respectively. Here, since the Pareto frontier is a surface in a 3-D space, its projections on any 2-D planes may not shape as a 2-D Pareto frontier. For convenience, each particle is associated with a distinct grey scale, so that it can be easily identified from the 3-D plot and its projections. Each particle in Figure 5-12 provides a pair of setpoints for the optimal control of the power plant. Different particles take different weights on different objectives. Thus, the final optimal control policy can be selected from them according to specific operating requirements.

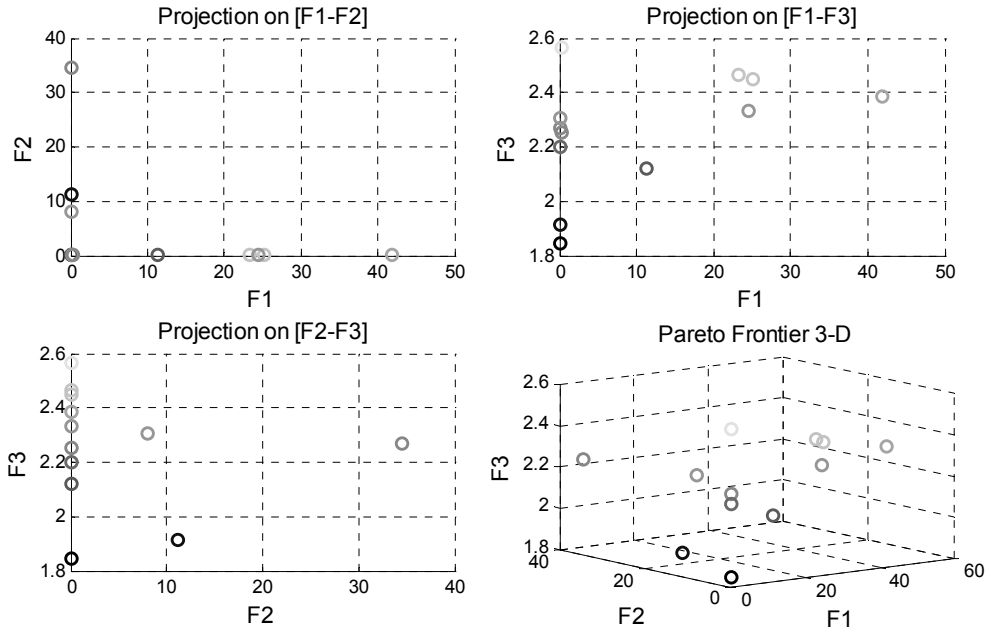

Figure 5-12 An example of the Pareto Frontier and its projections by the MOPSO.

5.5.1 ORG result before model updating

To select the "best" optimal solution, constant weights are assigned to the three objective functions as the weighted aggregation approach:

$$F = 0.4F_1 + 0.4F_2 + 0.2F_3 \tag{5.7}$$

The power load tracking (F_1) and cathode inlet temperature tracking (F_2) take more weight than the fuel efficiency (F_3), so that the power and temperature tracking will have higher priority than the efficiency.

The optimal control setpoints are generated by the ORG in Figure 5-13 for the power loads from 150kW to 300kW with 5kW increments. The sample points are marked with asterisk. The current density and methane flow rate increase monotonically with the power demand. Irregular variations can be observed in the turbine speed, while the LTR control move keeps constant for most instances. The SSH power and AGO control move have different patterns below 170kW compared with the result under higher power loads.

To verify the optimization results of the ORG and the validity of the NNCM, the optimal setpoints in Figure 5-13 are applied both to the NNCM and the original mathematical model. The two sets of simulation results are compared in Figure 5-14. The estimated outputs of the NNCM indicate ideal operational conditions and high fuel efficiency. However, it can be seen from the comparison that the NNCM has significant errors in turbine AC power when the power load runs below 170kW. The original model gives negative turbine power, but the estimated power is positive. As a consequence, the net output power and the plant efficiency of the NNCM also differ from the mathematical model. Meanwhile, considerable errors can be found in the anode inlet temperature and

the cathode inlet temperature. The deviations between the NNCM and the original model are caused by the new operational patterns, which have never been learned by the neural network models. Therefore, the NNCM needs to be updated with the new operating data.

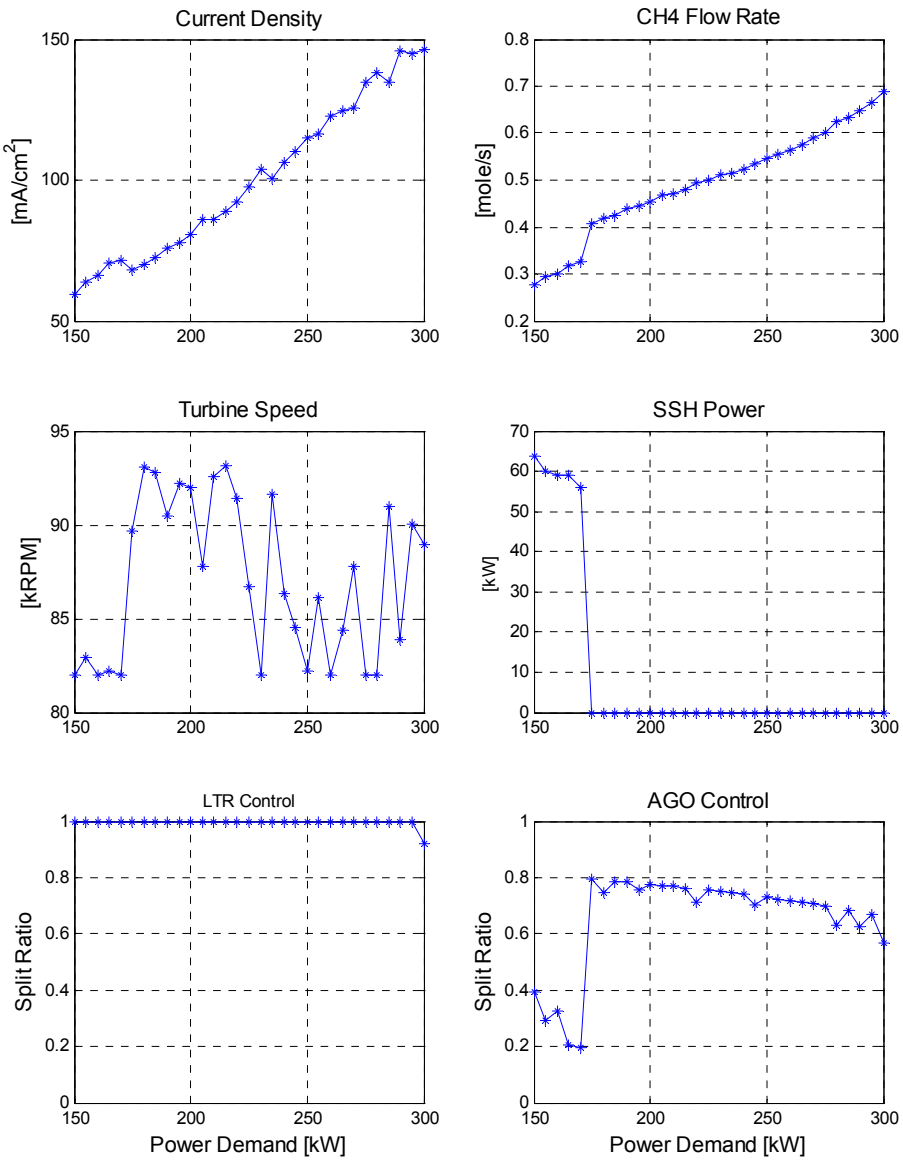

Figure 5-13 Optimal setpoints obtained by the PSO-based ORG.

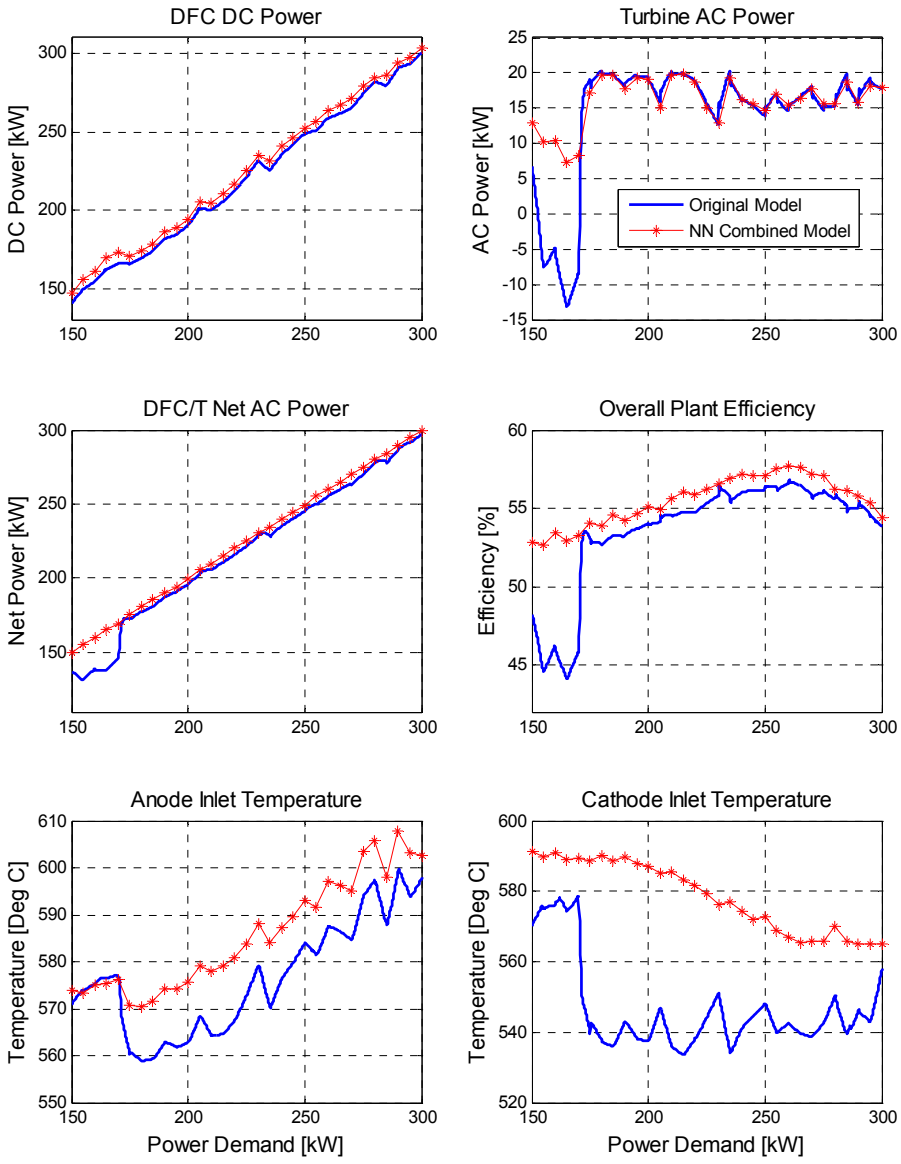

Figure 5-14 The simulation results of NNCM versus the original plant model.

5.5.2 ORG result after model updating

Once, the errors between the NNCM and the actual plant are identified, the ORG will enter the model updating mode as shown by the dotted line in Figure 5-1, where the actual power plant is replaced by the mathematical model in this study due to the limitation of the experimental data. With the new operational data, the neural networks of the NNCM are retrained and tested with the given setpoints. The results are presented in Figure 5-15. The estimation errors of the updated NNCM are considerably reduced and become acceptable for the ORG framework. However, based on the current optimal setpoints, the output power cannot follow the power demand below 170kW. The cathode inlet temperature cannot be controlled according to the specifications, and the fuel efficiency below 170kW is considerably low. Hence, the optimal solution of the ORG expires after the estimator is updated. The searching process should be executed again to update the optimization results.

The new solution of the optimization problem is shown in Figure 5-16. The current density and methane flow rate increase monotonically with the power load. The turbine speed keeps at the lowest speed to introduce less cold air to the system. The SSH power decreases and stays at zero when the power load reaches a certain level. The LTR control stays at the highest value to maximize heat recuperation. The AGO control goes around zero to transfer more heat to the turbine, and increases at high power load to maintain the cathode inlet temperature.

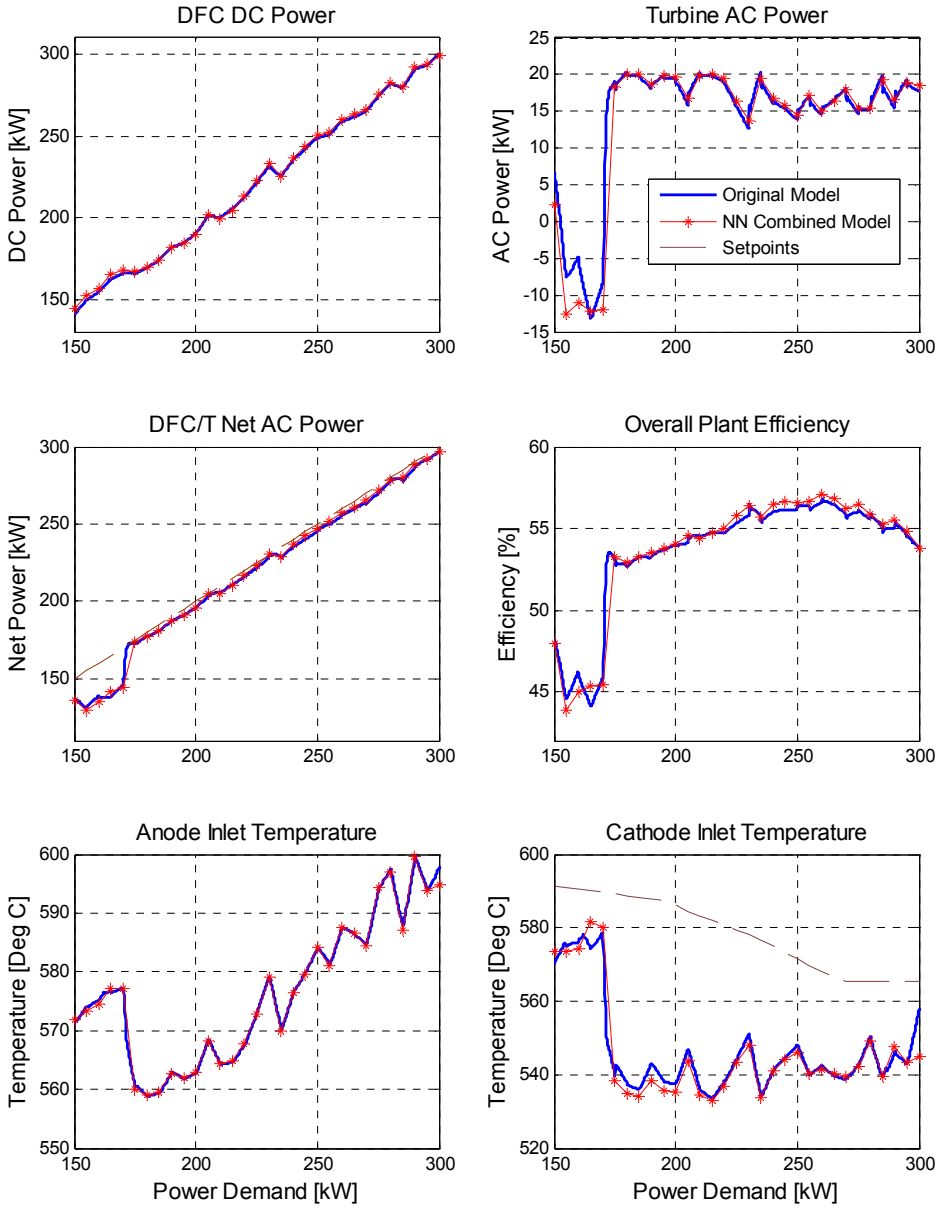

Figure 5-15 The outputs of the updated NNCM compared with the original model.

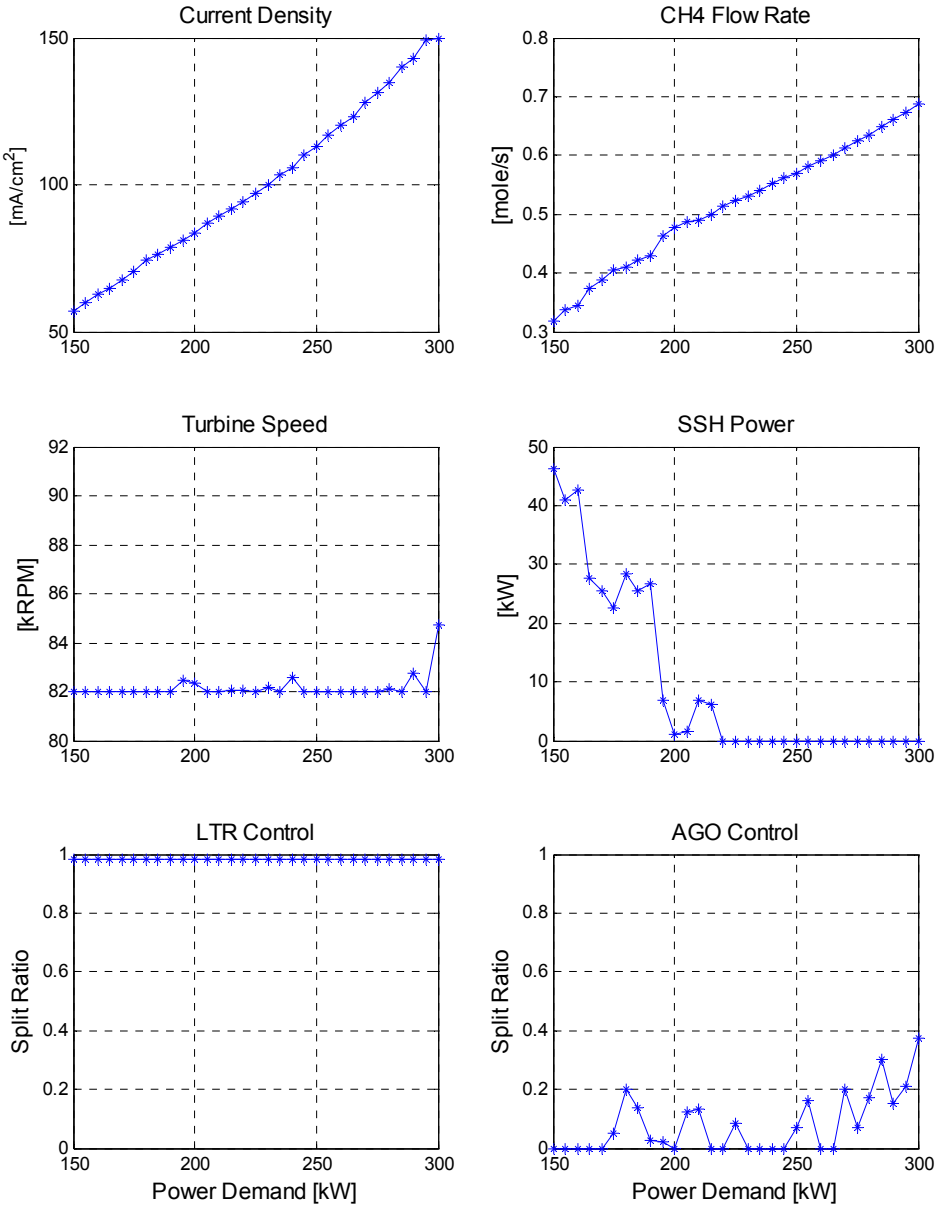

Figure 5-16 Optimal setpoints generated by the ORG with updated NN estimator.

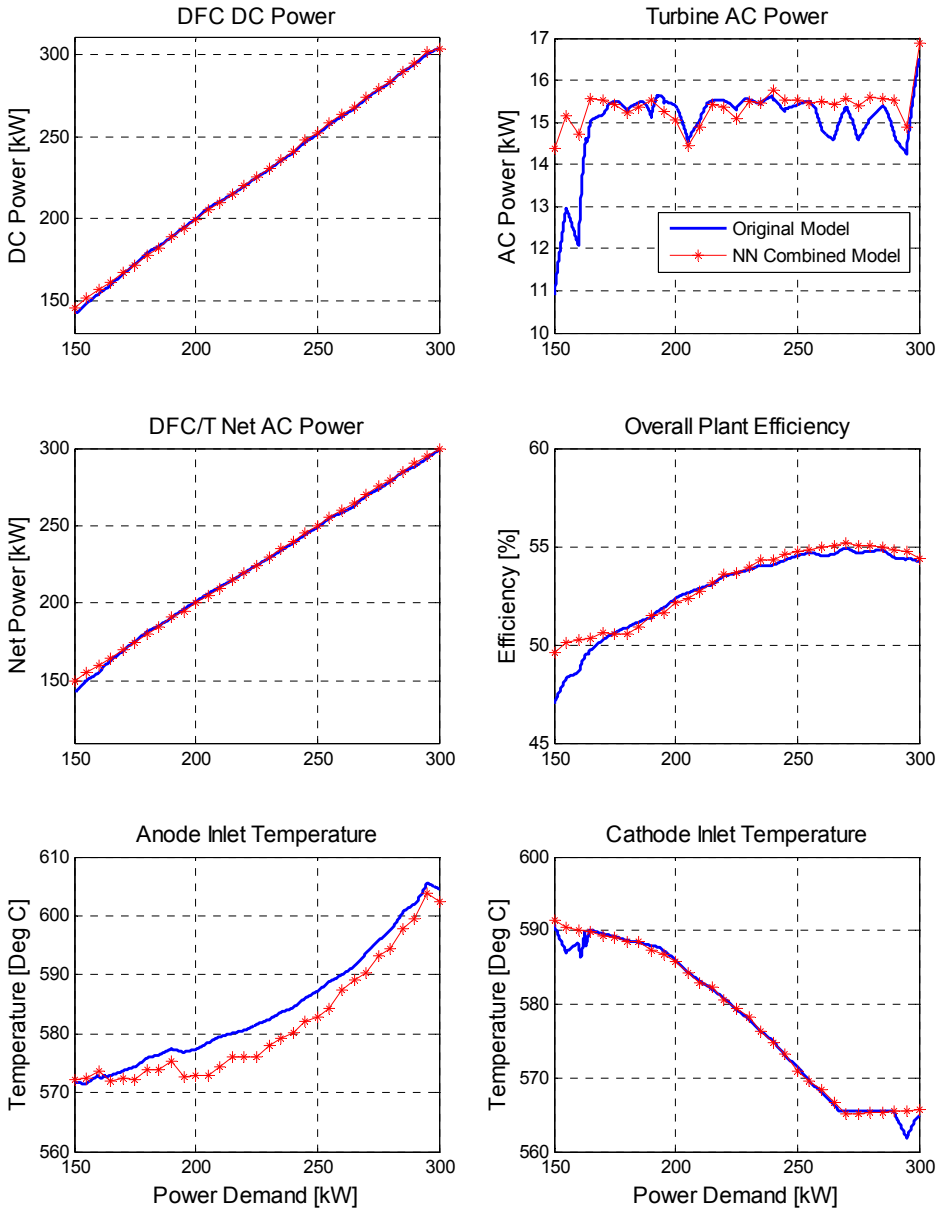

Figure 5-17 The simulation results with the updated optimal setpoints.

The simulation results with the updated optimal setpoints are shown and compared in Figure 5-17. The net output power generated by the DFC/T power can follow the power demand well, and the cathode inlet temperature is correctly controlled according to the temperature setpoint. Based on the simulation result, the DFC/T efficiency is rising with the power load, until it reaches the maximum efficiency of 55% at 270kW. Then, the efficiency slightly drops if the power goes higher. The optimized efficiency is compared with the actual operating data in Figure 5-18, where the experiment was conducted without the ORG and is plotted in dashed line. It can be seen that the simulation result with the optimized setpoints and feedforward controls shows higher fuel efficiency than the operation data without the ORG. Thus, the optimization results provided by the ORG are valid for the optimal operations of the DFC/T to improve fuel efficiency.

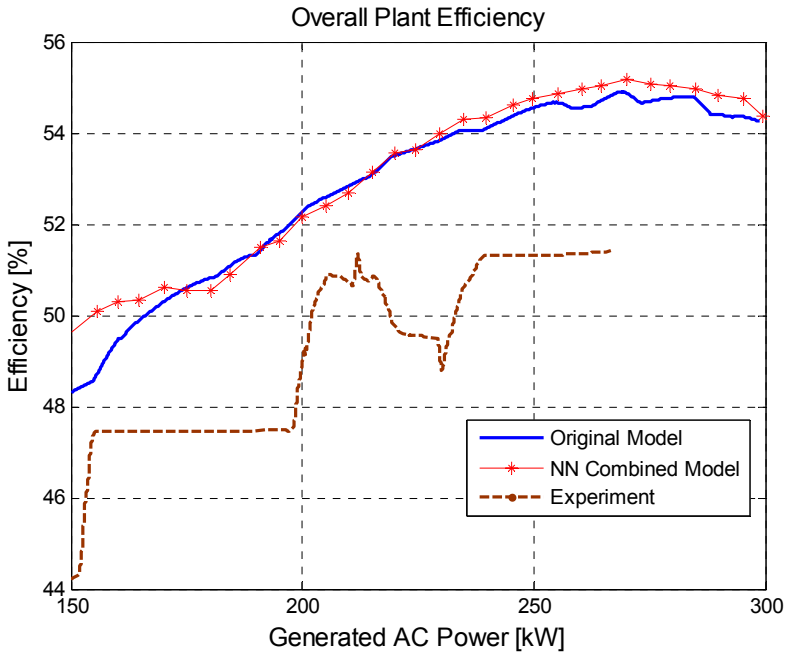

Figure 5-18 Overall plant efficiency of simulation and experiment.

Chapter 6

Fault Diagnosis and Accommodation and the Integrated Intelligent Control System

With the augmented mathematical model and the optimal reference governor, the plant control system can maintain good performance during normal operations. However, this alone is not sufficient for an intelligent control system with advanced technologies. Since local controllers have only limited information regarding the entire plant, incorrect control behaviors may be taken due to system failures. These abnormalities may consequently trigger performance degradation or even instability. Therefore, when fault occurs, the control system should detect the fault at an early stage and take appropriate reactions to avoid damages or degradations. As a part of the intelligent control scheme, a fault diagnosis and accommodation (FDA) system is introduced and the integrated intelligent control system is presented with simulations for various possible scenarios.

6.1 Fuzzy Fault Diagnosis

6.1.1 Definition of fuzzy faults

Power plant faults can occur anywhere in the plant at any time. However, it is impossible and unnecessary for a control system to identify the exact locations of all minor faults. On the other hand, the ability of locating faults at a subunit level is sufficient for control system design. Meanwhile, temperature control scheme is more

complicated and important than other control schemes, because the temperature exchangers and controllers are the major balance-of-plant equipments that determine the energy distribution of the entire system and guarantee smooth and reliable operations. The DFC/T power plant is operating under constant pressures and only two pressure controllers exist in the system. The fuel mass flow rate does not change along pipes or heat exchangers. Thus, the fault in pressure or mass/mole flow can be easily determined directly from the measurement data. However, the temperatures are highly coupled throughout the system and make the temperature faults not easy to diagnosis and isolate. In this chapter, only six fault patterns are defined on temperature control failures at the six major heat exchangers in the fault diagnosis system. These fault patterns are:

- Humidifier/Heat exchanger (HH) fault
- Fuel Pre-Heater (FP) fault
- Low Temperature Recuperator (LTR) fault
- High Temperature Recuperator (HTR) fault
- Anode Gas Oxidizer (AGO) fault
- Second Start-up Heater (SSH) fault

To provide more information about the temperature failures, two fault styles are defined for each fault pattern according to fault symptoms:

- The first style is "P-fault", which represents the case that actual output temperature of a subunit is higher than expected. This is usually caused by the failure of the control valve, such that heat will be fully exchanged between two streams without control.

- In contrast, the second style is "N-fault", which represents the case that actual output temperature of a subunit is lower than expected. This is usually caused by the fault position of the control valve, such that heat cannot be transferred between two streams.

Although these fault styles are described by the faulty positions of control valves, they can also represent a series of faults having similar symptoms, such as failures in sensors, actuators, and other parts of control loops or gas flows. Even though some subunits such as HH and HTR are not controlled, faults with similar symptoms may be caused by other reasons, such as fouling, eroding, or electrical problems. Thus, the defined fault styles are also applicable for temperature faults in these subunits. Once the fault pattern and style are determined by the fault diagnosis system, human operators will use this information to identify the detailed reason for the fault.

6.1.2 Diagnosis algorithm

Extensive research and investigations on FDA algorithms have been done in recent decades by researchers [53-64]. Instead of *hardware redundancy*, where redundant physical subsystems are constructed, most of the current research in FDA is based on *analytical redundancy*, in which sensory measurements are processed analytically to compute the value of a desired variable. Using this method, Polycarpou and Helmicki [55] and Farrel *et al.* [56] provided a framework of the FDA architecture and a general learning methodology for detecting and regulating system failures. Meanwhile, intelligent control theories are found to be powerful tools in FDA in recent years. These intelligent

approaches mainly include neural networks [57, 58], fuzzy systems [59, 60], and neuro-fuzzy systems [61]. However, most of these approaches assume that the system, either linear or nonlinear, is fully measurable or observable, which is not always true in real engineering problems, especially for large-scale complex plants such as the DFC/T plant.

The fault diagnosis algorithm usually includes two steps: residual generation and decision making [53, 58, 62]. The analytical redundancy method generates residuals by comparing the outputs of a plant with a mathematical model, either analytical or numerical [53]. In this work, the augmented hybrid model of the DFC/T in Chapter 2 is applied as a reference of normal operations without any fault. The outputs of the power plant (power, temperature, pressure, *etc.*) are compared with the estimated outputs of the model. The diversities between the plant and model serve as the residuals used for decision making.

Since the DFC/T power plant is highly coupled and complex, the model outputs for each subunit are estimated separately. For the *i*-th subunit, the output y_i is a function of the states x_i, the inputs y_k of this subunit (or the outputs of the subunits connected to it), and the control input u_i, as shown in (6.1). Meanwhile, the estimated output $\tilde{y}_i$ of the *i*-th subunit is a function of the estimated states $\tilde{x}_i$, and the inputs y_k and u_i of the actual subunit, as shown in (6.2). The dynamic equations are defined in the plant model [8, 12] and have the same initial conditions as in the real plant. The residual is thus calculated by (6.3) as following:

$$y_i = f\left(x_i, y_k, u_i\right) \tag{6.1}$$

$$\tilde{y}_i = \tilde{f}\left(\tilde{x}_i, y_k, u_i\right) \tag{6.2}$$

$$res_i = y_i - \tilde{y}_i \tag{6.3}$$

When the plant is devoid of faults, the residuals of all subunits will be small. However, if a fault occurs in the plant, the residuals for one or several subunits will be noticeable and detectable.

A number of decision making methodologies have been investigated [55-61]. In this work, fuzzy logic is used to determine fault conditions, because fuzzy theory is an effective tool in processing the ambiguous relationships of fuzzy faults due to the limited information of the system. The structure of the fault diagnosis system is shown in Figure 6-1. While the residual only reflects the state of the plant at a particular time instant, its integral contains much more information about the time history [65] of the plant status, which is more important for fault diagnosis than only the residual. For instance, small and persistent residuals will be accumulated by integration and become noticeable. In contrast, a brief disturbance may have a much smaller weight in decision making. Therefore, the integral of the residual between the actual plant and the nominal model is assigned as the *primary* input of the FDA system.

Moreover, the integrals cannot provide sufficient information about faults, since either a large residual or a small residual can be accumulated to the same integral values as time elapses. However, the causes of the residuals may be completely different. The small residual could be caused by the inaccuracy of the model but not the system fault, and false alarm might be trigged if monitoring only the integrals. Hence the values of residuals for each subunit are used by the diagnosis system as the *secondary* input variable in determining the causes for the disturbances.

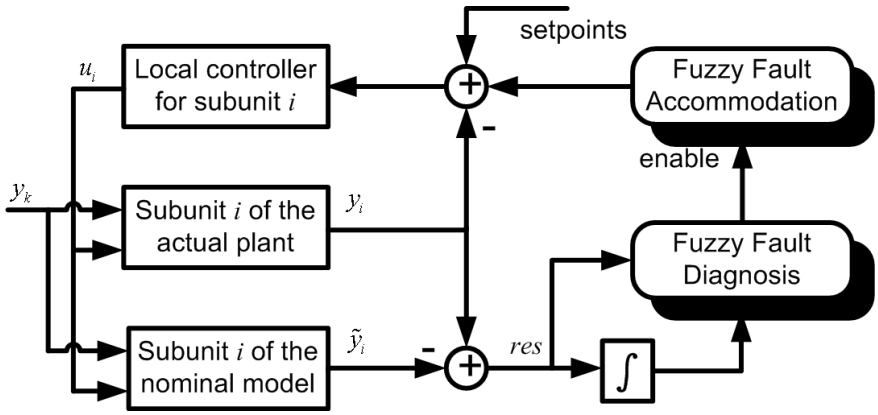

Figure 6-1 Block diagram of the fault diagnosis system.

6.1.3 Selection of variables

According to the algorithm indicated in Figure 6-1, the variable y_i and the corresponding estimated variable $\tilde{y}_i$ should be selected from all process variables for each subunit, on which the fault patterns are defined. The variables need to possess the ability of presenting the fundamental operational status of the subunits, and must be easily measured or calculated from the actual plant so that the diagnosis can be made practical.

In this section, the diagnosis system will be focused on the failures of temperature control, where the fault patterns are defined on heaters or heat exchangers. The energy increment of the stream from inlet to outlet at the cold side is a prime candidate that represents the amount of heat transferred by a heat exchanger and indicates the working status of the subunit. The energy increase can be calculated as follows:

$$y_i = \Delta E_i = N_i^{out} H_i^{out} - N_i^{in} H_i^{in} \tag{6.4}$$

$$H_i = \sum_{k=1}^{7} \tilde{x}_i^{(k)} \left(A_k T_i + B_k T_i^2 + C_k T_i^3 + D_k T_i^4 \right) \tag{6.5}$$

where $N_i^{out/in}$ and $H_i^{out/in}$ are the outlet/inlet mole flow rate and mole enthalpy of the *i*-th subunit, respectively. The mole flow rate can either be measured from the actual plant, or be estimated by the mathematical model. The mole enthalpy of the gas mixture can be obtained from (6.5), where $\tilde{x}_i^{(k)}$ is the mole fraction of the *k*-th component of the gas mixture, which is not measurable but can be approximated by the plant model; T_i is the measured temperature of a particular gas flow; A_k, B_k, C_k, and D_k are the coefficients obtained from the integration of the specific heat capacity of the *k*-th element of the gas mixture [8]. The reference variable $\Delta\tilde{E}_i$ is calculated similarly, but using the simulated variables from the model:

$$\tilde{y}_i = \Delta\tilde{E}_i = \tilde{N}_i^{out}\tilde{H}_i^{out} - \tilde{N}_i^{in}\tilde{H}_i^{in} \tag{6.6}$$

$$\tilde{H}_i = \sum_{k=1}^{7} \tilde{x}_i^{(k)} \left(A_k\tilde{T}_i + B_k\tilde{T}_i^2 + C_k\tilde{T}_i^3 + D_k\tilde{T}_i^4 \right) \tag{6.7}$$

Taking the HTR as an example, the variable ΔE_{HTR} is the energy transfer rate of the HTR based on measurements and represents its operational status. The reference $\Delta\tilde{E}_{HTR}$ is calculated from the mathematical model. The residual for HTR fault diagnosis is the difference between ΔE_{HTR} and $\Delta\tilde{E}_{HTR}$:

$$res_{HTR} = \Delta E_{HTR} - \Delta\tilde{E}_{HTR} \tag{6.8}$$

6.1.4 Membership functions and fuzzy rules

Three membership functions for fuzzy sets, *i.e.,* positive (P), negative (N), and zero (Z) in Figure 6-2, are defined for P-fault, N-fault, and fault-free status, respectively.

The likelihood of the existence of a fault is expressed by the membership values that it belongs to a particular fuzzy set. Due to the nature of faults and the limited information about failures, there does not exist clear boundaries distinguishing the different faulty situations. Thus, the overlapping membership functions are useful tools in expressing such fuzzy relationships. Meanwhile, the primary and secondary inputs are represented in terms of fuzzy logic by the membership functions in Figure 6-2. These functions map the normalized input variables to the membership values, which will be processed by fuzzy rules.

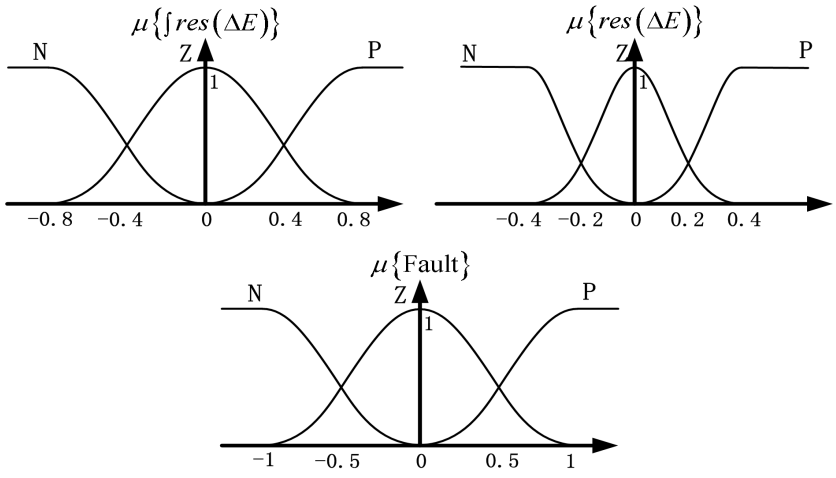

Figure 6-2 Fuzzy membership functions for HTR fault diagnosis.

After the inputs are converted into the membership values, the fuzzy rules will be launched to compute the likelihood of a fault belonging to different fuzzy sets. Three major rules are defined for each fault pattern as:

After the input variables are converted into degrees of truthfulness, the fuzzy rules will be launched to compute the truthfulness of a particular fault, which is the degree of

antecedent of the rules. Three common major rules are defined for each fault pattern. These rules are:

- If $\left\{\int res\left(\Delta E_i\right)\right\}$ is zero, then no fault exists.
- If $\left\{\int res\left(\Delta E_i\right)\right\}$ is positive and $\left\{res\left(\Delta E_i\right)\right\}$ is positive, then "P-fault" exists.
- If $\left\{\int res\left(\Delta E_i\right)\right\}$ is negative and $\left\{res\left(\Delta E_i\right)\right\}$ is negative, then "N-fault" exists.

Here, ΔE_i is the input variable for the *i*-th subunit and *res* indicates the residual of the variable. As in the first rule, if the integral is zero, non-fault situation can be determined based on the previous analysis. The second rule defines the condition for the "P-fault", where the temperature difference is significantly higher then expected. The third rule defines the condition for the "N-fault" that the temperature difference is negative, which indicates heat cannot be transferred through the heat exchanger.

Finally, for convenience, the membership values for each fuzzy set are defuzzified to a scalar value, likelihood index, indicating the likelihood of each fault style. A positive value indicates a "P-fault", while a negative value suggests an "N-fault". The higher the absolute value is, the more likely that the particular fault style happens. Thus, a 6×1 vector can be obtained as the diagnosis result, suggesting the existence of the six defined fault patterns.

6.2 Fuzzy Fault Accommodation

Detecting faults alone is not sufficient, though it is necessary for an intelligent control system. When a fault occurs, the plant needs to be regulated to prevent from

entering critical or even unstable operating regions before the fault is cleared or human takes over the control system. Due to the high complexity of the DFC/T power plant and the random nature of faults, it is difficult to design specific and detailed regulators to accommodate the system with very limited information on the causes and consequences of the faults. Nevertheless, fuzzy logic, as a qualitative scenario, is a powerful tool that has low complexity and less difficulty in designing the fault accommodation system.

6.2.1 Accommodation strategies

The core of the DFC/T power plant is the fuel-cell stack, where chemical potential is converted into electric power. Thus, maintaining the electrochemical reactions smooth and stable is the primary goal of the control system either under normal situations or during system failures. To achieve this goal, the temperature of the fuel-cell stack should be maintained within a certain range determined by the characteristics of the catalysts and the operating conditions. After the temperature is regulated, the power plant needs to track the power load demand assigned to it. Therefore, the objective of the accommodation system is to regulate the temperature of the fuel-cell stack and recover the output power during system failures.

Under normal operations, the stack temperature is dominated by the cathode inlet temperature T_{CI}, which is controlled by the LTR and SSH controllers on the basis of the setpoints T_{CISP}. The stack power is controlled by the methane flow rate N_{CH4} and the stack current density I^2. The unreacted methane is then burned in the AGO, and the excessive heat is used by the turbine to generate additional power [11, 12]. However, during system

failures, the temperature and power control scheme may become weak, not functional or even broken. On the other hand, from the viewpoint of the overall power plant, the stack temperature is determined by the energy contained in the methane flow that injected to the system. Meanwhile, the cold air takes heat off the plant and transfer the excessive heat to the gas turbine for power generation. Thus, even though the local control scheme may not be fully functional, the stack temperature still can be maintained by adjusting the amount of the fuel and the fresh air, and the output power can be regulated by adjusting the stack current density.

Therefore, the control strategies can be described as follows:

- If the stack temperature is *higher / lower* than normal, then *decrease / increase* the fuel flow rate N_{CH4} and introduce *more / less* air by *increasing / decreasing* the compressor speed R_{RPM};
- If the output power is *higher / lower* than demand, then *decrease / increase* the current density I^2 of the stack..

However, all strategies should be executed within the operating region of the DFC/T power plant. The ratios of fuel to current and fuel to air need to be maintained within a certain range to satisfy the requirement of chemical reactions; otherwise, the plant may become unstable or damaged. Moreover, the strategies are built based on an assumption that the DFC/T power plant is connected to a utility grid so that the power disturbance caused by faults and accommodating actions can be compensated.

6.2.2 Accommodation structure

According to the compensation strategies, the control scheme in Figure 6-3 is implemented in the FDA system. The input signals are the residuals of the two variables that need to be regulated, *i.e.,* the stack temperature T_{stk} and the net output power P_{net} of the plant. Both the residuals and their integrals are introduced to the fault accommodation controller for the same reason as in the diagnosis system. The outputs of the controller are setpoints modifications, which will compensate the original setpoints to take effect. The modified setpoints are restricted to the operational limitations to prevent instability and damages.

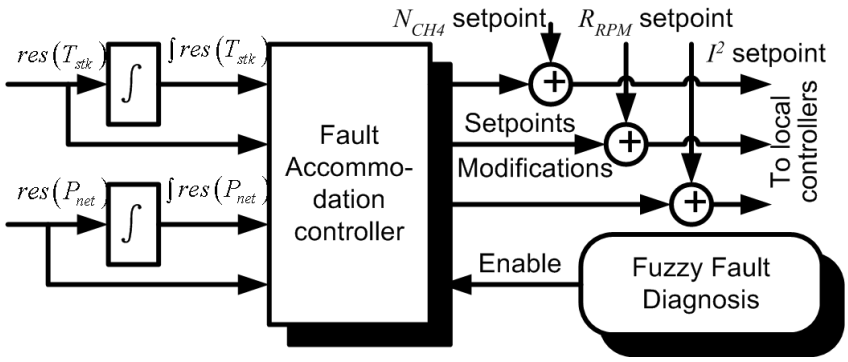

Figure 6-3 Block diagram of fuzzy fault accommodation system.

6.2.3 Controller design and tuning

Since the inputs of the fault regulator are the residuals (errors) and their integrals, it is a P-I type controller that can be tuned by a number of classic PID tuning methods [66, 67]. In this research, the membership functions of the fuzzy controller are triangle functions evenly placed in the interval of [-1 1]. To determine the gains of proportional and integral controls, the actual system is approximated as a first-order plus time delay

system, and the minimum ITSE (integral of time weighted square error) controller tuning rules [66] are applied to optimize the accommodation controller. Due to the random nature of faults, the dynamic of the post-failure system is hard to determine in real-time. Thus, the fault controller is tuned according to the average parameters of the normal system from half-load mode to full-load mode. For example, the step response of the stack temperature of the healthy system is plotted in Figure 6-4, where a step of the methane flow rate N_{CH4} at 0.05 mole/s is injected at t=0s. Because the DFC/T plant is a nonlinear system, the temperature responses are not identical under different load profiles. Hence, the average time delay, time constant, and gain are used for controller tuning.

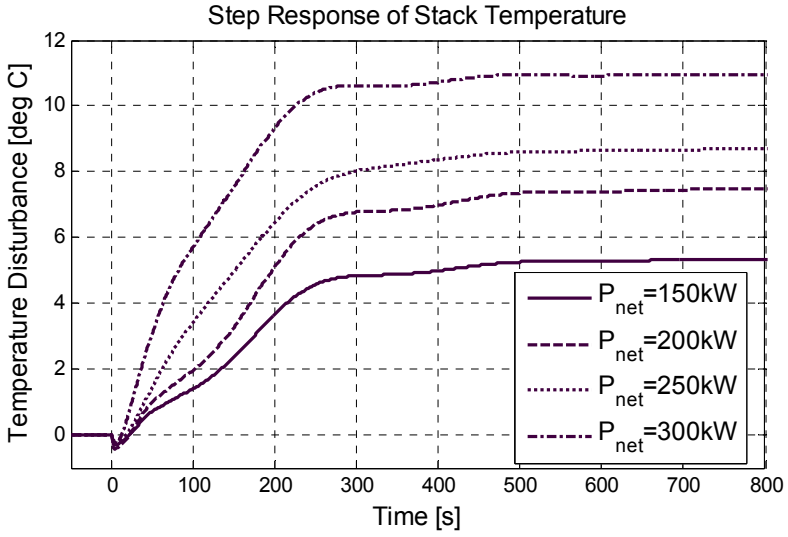

Figure 6-4 Temperature step response of stack under different power loads.

Although the fuzzy accommodation controller is tuned with the PID tuning method, it is different from the traditional PI controller. With the membership functions and fuzzy rules described in Section 6.2.1, the fuzzy logic is capable of realizing nonlinear relationship between the proportional and integral controls, rather than the

simple aggregation for PI controller. This nonlinear relationship may achieve faster response time and lower overshoot.

6.2.4 Fuzzy-neural networks

Another intelligent system approach for fault regulation is the fuzzy-neural networks, which possess the learning ability while regulating the system [61, 68]. The fuzzy-neural networks method is also investigated in this paper and compared with other approaches.

A classic structure of the five-layer neural network, as Figure 6-5, is used for fault accommodation. The first layer maps the inputs to the membership values for each fuzzy set by membership functions defined in the previous section. The second layer performs the fuzzy "and" operation with multiplication. The third layer is the normalization layer, which normalizes the weight of each rule by the sum of the weights of all rules. The forth layer is the consequent layer that calculates the implication from the decision w_i for each rule. The final layer is the aggregation layer, adding the implications of each rule to a scalar, which is the output of the fuzzy-neural controller [61]. In the training algorithm, the decision w_i (i=1,…,9) are the parameters need to be optimized. The objective function is defined on the ITSE index as:

$$E = \int_o^t \tau \left[res(T_{stk})^2 + res(P_{net})^2 \right] d\tau \tag{6.9}$$

The negative gradient direction is selected as the steepest descent direction for parameter updating [61].

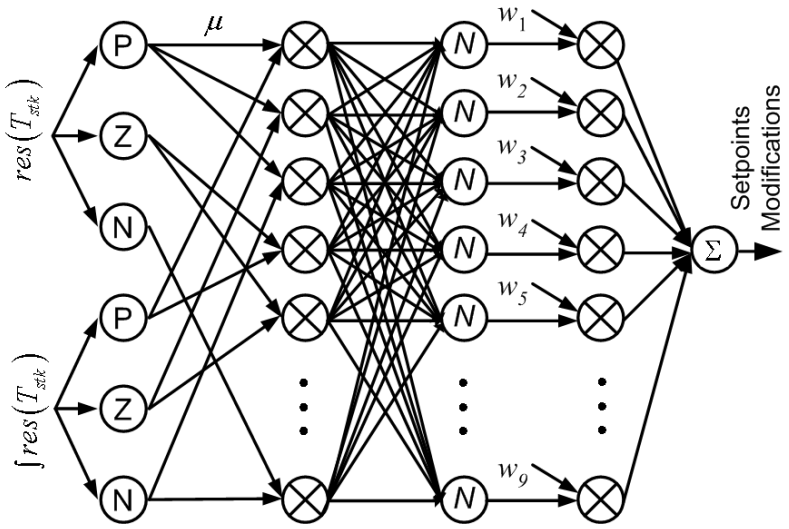

Figure 6-5 The structure of the fuzzy-neural network controller.

Because of the learning algorithm, the fuzzy-neural controller can update its parameters adaptively while regulating the system failures. This ability makes it a powerful fault regulation with better performance than the traditional PI controller and the fuzzy controller, which can be seen from the simulation results in the next section.

6.3 Integrated Intelligent Control System

6.3.1 Structure of the integrated system

The presented control systems not only can work individually, but also can be integrated as a comprehensive intelligent control system, where the individual systems collaborate with each other to perform overall management for the DFC/T power plant. The block diagram of the integrated control system is shown in Figure 6-6, where the

rounded blocks with shadows are the intelligent systems developed in this dissertation and the rectangle blocks come from previous work.

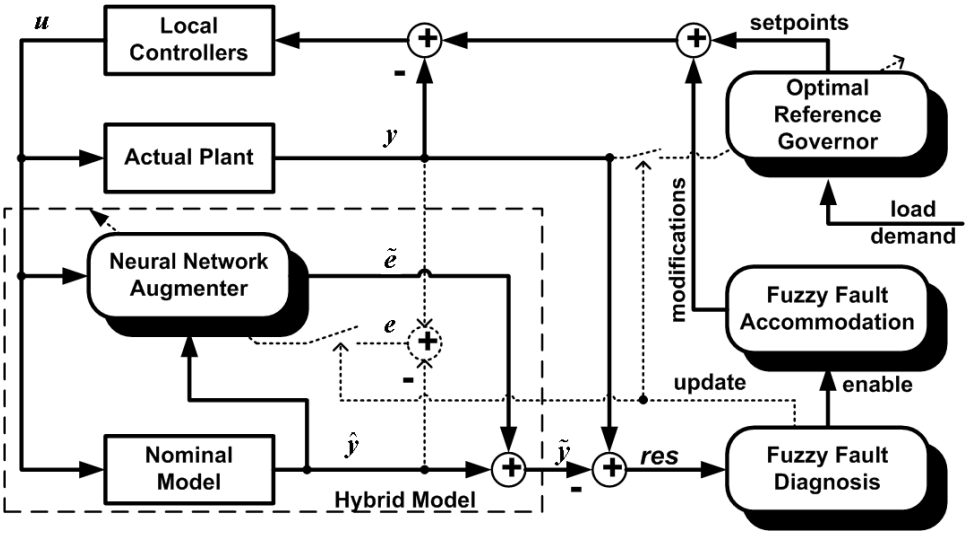

Figure 6-6 Block diagram of the integrated intelligent control system.

The hybrid plant model, which is achieved by the nominal mathematical model and the neural network augmenters, provides a reference of the normal operations for the FDA system. The fuzzy fault accommodation system will be activated by the diagnosis system and modifies the optimal setpoints generated by the optimal reference governor. The modified setpoints serve as the references for the local controllers of the power plant. The neural network models of the NN augmenter and the NN estimator in the ORG will be updated as suggested by the diagnosis system.

6.3.2 System behaviors during normal operations and fault conditions

During normal operations (*i.e.*, no fault presents in the system), the residual *res* between the power plant output y and the simulation result $\tilde{y}$ of the hybrid model are

sufficiently small that no fault signals are presented by the fault diagnosis system. Thus, the power plant will be supervised by the local controllers according to the setpoints provided by the optimal reference governor without modifications. Hence, the power plant can achieve high energy conversion efficiency.

On the other hand, if fault occurs in the system, the residual *res* will no longer be small. The fault diagnosis system will generate fault signals activating the fault accommodation system, which will modify the setpoints provided by the ORG and regulates the system during system failures. Although the modified setpoints may not be optimal in efficiency, they can keep the plant from critical operating regions and prevent damages or degradations. Thus, the plant reliability can be improved.

6.3.3 Model updating

An additional capability because of the integration of the control system is the model updating scheme plotted in the dotted lines in Figure 6-6. In case of a consistent and gradually increasing residual *res*, the fault diagnosis system will provide a model updating signal indicating the mathematical model is expired and needs to be updated. This situation usually happens when the power plant is operating under a new pattern that the neural networks have never learned or the parameters of the power plant keep changing slowly with time elapsing.

In the model updating phase, the neural networks are retrained with the newly collected operational data. The NN augmenters are trained with the error e between the plant output y and the model output $\hat{y}$, while the NN estimator of the ORG is trained

with the new operational data y. After the models are updated, the integrals in the FDA system will be reset to erase the memory of the previous operational information.

The integrated system in Figure 6-6 shows a comprehensive plant-wide control system, where the local controllers, optimizer, fault detector, and hybrid plant model are working in parallel and collaboratively. The integrated control system can operate the power plant with high fuel efficiency in normal operations, and can protect the plant from damages during system failures. Meanwhile, the model updating scheme guarantees the validity of the whole system in providing effective managements for the hybrid power plant. Hence, an intelligent autonomous control system is finally achieved to perform efficient and reliable control for the DFC/T power plant.

6.4 Simulation results

To evaluate the performance of the overall intelligent control scheme and different fault accommodation algorithms, an SSH-N fault and an LTR-P fault are simulated under power demands of 150kW and 300kW, respectively.

6.4.1 SSH-N fault at 150 kW

When running at 150kW, the plant cannot generate sufficient heat with a small amount of fuel. Thus, the SSH serves as an electric heater to provide additional heat to maintain the temperature of the fuel-cell stack. The turbine can not provide enough torque to drive the air compressor, so that the generator works as an electric motor to

provide additional torque. As a possible failure mode, an SSH-N fault is simulated at t = 0s, such that no additional heat is provided to the system.

Figure 6-7 shows the vector of the diagnosis result, where each element of the vector provides the likelihood index for the existence of each fault pattern. The solid lines indicate the result without measurement noise. The SSH result steps to -0.8 within 3 seconds suggesting the existence of an SSH-N fault, while other outputs remain at zero. The dotted lines show the diagnosis result with Gaussian White Noises ($\mu = 0$, $\sigma = 5\,°\text{C}$ for temperature, $\sigma = 0.1\,\text{mole/s}$ for gas flow rate) in the measurement data. Although the results are disturbed by the noise, the SSH fault can still be distinguished from others because of its magnitude and response time. Thus, the fuzzy diagnosis system is insensitive to measurement noises.

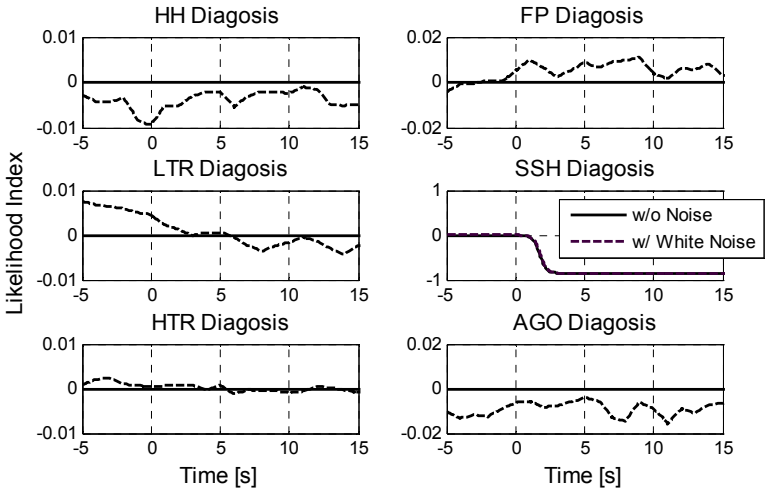

Figure 6-7 Fuzzy fault diagnosis results during SSH-N fault @ 150 kW.

The simulation results of the accommodation system are shown in Figure 6-8. The dash-dot lines denote the system response without fault accommodation. Although the output power drops by only 4kW, the stack temperature drops by 20°C to 570°C, which

is cold enough to stop all electrochemical reactions. Once the plant is shut down, it may take days to restart and may cause significant offline time.

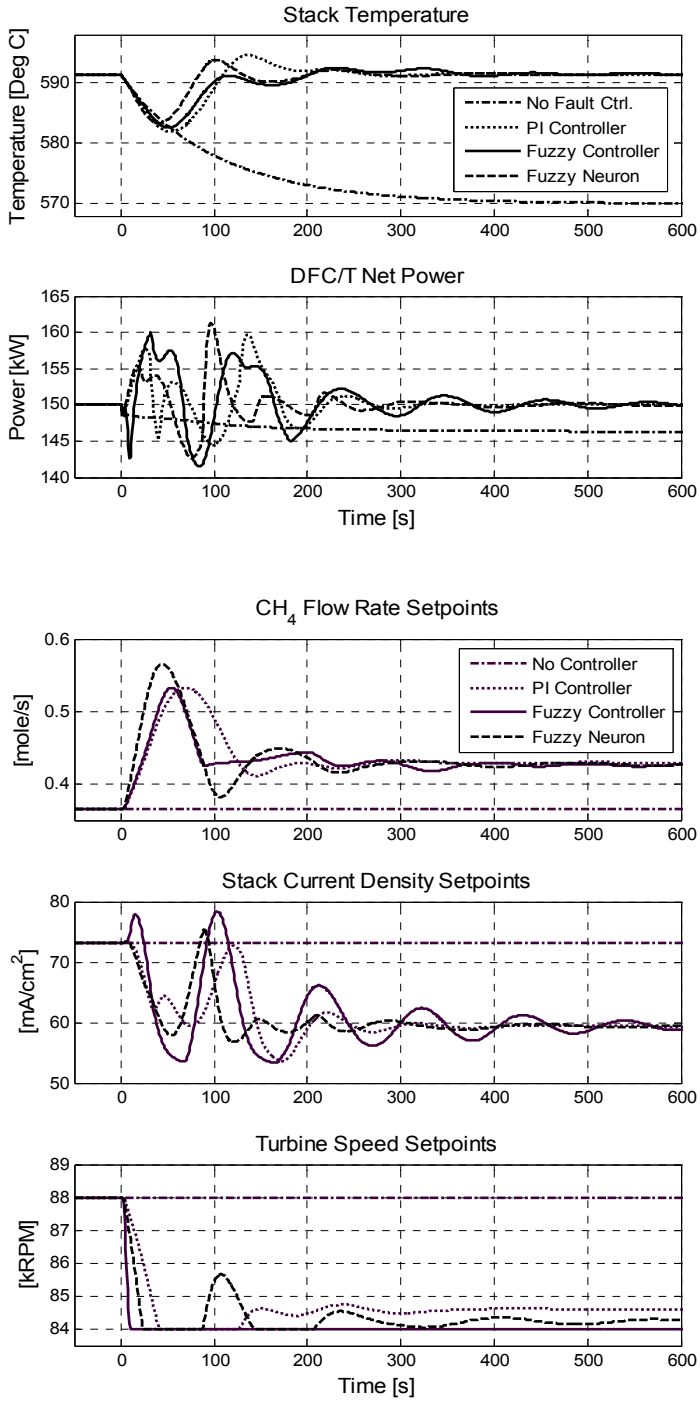

Figure 6-8 DFC/T responses during SSH-N fault @ 150 kW.

When the FDA system is applied, the fault regulation algorithm is activated after the fault occurs. The fault control strategies reduce the speed of the compressor to introduce less cold air; increase the amount of fuel by raising the methane flow rate and decrease the stack current density, so that more excessive fuel will be used to generate heat to warm up the fuel-cell stack. The excessive methane will boost the cell voltage [8], but with the reduced current density, the output power can still be maintained.

Three control methods, *i.e.,* PI controller (in dotted lines), fuzzy controller (in solid lines), and fuzzy-neural network (in dashed lines), are implemented with the fault accommodation strategies and framework in Figure 6-8. All of the three controllers are able to regulate the fault and drive the system to a steady working status in 300 seconds with a maximum temperature drop of 10°C. The fuzzy controller has less overshoot and the fuzzy-neural network is faster than the traditional PI controller in regulating the stack temperature. The three controllers have comparable disturbances of 10kW in power control, but the fuzzy controller has slightly more oscillations as time elapses.

6.4.2 LTR-P fault at 300 kW

An LTR-P fault at t = 0s is simulated in Figure 6-9 and Figure 6-10. When the plant is running at an output power of 300kW, the LTR fails in a faulty position so that heat is fully transferred without control. Thus, the compressed air is overheated by the LTR, and finally heats up the fuel-cell stack. Without the FDA system, the stack temperature (dash-dot lines in Figure 6-10) will rise up to 635°C, which is the upper limit of the safe operational region and may consequently damage the device or the catalyst.

The diagnosis results in Figure 6-9 presents the likelihood index for each fault pattern, where the LTR-P fault can be identified from others by its magnitude and response time, either without measurement noises, or with the similar Gaussian White Noises as in the previous case.

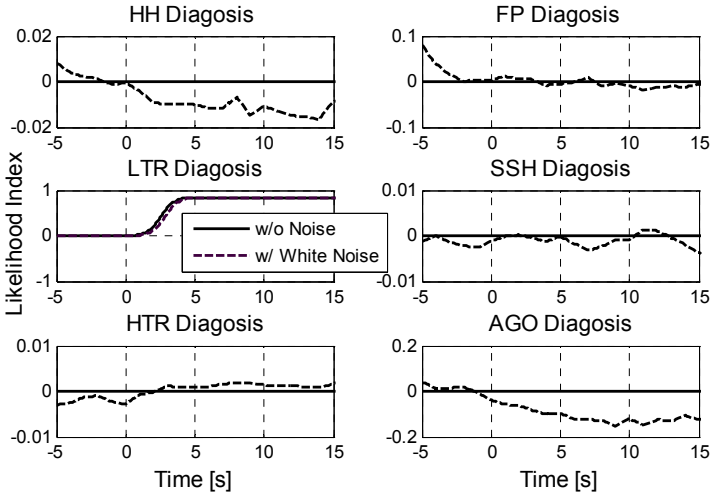

Figure 6-9 Fuzzy fault diagnosis results during LTR-P fault @ 300 kW.

Once the accommodation system is activated, it increases the compressor speed to blow more air into the system; decreases the amount of fuel by reducing the methane flow rate; and slightly increases the current density to compensate the power drop. However, the plant cannot recover to its previous output power due to the reduced amount of fuel and the ratio limitation between current density and methane flow rate.

The three controllers are investigated with the LTR-P fault. In Figure 6-10, the controllers regulate the fault and drive the system to a stable working status in 300 seconds with a temperature disturbance of 10°C and a lower output power of 290kW, which is 3.3% less the demand power. The fuzzy and fuzzy-neural controllers have smaller temperature disturbance than the PI controller, but the fuzzy controller converges

slower than the others. For the power control, the fuzzy controller gives less overshoot but lower convergence rate.

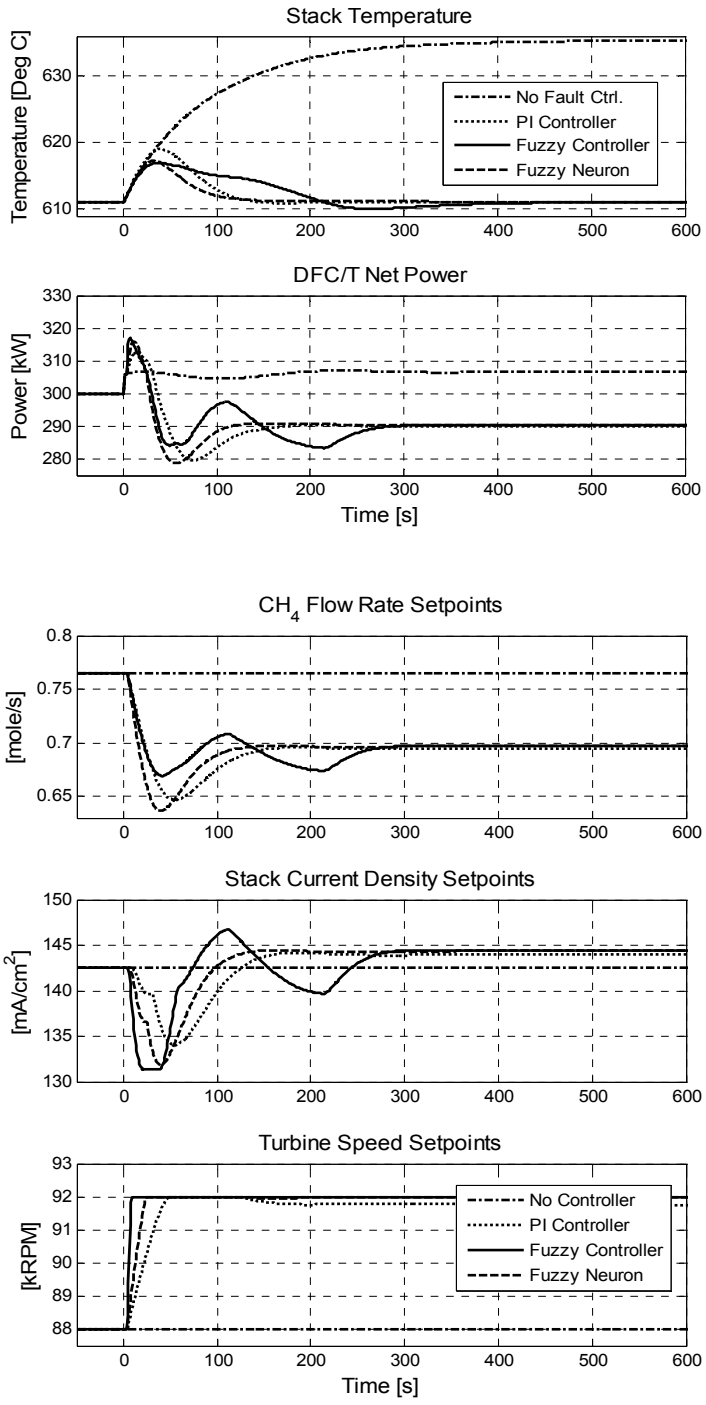

Figure 6-10 DFC/T responses during LTR-P fault @ 300 kW.

Chapter 7

Conclusion and Future Work

7.1 Conclusions

Because of high energy conversion efficiency and extra low emissions, fuel cells have shown their remarkable application potentials in distributed generation. As one of the most advanced fuel cell technologies, the DFC/T power plant received extensive attentions from researchers, developers, and governments. Significant research efforts were invested into system modeling and intelligent control system development for the power plant, providing the foundations for this dissertation, which intends to solve the problems of model accuracy, fuel efficiency, and plant reliability.

In this dissertation, to improve the accuracy of the mathematical model of the power plant and to provide a valid platform for the following and further research, an supplementary energy dynamic model, whose parameters are identified from online operational data, is developed to augment the original mathematical model. Furthermore, artificial neural networks are applied to compensate for the errors that cannot be modeled analytically, and to further improve the model accuracy. The hybrid model presented in this dissertation is an advanced dynamic system modeling method that both model parameters and uncertainties can be identified from operational data. The update ability of the hybrid model can keep itself valid while dynamics are changing in the actual plant. This hybrid modeling method is not only effective for the DFC/T power plant, but also

can be extended to most dynamic physical systems to provide a reliable platform for research, studies, and analyses.

Also in this dissertation, a multi-objective nonlinear optimization framework is developed for the DFC/T power plant working as a base-load power source, for which the fuel efficiency is a primary issue of plant operations. The particle swarm optimization and neural network combined model are implemented as the core optimization algorithm and the state estimator, respectively. The presented optimization framework is an extension and combination of heuristic optimizations and artificial neural network technologies. The framework is validated by the simulation on the DFC/T plant model, and in addition, it can also be applied to and will be effective for the optimization problems of the power plants with different types or configurations.

Meanwhile, the fault diagnosis and accommodation system is a successful application of fuzzy theories. The fuzzy FDA system can identify the fault correctly and promptly, and can effectively prevent the power plant from entering abnormal or even unsafe operating regions. The work in this dissertation demonstrates the capability of the fuzzy theory in detecting and regulating local failures for large-scale power plant systems.

Moreover, the integrated system provides a prototype of a comprehensive plant-wide control system, where local controllers, optimizer, fault detector, and plant models are working simultaneously and collaboratively. The overall control system is not a simple combination of the individual control systems, but an integrated system that each part cooperates with each other. With the intelligent control system, the efficiency and reliability of the DFC/T power plant are considerably improved, and the performance of

the entire control system can be upgraded. An intelligent autonomous control system is finally achieved for the hybrid power plant to perform high quality plant-wide management, by which accuracy, efficiency and reliability can be guaranteed.

7.2 Future Work

Future improvements of the intelligent control system are possible by investigating the overall control system on the actual DFC/T power plant and collecting more operational data for system improvement. Parameters of the pressure model can be refined if the operational data of pressure is available. Further analysis of plant optimization will suggest the bottleneck of the power plant against higher efficiency. Then, the plant configuration, structure, or the hardware can be improved to approach the expected fuel efficiency. For the FDA system, more types of membership functions and different control algorithms or controllers can be investigated and the transient of the accommodation actions will be further studied.

Regarding the DFC/T power plant, its interfaces and control algorithms to the utility grid is another important aspect of the control system. The DFC stack generates DC power while the turbine generator produces AC power at a variable frequency. Before connecting to the utility grid, the asynchronous AC power needs to be rectified and fed into a DC bus. Then the combined DC power is inverted to AC power with synchronized frequency and phase through a grid-tie power inverter. Additional power electronics units may be also required to eliminate or reduce the harmful harmonics

generated by the switching devices. The structure, control algorithms, and optimizations of the power electronics interface need additional studies and developments.

Moreover, the fuel-cell power plant may have various potential applications besides distributed generation. Since the fuel-cell power plant generates DC power directly, it should be highly attractive in the applications where high quality high capability DC power is required, such as electrolysis of copper and aluminum. Utilizing fuel-cell power plants, the product may be upgraded and the efficiency can be improved. Future research and case studies are possible regarding these specific applications.

Bibliography

[1] K. Tran and M. Vaziri, "Effects of dispersed generation (DG) on distribution systems," in *Proc. IEEE PES General Meeting*, June 12-16, 2005, pp. 748-753.

[2] M. C. Williams, J. P. Strakey, and S. C. Singhal, "U.S. distributed generation fuel cell program," *J. of Power Sources,* vol. 131, pp. 79-85, 2004.

[3] Department of Energy, "The smart grid: an introduction", <URL: http://www.oe.energy.gov/smartgrid.htm>.

[4] L. Doggett, "Guide to the American Recovery and Reinvestment Act of 2009," Congress of the United States, 2009.

[5] Department of Energy, "Future fuel cells R&D", <URL: http://www.doe.gov/>, [Accessed: June, 2009].

[6] FuelCell Energy, Inc., "Thrust area: hybrid fuel cell/turbine power systems", <URL: http://www.fuelcellenergy.com/>, [Accessed: May 29, 2009].

[7] T.-I. Choi and K. Y. Lee, "Interface of a fuel cell distributed generator with distribution system network," in *Proc. IEEE PES GM*, July 26-30, 2009.

[8] M. D. Lukas, K. Y. Lee, and H. Ghezel-Ayagh, "Development of a stack simulation model for control study on direct reforming molten carbonate fuel cell power plant," *IEEE Trans. on Energy Conv.,* vol. 14, Dec. 1999.

[9] M. D. Lukas, K. Y. Lee, and H. Ghezel-Ayagh, "Reduced-order dynamic model of carbonate fuel cell system for distributed generation control," in *Proc. IEEE PES Summer Meeting*, Seattle, WA, July 16-20, 2000, vol. 3, pp. 1793-1797.

[10] M. D. Lukas, K. Y. Lee, and H. Ghezel-Ayagh, "Plant-wide simulation of direct reforming molten carbonate fuel cell systems," in *Proc. IEEE PES Summer Meeting*, July 1999, vol. 1, pp. 532-535.

[11] M. D. Lukas, K. Y. Lee, and H. Ghezel-Ayagh, "Operation and control of direct reforming fuel cell power plant," in *Proc. IEEE PES Winter Meeting*, Jan. 23-27, 2000, vol. 1, pp. 523-527.

[12] H. Ghezel-Ayagh, M. D. Lukas, and S. T. Junker, "Dynamic Modeling and Simulation of a Hybrid Fuel Cell/Gas Turbine Power Plant for Control System Development," in *Proc. ASME 2nd Inter. Conf. on Fuel Cell Science, Eng. and Tech.*, 2004.

[13] R. A. Roberts, J. Brouwer, E. Liese, and R. S. Gemmen, "Dynamic simulation of carbonate fuel cell-gas turbine hybrid systems," *J of Engineering for Gas Turbines and Power,* vol. 128, issue 2, pp. 294-301, April 2006.

[14] S. Kameswaran, L. T. Biegler, S. T. Junker, and H. Ghezel-Ayagh, "Optimal off-line trajectory planning of hybrid fuel cell/gas turbine power plants," *AIChE J.,* vol. 53, issue 2, pp. 460-474, Feb. 2007.

[15] T.-I. Choi, K. Y. Lee, S. T. Junker, and H. Ghezel-Ayagh, "Neural network supervisor for hybrid fuel cell/gas turbine power plants," in *Proc. IEEE PES General Meeting*, Jun. 24–28, 2007, pp. 1-8.

[16] The California Energy Commission, "Distributed energy resources guide: fuel cells applications", <URL: http://www.energy.ca.gov/>, [Accessed: May 28, 2009].
[17] T. Shinoki, M. Matsumura, and A. Sasaki, "Development of an Internal Reforming Molten Carbonate Fuel Cell Stack," *IEEE Trans. on Energy Conversion,* vol. 10, pp. 722-729, December 1995.
[18] A. J. Leo and A. J. Skok, "Santa Clara direct carbonate fuel cell demonstration," in *Proc. FETC Fuel Cells '97 Review Meeting*, 1997.
[19] H. Ghezel-Ayagh, J. M. Daly, and Z. Wang, "Advances in direct fuelfell/gas turbine power plants," in *Proc. ASME Turbo Expo*, 2003.
[20] M. D. Lukas, K. Y. Lee, and H. Ghezel-Ayagh, "An explicit dynamic model for direct reforming carbonate fuel cell stack," *IEEE Trans. on Energy Conversion,* vol. 16, issue 3, pp. 289-295, September 2001.
[21] F. Kreith and M. S. Bohn, *Principles of heat transfer 5th edition*, Boston: PWS Publishing Company, 1997, chapter 1.
[22] M. Verhaegen and V. Verdult, *Filtering and system identification: a least squares approach*, New York: Cambridge University Press, 2007, pp. 28-37.
[23] W. Sun and Y. X. Yuan, *Optimization theory and methods: nonlinear programming*, New York: Springer, 2007, pp. 71-89, 119-130.
[24] G. P. Liu, *Nonlinear identification and control: a neural network approach*, London: Springer, 2001, chapter 1.
[25] F. Durst, *Fluid mechanics: An Introduction to the Theory of Fluid Flows*, Berlin, Heidelberg: Springer, 2008, chapter 4, 5.
[26] K. Y. Lee and M. A. El-Sharkawi, *Modern heuristic optimization techniques with applications to power systems*. Piscataway: IEEE Press, 2008.
[27] T. Back, "Selective pressure in evolutionary algorithms: A characterization of selection mechanisms," in *Proc. IEEE Conf. on Evolutionary Computation*, 1994.
[28] D. E. Goldberg and K. Deb, "A comparative analysis of selection schemes used in genetic algorithms," *Fundations of genetic algorithms,* pp. 69-93, 1991.
[29] Swiss Federal Institute of Technology, A comparison of selection schemes used in evolutionary algorithms 1995.
[30] G. Sywerda, "Uniform crossover in genetic algorithms," in *Proc. The 3rd international conference on genetic algorithms*, 1989, pp. 2-9.
[31] J. Kennedy and R. Eberhart, "Particle swarm optimization," in *Proc. IEEE International Conference on Neural Networks*, Perth, WA, Australia, Nov.-Dec., 1995, vol. 4, pp. 1942-1948.
[32] P. Angeline, "Using selection to improve particle swarm optimization," in *Proc. IEEE International Conference on Evolutionary Computation*, Anchorage, AK, May 4-9, 1998, pp. 84-89.
[33] V. Miranda and N. Fonseca, "EPSO-evolutionary particle swarm optimization, a new algorithm with applications in power systems," in *Proc. IEEE Transmission and Distribution Conference and Exhibition*, Oct. 6-10, 2002, vol. 2, pp. 745-750.

[34] M. Clerc, "The swarm and the queen: towards a deterministic and adaptive particle swarm optimization," in *Proc. CEC'99 Congress on Evolutionary Computation*, Washington, DC, 1999, vol. 3, pp. 1951-1957.

[35] C. A. Coello-Coello and M. S. Lechuga, "MOPSO: a proposal for multiple objective particle swarm optimization," in *Proc. CEC'02 Congress on Evolutionary Computation*, Mexico City, May 12-17, 2002, vol. 2, pp. 1051-1056.

[36] K. E. Parsopoulos and M. N. Vrahatis, "Particle swarm optimization method in multiobjective problems," in *Proc. ACM Symposium on Applied Computing*, Madrid, Spain, 2002, pp. 603-607.

[37] J. S. Heo, K. Y. Lee, and R. Garduno-Ramirez, "Dynamic Multiobjective Optimization of Power Plant Using PSO Techniques," in *Proc. IEEE PES General Meeting*, June 12-16, 2005, pp. 2543-2548.

[38] K. Y. Lee, J. S. Heo, J. A. Hoffman, S.-H. Kim, and W.-H. Jung, "Modified predictive optimal control using neural network-based combined model for large-scale power plants," in *Proc. IEEE PES General Meeting*, Tampa, FL, June 24-28, 2007, pp. 1-8.

[39] D. N. Jeyakumar, T. Jayabarathi, and T. Raghunathan, "Particle swarm optimization for various type of economic dispatch problems," *International Journal of Electrical Power & Energy Systems,* vol. 28, issue 1, pp. 36-42, January 2006.

[40] C. A. Coello-Coello, D. A. Van-Veldhuizen, and G. B. Lamont, *Evolutionary algorithms for solving multi-objective problems*. New York: Kluwer Academic Publishers, 2002.

[41] T. P. Bagchi, *Multiobjective scheduling by genetic algorithms*. Boston: Kluwer Academic Publishers, 1999.

[42] Y. Jin, M. Olhofer, and B. Sendhoff, "Dynamic weighted aggregation for evolutionary multiobjective optimization," in *Proc. Genetic and Evolutionary Computation Conference*, 2001.

[43] K. E. Parsopoulos and M. N. Vrahatis, "Particle swarm optimization method in multiobjective problems," in *Proc. 2002 ACM symposium on Applied computing*, Madrid, Spain, 2002, pp. 603-607.

[44] C. M. Fonseca and P. J. Fleming, "Genetic algorithms for multiobjective optimization formulation discussion and generalization," in *Proc. The Fifth International Conference on Genetic Algorithms*, San Mateo, CA, 1993.

[45] C. A. Coello-Coello, G. T. Pulido, and M. S. Lechuga, "Handling multiple objectives with particle swarm optimization," *IEEE Trans. on Evolutionary Computation,* vol. 8, issue 3, pp. 256-279, 2004.

[46] C. A. Coello-Coello, "A comprehensive survey of evolutionary-based multiobjective optimization techniques " *Knowledge and Informaiton Systems,* vol. 1, issue 3, pp. 269-308, 1998.

[47] C.-C. Ku, K. Y. Lee, and R. M. Edwards, "Improved nuclear reactor temperature control using diagonal recurrent neural networks," *IEEE Trans. on Nuclear Science,* vol. 39, issue 6, pp. 2298-2309, December 1992.

[48] M. Clerc and J. Kennedy, "The particle swarm - explosion, stability, and convergence in a multidimensional complex space," *IEEE Trans. on Evolutionary Computation,* vol. 6, issue 1, pp. 58-73, February 2002.

[49] K. Y. Lee, J. S. Heo, J. A. Hoffman, S.-H. Kim, and W.-H. Jung, "Neural network-sased modeling for a large-scale power plant," in *Proc. IEEE PES General Meeting*, Tampa, FL, June 24-28, 2007, pp. 1-8.

[50] J. S. Heo and K. Y. Lee, "A multi-agent system-based intelligent identification system for control and fault-diagnosis for a large-scale power plant," in *Proc. IEEE PES General Meeting*, Montreal, Que., 2006, pp. 1-6.

[51] D. Marqardt, "An algorithm for least-squares estimation of nonlinear parameters," *SIAM Journal on Applied Mathematics,* vol. 11, pp. 431-441, 1963.

[52] The MathWorks, Inc., Neural network TOOLBOX for use with MATLAB, user's guide version 4, 2006.

[53] J. Calado, J. Korbicz, K. Patan, R. Patton, and J. S. D. Costa, "Soft computing approaches to fault diagnosis for dynamic systems: a survey," *European J. of Control,* vol. 7, pp. 248-286, July 2001.

[54] R. Isermann and P. Balle, "Trends in the application of model-based fault detection and diagnosis of technical processes," *Control Engineering Practice,* vol. 5, issue 5, pp. 709-719, March 1997.

[55] M. M. Polycarpou and A. J. Helmicki, "Automated fault detection and accommodation: a learning systems approach," *IEEE Trans. on System, Man, and Cyber.,* vol. 25, issue 11, pp. 1447-1458, Nov, 1995.

[56] J. Farrel, T. Berger, and B. D. Appleby, "Using learning techniques to accommodate unanticipated faults," *IEEE Control Systems Magazine,* vol. 13, issue 3, pp. 40-49, June 1993.

[57] S. Simani and C. Fantuzzi, "Fault diagnosis in power plant using neural networks," *Info. Sciences,* vol. 127, pp. 125-136, Aug. 2000.

[58] K. Kim and E. B. Bartlett, "Nuclear power plant fault diagnosis using neural networks with error estimation by series association," *IEEE Trans. on Nuclear Science,* vol. 43, pp. 2373-2388, Aug. 1996.

[59] A. L. Dexter, "Fuzzy model based fault diagnosis," *IEE Proc. - Control Theory Applications,* vol. 142, pp. 545-550, Nov. 1995.

[60] C.-w. Xu and Y.-z. Lu, "Fuzzy model identification and self-learning for dynamic systems," *IEEE Trans. on Systems, man, and cybernetics,* vol. 17, issue 4, pp. 683-689, 1987.

[61] O. M. Al-Jarrah and M. Al-Rousan, "Fault detection and accommodation in dynamic systems using adaptive neurofuzzy systems," *IEE Proc. - Control Theory Applications,* vol. 148, issue 4, pp. 283-290, July 2001.

[62] T. Escobet, D. Deroldi, S. d. Lira, V. Puig, J. Quevedo, J. Riera, and M. Serra, "Model-based fault diagnosis in PEM fuel cell systems," *Journal of Power Sources,* vol. 192, pp. 216-223, 2009.

[63] P. M. Frank, "Fault diagnosis in dynamic systems using analytical and knowledge-based redundancy," *Automatica,* vol. 26, pp. 459-474, 1990.

[64] H. Monsef, A. M. Ranjbar, and S. Jadid, "Fuzzy rule-based expert system for power system fault diagnosis," *IEE Proceedings - Generation, Transmission and Distribution,* vol. 144, issue 2, pp. 186-192, March 1997.

[65] A. Ben-Abdennour and K. Y. Lee, "An autonomous control system for boiler-turbine units," *IEEE Trans. on Energy Conv.,* vol. 11, June 1996.

[66] A. O'Dwyer, *Handbook of PI and PID controller tuning rules, 2nd Ed*, London: Imperial College Press, 2006, chapter 4.

[67] J.-X. Xu, C. Liu, and C. C. Hang, "Tuning of fuzzy PI controllers based on gain/phase margin specifications and ITAE index," *ISA Transactions,* vol. 35, pp. 79-91, 1996.

[68] J.-S. R. Jang, "ANFIS: Adaptive-network-based fuzzy inference system," *IEEE Trans. on Systems, Man, and Cybernetics,* vol. 23, issue 3, pp. 665-685, June 1993.

VITA

Wenli Yang

Wenli Yang received his B.S. degree in Automation and M.S. degree in Control Science and Engineering from Tsinghua University in Beijing, China, in 2004 and 2006, respectively.

He is currently a Ph.D. candidate in Electrical Engineering at the Pennsylvania State University. His research interests include control systems, power systems, alternative energy, power electronics, distributed generation, artificial intelligence, and robotics.